



Photocatalytic degradation of Perchloroethylene by a lab-scale continuous-flow annular photoreactor packed with glass beads carbon-doped TiO₂ nanoparticles

Hojjat Kazemi ^{a,*}, Mahboubeh Rabbani ^b, Haniye Kashafroodi ^b and Hossin kazemi ^a

^aAnalytical Chemistry Research Group, Research Institute of Petroleum Industry (RIPI), Tehran, Iran

^bDepartment of Chemistry, Iran University of Science and Technology, Narmak, Tehran, Iran

ARTICLE INFO:

Received 14 Aug 2021

Revised form 28 Oct 2021

Accepted 7 Nov 2021

Available online 28 Dec 2021

Keywords:

TiO₂ nanoparticles,
Photocatalyst,
Chlorinated volatile organic compounds,
Pollutant degradation,
Sol-gel,
Gas chromatography-mass spectrometer

ABSTRACT

In this study, the amount of photocatalytic degradation of perchloroethylene in the gas phase was investigated by a fixed bed continuous-flow tubular photoreactor. The photoreactor consists of a cylindrical glass tube, was filled with glass beads coated with nanoparticles of TiO₂, and TiO₂ doped carbon (TiO₂-C). These nanoparticles were synthesized by the sol-gel method and deposited on glass beads using the sol-gel dip technique. X-ray diffraction (XRD), scanning electron microscopy (SEM), Fourier transforms infrared spectroscopy (FT-IR), and diffuse reflectance spectroscopy (DRS) were used for the characterization of synthesized materials. The effect of different parameters such as relative humidity, residence time, PCE concentration on the photocatalytic degradation process was investigated by ultraviolet irradiation to achieve the highest possible degradation efficiency. The PCE degradation and byproduct species were monitored and identified with a gas chromatography-mass spectrometer device (GC-MS). Under the optimum experimental conditions, the photocatalytic activities of TiO₂, TiO₂-C were investigated and compared together. The results showed that photocatalytic activity of TiO₂ for degradation of PCE was extremely increased when doped with carbon. For TiO₂-C catalyst, under UV irradiation (3000 ppm initial PCE concentration, 30% humidity and 1 min residence time) approximately 96% of the initial PCE was degraded. Also, the catalyst showed high stability over 48 h without a decrease in catalytically efficiency. All results show that TiO₂-C is a good candidate for application PCE degradation.

1. Introduction

Among volatile organic compounds (VOCs) chlorinated volatile organic compounds, such as perchloroethylene (PCE), are important because of widely used as solvents at industrial scale in metal parts, semiconductors washing, dry cleaning, etc.

This extensive use leads to their being extremely present in the water and air. These compounds are toxic, carcinogenic and have many other adverse effects on humans [1, 2]. Therefore, there are great efforts to develop inexpensive and effective processes that can completely degrade these compounds. In the physical methods, the pollutants are only transferred from one phase to another without any degradation. The chemical

*Corresponding Author: Hojjat.Kazemi

Email: hojjatkazemi4@yahoo.com

<https://doi.org/10.24200/amecj.v4.i04.159>

methods are expensive, require high doses of chemicals, and produce large amounts of sludge [3]. In recent years, advanced oxidation processes (AOPs) have been used for the degradation and mineralization of the potentially toxic organic and inorganic contaminants in industrial wastewaters [4, 5]. Some AOPs are the photo-catalytic [6], Fenton and photo-Fenton [7, 8], UV/H₂O₂ [9] processes. Heterogeneous photocatalytic oxidation (PCO) appears to be a promising process for eliminating VOCs from the air because of operation at ambient temperature and ability to complete degradation/mineralization of VOCs (by-products are generally harmless CO₂, H₂O and mineral acids) [10, 11]. Many reports described the degradation of PCE through PCO [11, 12]. In these reports, TiO₂ is the most widely used as a photocatalyst because of its high photocatalytic activity, non-toxicity, and stability [13, 14]. Although TiO₂ itself has been proved to be a suitable photocatalyst for oxidation of PCE through PCO, more efforts are needed for further improvement of photocatalytic performance of TiO₂-based catalysts. Supporting on materials with large surface areas such as glass fiber [15], paint [16], thin-film TiO₂ [17], TiO₂ pellet [18], carbon black or activated carbon [19], carbon nanofibers [20], carbon nanotube [21] is one approach. Another trend is combining or doping TiO₂ with other materials such as Ag [22], Au [23], Sn [24], Pb [25], Ni [26] metal oxides [27] to improve the performance of the photocatalyst. Among these attempts, TiO₂ doping with transition metals ions such as V, Co, or Fe has been a common approach for improving the photocatalytic performance of the catalyst. However, some key problems remain unresolved, for example, doped materials suffer from thermal instability, photo-corrosion, and an increase in the carrier-recombination probability. Non-metal (B, F, N, C etc.) doping has since proved to be far more successful. Especially, in the process of carbon doping, the C element is always suggested permeating to the lattice of TiO₂ substituting a lattice O atom and forming O–Ti–C species [28-31]. Another approach is to change or

design new reactor configurations. Some reactor configurations are honeycomb monolith, plate, fluidized bed, packed bed, and annular tube flow [32, 33]. The design of the photocatalytic reactor plays an important role in its photocatalytic performance. Some factors such as specific surface area, pass-through channels, air velocity, direction and angle of irradiance of UV light on the catalyst surface, contact area and a mass transfer should be considered in the design of a photocatalytic reactor [32, 33].

In this project, a fixed substrate filled photocatalytic system was used, with a light source in its center, which in other words, is a combination of a filled and ring-shaped system. On one hand, the advantage of ring-shaped tube systems was used for direct light radiation to the reaction surface taking into account placing the light source in the center of the system, which reduces the number of bulbs as well as the effective use of diffused light from an optical source in different directions and, on the other hand, a greater contact surface between the catalyst and the pollutant in the fixed substrate system was created. The rotating center system is designed for two rows of glass balls to be placed nearby each other, this design increases the contact surface of the pollutant with the catalyst compared to other systems. Also, direct light radiation to glass balls can cause light fractions in any ball and increase light intensity throughout the system. In general, the system is designed to utilize all the power and efficiency of the catalysts by increasing the reaction surface and the immediate light exposure. That's why in this work, we report an experimental study of the photocatalytic oxidation of PCE in the gas phase using a lab-scale continuous-flow annular photoreactor packed with glass beads. TiO₂, C doped TiO₂ nanoparticles synthesized with the sol-gel method and deposited at the surface of glass beads with dip-coating technique. The performance of the photoreactor was evaluated for different operating conditions, such as feed flow rate, PCE concentration, residence time and relative humidity. To prove efficiency in industrial

applications, the effect of these parameters was investigated under the same industrial condition. For this propose, High concentrations of PCE (between 574 and 2442 ppm), a large range of air stream flow rates contaminated with PCE (59–300 mL min⁻¹, measured at 298 K and 1 bar) and different water vapour contents (12–40%, measured at 298 K and 1 bar) were employed.

2. Experimental

2.1. Materials

All the solvents and chemicals were purchased from Merck and Sigma-Aldrich Companies and used without further purification. The glass beads with a diameter of 5-6 mm were used as a support material and deionized (DI) water was used to prepare the different solutions and washing steps.

2.2. Instruments

The X-ray diffraction (XRD) patterns were recorded by a Philips Xpert X-ray diffractometer (Model PW1729) with Cu K α radiation. The Structures and morphologies of nanoparticles were determined using scanning electron microscopy (SEM, TE-SCAN model MIRA3). The Fourier transform-infrared (FT-IR) spectra were obtained using BRUKER spectra VERTEX apparatus. The UV-VIS diffuse reflectance spectra (DRS) were recorded by a DRS apparatus (Shimadzu UV-1800). The identification of photodegradation by-products was done by a gas chromatography-mass spectrometry (GC-MS) system (Shimadzu, QP-2010SE).

2.3. GC/MS analysis

The identification of product gas streams and intermediate products were analyzed employing a gas chromatography-mass spectrometry (GC/MS) system operating in electron impact mode using an HP-5 (30m \times 0.25mm \times 250 μ m) capillary column. The GC column was operated in a temperature-programmed mode with an initial temperature of 35 $^{\circ}$ C held for 5 min, ramp at 4 $^{\circ}$ C min⁻¹ up to 250 $^{\circ}$ C and held at that temperature for 5 min. Injector temperature was 280 $^{\circ}$ C with helium serving as

the carrier gas at the flow rate of 2 mLmin⁻¹. The identification of photodegradation products was done by comparing the GC/MS spectra patterns with those of standard mass spectra in the National Institute of Standards and Technology (NIST) library.

2.4. Catalyst base preparation method

Before the synthesis, transparent glass beads (with a diameter of 5-6 mm) were roughened mechanically by sandblasting method to increase surface area and adherence between the catalyst and the support. The surface glass beads were physically roughened in a mixture of water, sandblasting sand and sanding powder using a mechanical mixer and then etched in 1M NaOH solution. After sandblasting, the glass beads were washed sequentially and thoroughly with acetone, ethanol and deionized water (DW). Then they were dried at 80 $^{\circ}$ C for 1 h in the oven [34].

2.5. Synthesis of TiO₂, C doped TiO₂, supported on roughened glass bead

TiO₂, C doped TiO₂ were prepared via sol-gel method according to the previous reports [34] with few modifications. Briefly, for preparation of carbon-doped TiO₂, 50 mmol of Tetrabutyl Orthotitanate (TBOT) was slowly added to a solution of ethanol and water under continuous magnetic agitation at room temperature. Then 4 ml of Hydrochloric acid 1M was added. The resulting mixture was kept stirred for 3 hours at a speed of 500 rpm and then the roughened glass beads were added to the liquid mixture. After 10 minutes, glass beads were separated and dried at 80 $^{\circ}$ C for 1 hour and calcinated at 200 $^{\circ}$ C for 5 hours, using a heating rate of 1 $^{\circ}$ C min⁻¹. Pure TiO₂ was also synthesized with the same procedures as described above, except calcination temperature for the synthesis of pure TiO₂ was set at 350 $^{\circ}$ C.

2.6. Photocatalytic reactor

In this study, Photocatalytic degradation of PCE in the air using titanium oxide base (TiO₂, TiO₂-C) catalysts was evaluated in a lab-scale continuous-

flow tubular UV-photoreactor packed with coated glass beads. The continuous gas flow photoreactor with the length of 40 cm has consisted of two coaxial tubes. The coated glass beads filled the void in-between two coaxial tubes and the inner tube was made of quartz glass housing the light source. The outer tube was a Pyrex tube packed with catalyst coated glass beads to a height of 27 cm which provided an effective volume of 200 ml in the reactor. The external wall of the cylinder was completely covered with a layer of aluminum sheet, so that the light is constantly reflected inside the cylinder. The light source was an 8-watt fluorescent lamp (Philips UVC 8W T5) to provide light with appropriate energy in the ultraviolet region. The reactor feed was prepared by mixing of PCE vapors, humid and dry air which were generated via passing the air through two glass impingers containing pure liquid PCE and distilled

water. PCE concentration and humidity were adjusted by controlling flow rate of dry air into the impingers and the amount of dry air entering the mixing tank. The concentration of PCE in the inlet and outlet streams of the photoreactor and degradation byproduct were measured by a GC/MS. humidity and CO₂ content were measured by a SAMWON ENG SU-503B device and a KIMO AQ-100 CO₂ meter, respectively and rechecked by titration methods (Fig.1). All flow rate of was adjusted by a rotameter and the degradation efficiency was measured by equation 1:

$$\text{Degradation Efficiency} = \frac{C_{\text{inlet}} - C_{\text{outlet}}}{C_{\text{total}}} \times 100 \quad (\text{Eq.1})$$

C_{inlet} , C_{outlet} and C_{total} were concentrations of inlet and outlet and total of PCE respectively.

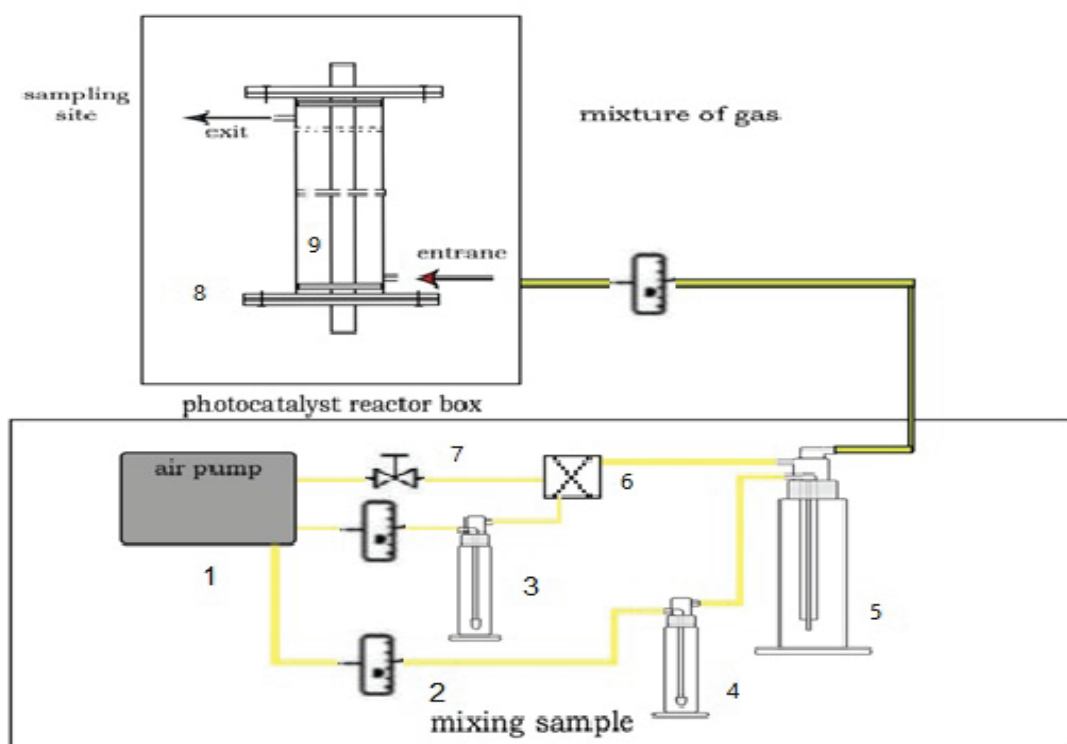


Fig.1. Schematic of photocatalytic system 1) Air reservoir 2) Rotamer 3) Impinger containing water 4) impinger containing Perchloroethylene 5) Mixing chamber 6) Tee 7) Tap 8) Reactor 9) Light source

3. Results and discussion

3.1. Photocatalyst characterization

The synthesized materials were first characterized with X-ray diffraction as shown in Figure 2. Fig. 2 shows a typical XRD pattern of the pure TiO₂ and TiO₂-C which is in good agreement with the standard patterns for anatase titanium dioxide (JCPDS 21-1272) [35] and confirm the absence of any other impurity. The XRD pattern of the TiO₂-C was identical to pure TiO₂ but strongest peak at $2\theta = 25.3^\circ$ (representative of (101) plane). Compared with pure TiO₂ shifted slightly to a higher 2θ value. Also for all synthesized materials, diffraction peaks were weakened and broadened, suggesting distortion of the crystal lattice. Greater change can be seen with the addition of carbon and vanadium, indicating that vanadium and carbon were incorporated into the lattice and greater distortion of the crystal lattice was accorded [36, 37]. however, this is favorable

for photodegradation purposes because of increasing pathways for gas-phase penetration into the inner spaces of the active materials and increasing of material transportation.

The IR spectrum of TiO₂ and TiO₂-C were shown in Figure 3. The FT-IR spectrum of both spectra displays absorption bands between 700 and 800 cm⁻¹, which can be assigned to the metal-oxygen stretching vibrations of Ti-O [38]. The broad peak in the range of 3400 nm and sharp peak in the range of 1620 nm corresponds to the stretching and bending bonds of the water molecule, respectively, which occur due to lack of inter-tissue water or the absorption of moisture on the surface of the synthesized materials. The two peaks appearing in 1350 and 1200 nm of the TiO₂-C compound are related to the CH₃ and CH₂ bending bonds, which confirms the presence of carbon in the structure of this compound [18, 39].

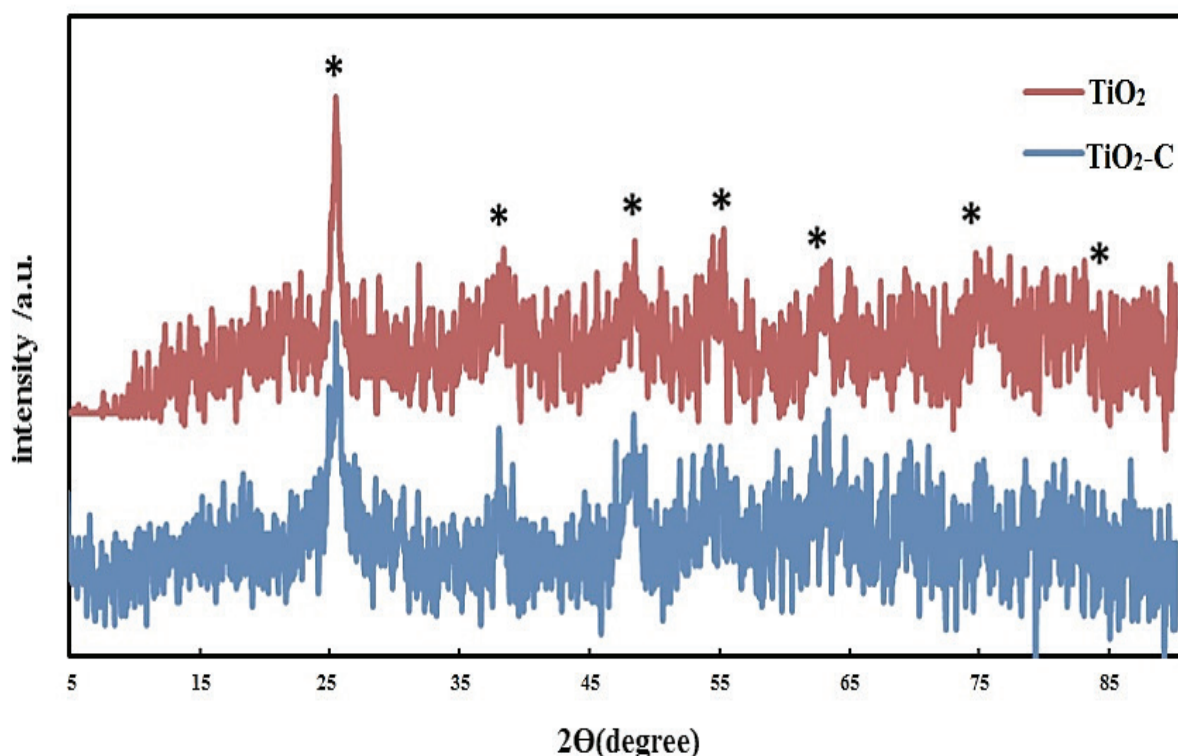


Fig.2. XRD pattern of the pure TiO₂ and TiO₂-C

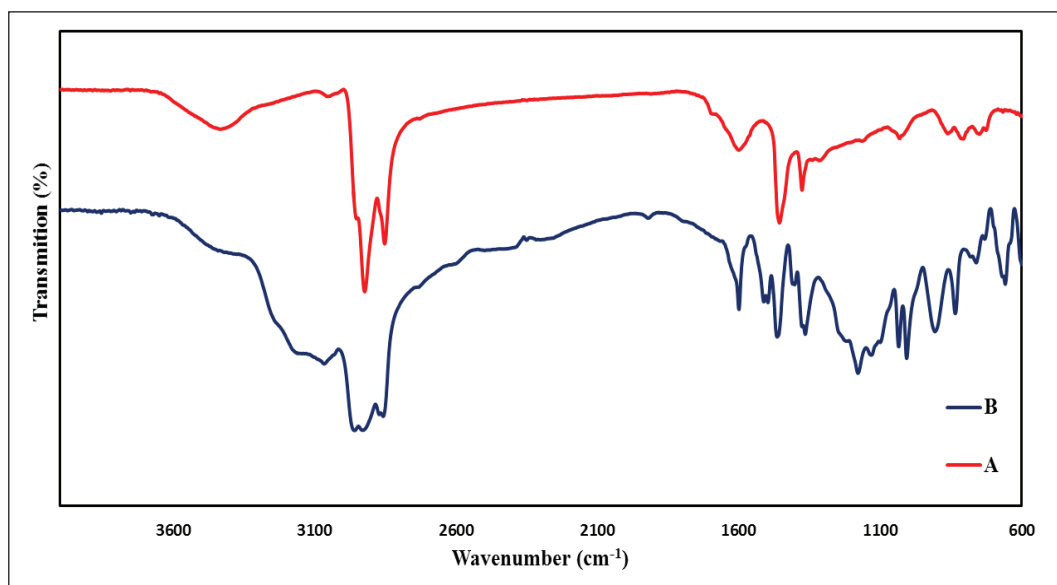


Fig.3. FT-IR spectrum of A) TiO₂ and B) TiO₂-C

The optical absorption property is an important factor to influence the photocatalytic activity of the catalysts. Thus, the absorbance properties of as-prepared TiO₂ and TiO₂-C were analyzed by the UV-vis diffuse reflection spectra (DRS), and the results are shown in Figure 4. Pure TiO₂ shows the absorbance in the UV region, in which the absorption start point of TiO₂ is around 400nm. While TiO₂-C exhibits good absorption in the UV region and the broad absorption region with less intense in the visible light. Compared with pure TiO₂, TiO₂-C absorbed photon energy in the visible region up to

700 nm indicating that the incorporated elemental carbon was acting as a photosensitizer [40]. The results suggest that TiO₂ and TiO₂-C photocatalysts have higher photocatalytic performances in the UV region.

The morphology of the fabricated products was characterized by scanning electron microscopy (SEM) and the results are shown in Figure 5. As seen in Figure 5 the synthesized particles have mostly a spherical morphology with the obtained size in the range of about 14-45 nm for TiO₂ and TiO₂-C.

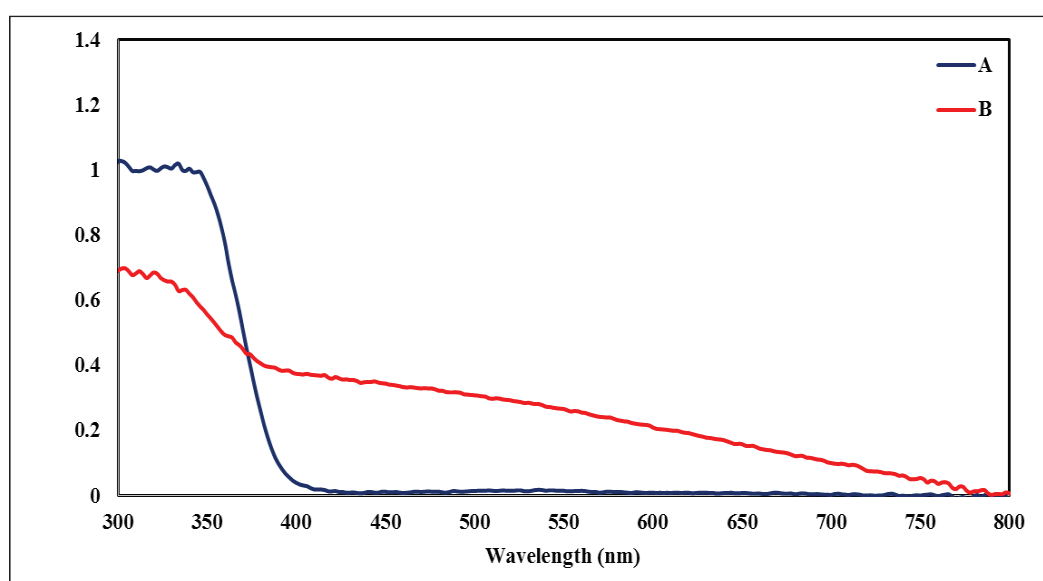


Fig.4. UV-vis diffuse reflection spectra A) TiO₂ and B) TiO₂-C

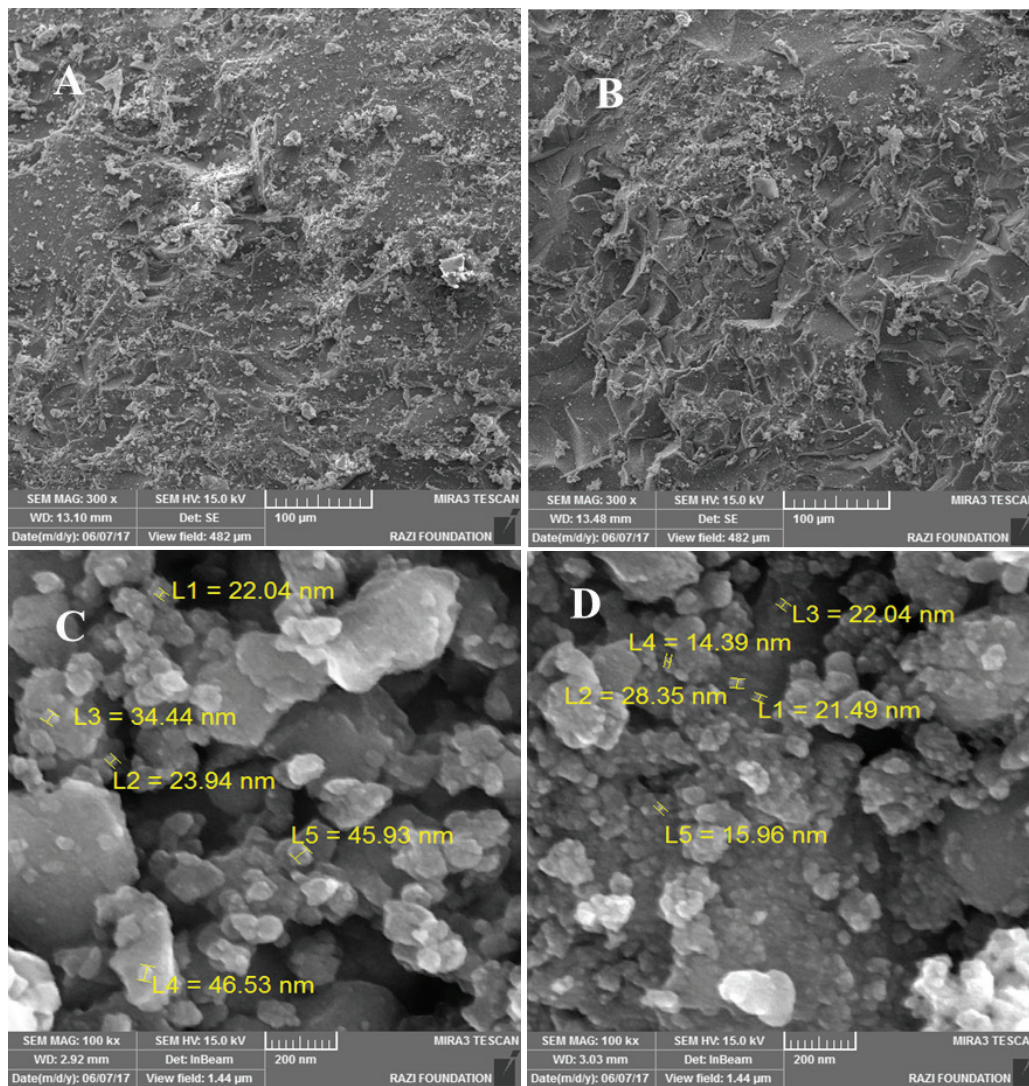


Fig.5. SEM image of (A, C) TiO₂ and (B,D) TiO₂-C

3.2. Investigating the reaction conditions of photocatalytic system

3.2.1. Concentration effect

First, the degradation efficiency of PCE using TiO₂-C photocatalyst in different inlet feed concentrations from 400 to 5000 ppm under UV irradiation, the residence time of 1 min and flow rate 200 mL min⁻¹ investigated. Figure 6 is illustrated the effect of increasing PCE feed concentrations on photocatalytic degradation efficiency. As shown, degradation efficiency increased by increasing PCE concentration up to 3000 ppm and

rich to 99%, indicating higher PCE means higher adsorption in the surface of the photocatalyst, and higher mass transfer between the PCE gas and the catalyst surface which increased the PCE degradation. Further PCE concentration caused a decrease in the degradation efficiency, because of surface flooding of photocatalyst [41s, this referenceshowed in supporting nformation page, SIP]. It was seen that the degradation capacity of this system is 3000 ppm, which is much higher than that other of reported photocatalytic systems with the same lamp.

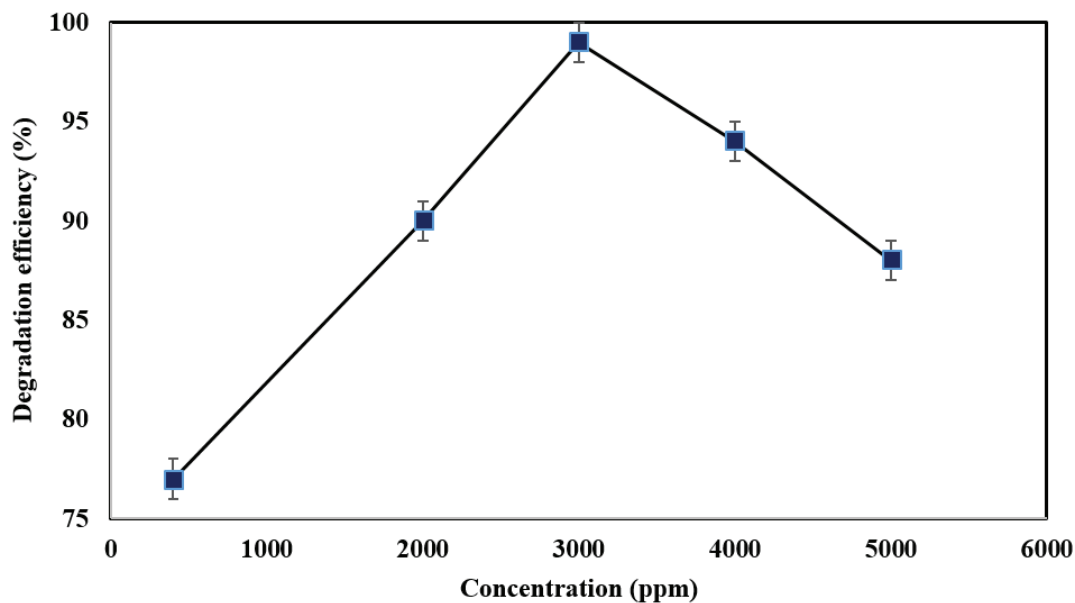


Fig.6. The effect of concentration on degradation efficiency of $\text{TiO}_2\text{-C}$ at a fixed time of 1 min

3.2.2. Residence time effect

Figure 7 shows the residence time effect on degradation efficiency of $\text{TiO}_2\text{-C}$ photocatalyst over the range of the residence times from 0.2 min to 2 min at a 3000 ppm PCE concentration. Residence time in the reactor was controlled by changing the flow rate. As shown for photocatalyst, the PCE degradation increased with increasing

residence time, because PCE stays longer inside the reactor and have more opportunity to react with photocatalyst [18]. The increasing residence time of more than 1 min for photocatalyst did not only increase significantly in the degradation efficiency of PCE but also increased the elimination time. As a result, the time of one minute was chosen as the optimal time.

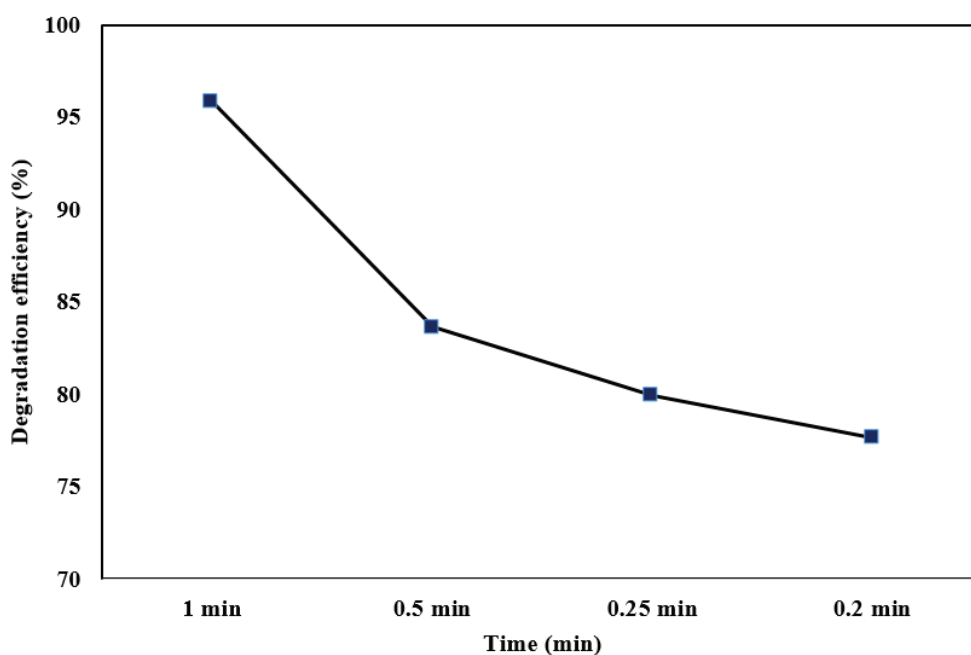


Fig.7. the effect of time on degradation efficiency of $\text{TiO}_2\text{-C}$ at 3000 ppm

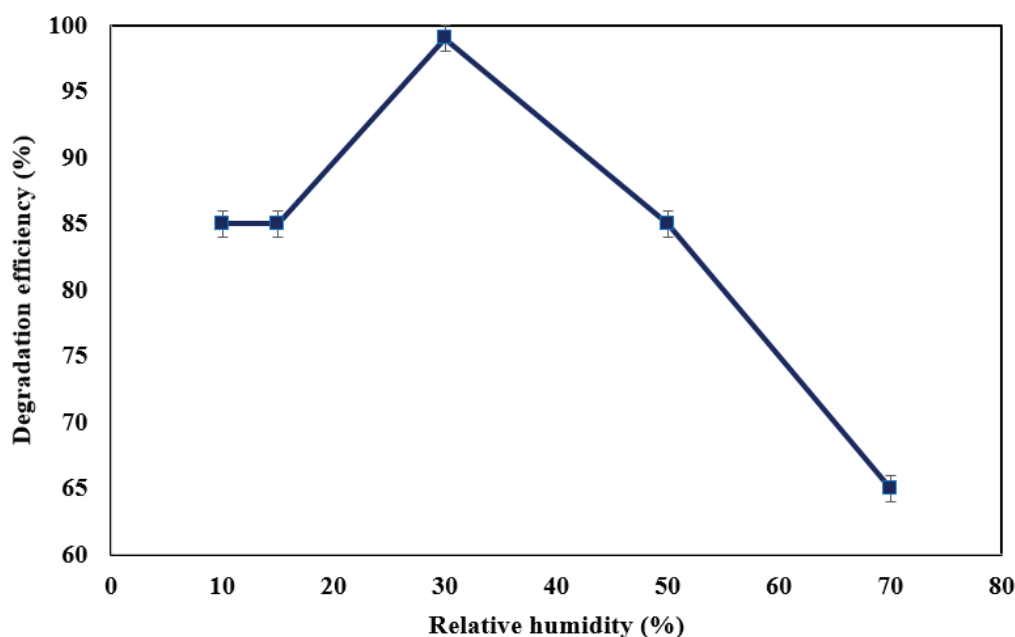


Fig.8. The effect of relative humidity on degradation efficiency of TiO₂-C at constant concentration and time of 3000 ppm, 1 min respectively

3.2.3. Moisture Effect

Due to Figure 8, the effect of the water content on the PCE degradation over TiO₂-C was evaluated under five relative humidity (RH) conditions (10, 15, 30, 50 and 70%), 3000ppm PCE concentration, one-minute residence time and UV irradiation. Figure 8 shows that the degradation efficiency of PCE attained under each RH condition. As shown, a significant change in degradation efficiency was not observed as the RH increased from 10 to 15 % but when RH increased up to 30% degradation efficiency increased and rich to approximately 99%. Further increasing of RH reduced the degradation efficiency due to competitive adsorption of PCE and water molecules on the photocatalytic surface. Actually, by more increasing the moisture content of the incoming gas, most photocatalytic active surfaces are coated with water and remaining less surface to contact with PCE and its degradation [14, 42s, SIP]. The opposing effect of the water content has already been discussed in several research works and even so it still is a matter of debate [42s-45s, SIP]. Several authors reported that the absence of water vapour can seriously retard

the degradation of several chemicals and their mineralization to CO₂ may become incomplete, but excessive water vapor may inhibit the degradation by competitive adsorption on the photocatalyst surface [14].

3.3. Photocatalytic degradation

The photocatalytic performance of prepared samples was evaluated by the PCE degradation under UV light. For comparison, the photocatalytic activity of pure TiO₂, TiO₂-C₂ was also determined under the optimal conditions (eg. 1 min residence time, 30% RH and 3000 ppm PCE concentration). First, the photocatalytic system was filled with glass balls without a photocatalyst coating. Then, the degradation efficiency was studied in the presence of photocatalysts coated glass balls. When the lamp was illuminated, the output of the system was sampled at different times, and the process of changes in concentration, efficiency and output products was investigated by the GC-MS. For the photolysis process (without using any photocatalyst), the system's efficiency was determined 99% based on the reduction of perchloroethylene concentration in

120 min. At first, it seemed that the lamp alone was able to degrade perchloroethylene and perform the complete reaction of converting perchloroethylene to carbon dioxide, water and hydrochloric acid. But after a long time, we observed a large volume of solid crystals at the end of the system and the outlet pipe. By identifying these materials with GC-MS, we realized that most of the material has converted into compounds that result from a simple breakdown of Perchloroethylene bonds. That's why we measured system efficiency based on CO₂ gas. Also, the system's efficiency was calculated 10% based on the produced amount of CO₂ gas. So that the lamp was not capable of completely degrading PCE, merely transforming it into other materials with more complex structures and converting has a small fraction of it into complete degradation reaction products. Also, the system's efficiency was obtained 58% and 95.6% for TiO₂ and TiO₂-C, respectively based on the produced amount of CO₂ gas. The results indicate that in the case of using TiO₂-C, the PCE degradation is almost complete

and turns into completed reaction products in its output, which indicates the correct choice of the pollutant, ie carbon in improving photocatalyst. Table 1 summarizes the major intermediate compounds identified.

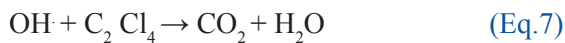
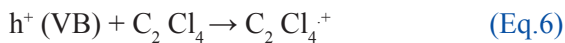
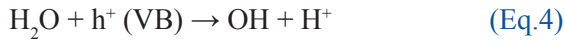
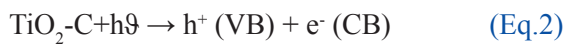
3.4. Photocatalytic mechanism for PCE degradation

For photocatalytic oxidation, an important step of photoreaction is the formation of the hole-elect pairs which need the energy to overcome the band gap between the valence band (VB) and conduction band (CB) [41s,SIP]. TiO₂ as a semiconductor has a valence band and a conduction band. When photocatalyst exposes to UV light, TiO₂ can absorb UV light and electrons transfer from the valence band (VB) to the conduction band (CB) and generate electron-hole pairs (Eq.2) [46s, SIP]. Electrons of CB can react with oxygen adsorbed on the catalyst surface to produce oxygen radicals (O₂⁻) (Eq.3). Holes of VB can react with H₂O to produce ·OH radicals (Eq.4, 5). Also, the electrons and the holes

Table.1. Products obtained from photocatalytic degradation of perchloroethylene with UV lamp alone and UV lamp with, TiO₂ and TiO₂-C

Photocatalyst	Compound
UV lamp	H ₂ O
	C ₂ Cl ₄
	Dichloroacetic acid
	Trichloro dehydrate
	Trichloroacetic acid
UV lamp -TiO ₂	H ₂ O
	HCl
	C ₂ Cl ₄
	Trichloroacetyl chloride
	Methyl trichloroacetate
	Trichloroacetic acid
UV lamp -TiO ₂ -C	H ₂ O
	CO ₂
	HCl
	C ₂ Cl ₄

may react directly with PCE molecules leading to the formation of oxidizing species (Eq.6) [14, 31, 47s, 48s, SIP]. The radicals ($\cdot\text{OH}$) as a strong oxidizing species and O_2^- are responsible for the degradation of PCE. These $\cdot\text{OH}$ and O_2^- which are produced as shown, further react with C_2Cl_4 to produce CO_2 and water, as represented in (Eq.7, 8) [31, 49s, SIP]. In the absence of suitable electron and hole scavengers, the stored energy is dissipated in a few nanoseconds, through recombination. In some works [50s-52s, SIP], researchers believe that carbon materials can generate photoelectrons and photo holes under UV irradiation. The C element is not directly involved in the photocatalytic process but can absorb UV light. After absorbing enough energy, these regions can generate photoelectrons and photoholes that can be transferred to TiO_2 . The results obtained show enhancement in the photocatalytic activity when the C element is doped on the surface of TiO_2 nanoparticles.



Based on observed products for $\text{TiO}_2\text{-C}$, several mechanisms of PCE degradation and intermediates have been described in the literature [14, 53s, 54s].

3.5. Photocatalyst stability

The stability of photocatalyst $\text{TiO}_2\text{-C}$ was investigated for a relatively long time to evaluate its capability of being applied in real systems in addition to examining its stability (Fig. 9). Figure 9 shows the change of degradation efficiency over relatively long periods for $\text{TiO}_2\text{-C}$ with 3000 ppm input concentration of PCE, 1min residence time and 30% RH under UV irradiation by the full intensity of the 8W 365 nm lamp. As seen for photocatalysts, first the degradation efficiency was increased and rich to 95% for $\text{TiO}_2\text{-C}$ respectively. No change over 5 hours' periods of time of irradiation were observed. Long term stability was also investigated for $\text{TiO}_2\text{-C}$ photocatalyst over 7 days (result not shown) at the same condition. No change in the stability and degradation efficiency were discernible over this period. These results showed degradation efficiency of $\text{TiO}_2\text{-C}$ was better than TiO_2 and relatively 50% more than TiO_2 and also a good stability over long period of time for $\text{TiO}_2\text{-C}$, indicating $\text{TiO}_2\text{-C}$ has good efficiency for photocatalytic degradation of PCE and is a good candidate for use in real systems.

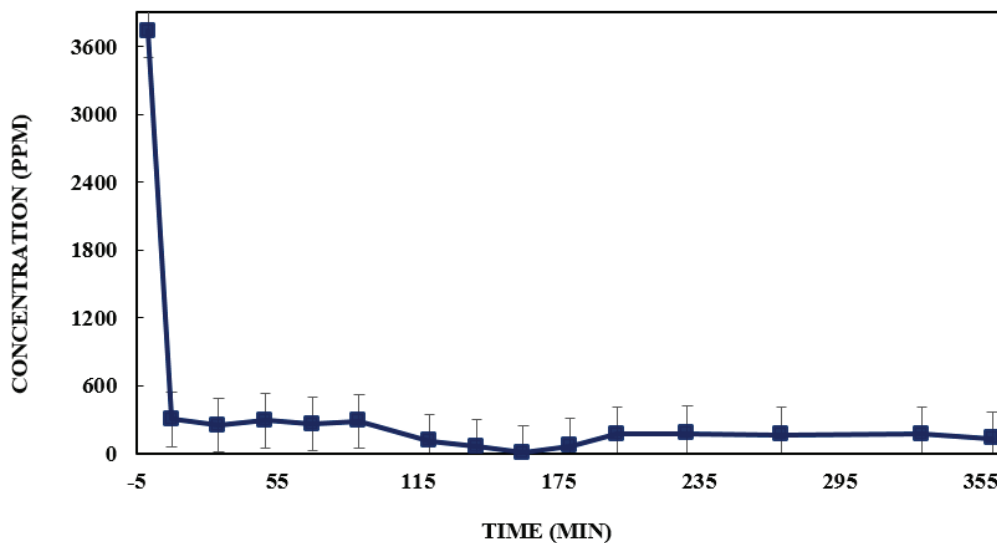


Fig. 9. Photocatalyst stability of $\text{TiO}_2\text{-C}$ over time 5 h

3.6. Comparison of TiO₂-C photocatalyst with other reported works

In Table 2, the different photocatalysts are compared in terms of lamp intensity, degradation wavelength, efficiency, and moisture content. Two factors of lamp power and temperature are very effective in degradation efficiency. On the other hand, in many previous studies, the method of determining the efficiency is expressed merely based on reducing the PCE output and does not consider the conversion of PCE to products and the production of CO₂. In terms of lamp power, the lamp used in the present study has a power of 8 (wat) and a wavelength of 365 nm in the UV region which was one of the least powerful lamps used in this field, indicating the high efficiency of the system due to the design of the lamp. In the center, its large reflection due to the aluminium sheet in the outer wall, the increase in

contact surface due to the use of glass balls and the proper selection of carbon contaminant. Also, the efficiency of the present research, despite the low power consumption (compared to the UV lamps), and the number of fewer lamps, are more or equal than to many previous reports.

4. Conclusions

In this project, a photocatalyst system with a fixed substrate and a light source in its center was used. In general, the system was designed to use all the power and efficiency of the catalysts, by increasing the reaction surface and the direct impact of light. In this system, an 8w fluorescent lamp with a wavelength of 365 nm was used as a source of UV light. The system was filled with glass balls coated with three catalysts (TiO₂, C-TiO₂) synthesized by the sol-gel method and uncoated balls to remove

Table.2. Comparison of TiO₂-C with photocatalysts reported in previous scientific papers

Lamp	Wavelength	Efficiency	Catalyst	Humidity	Reference
A Philips UV A lamp (Cleo performance 80W/10 Model)	The wavelength of 365 nm.	Is not limited	PC500	45 to 55%	[11]
Phillips, 4 W, F4 T5/BLB type	maximum emission at 365 nm	50%	-	-	[1]
three 8W black-light fluorescent lamps	light 365 nm	-	P25Pt/TiO ₂ and Pd/TiO ₂	-	[55s]
Philips TL 18W/08 F4T5/BLB	355nm	Predicted conversions show good	TiO ₂	48%	[56s]
five black light blue fluorescent lamps (Philips TL 8W/08 F8T5/BLB)	343 and 400	(55%)	(P-25)	8% relative humidity	[57s]
seven(Philips TL 4W/08 F4T5/BLB)	310 to 410 nm	24, 50, and 100%	TiO ₂	10, 50, and 90%	[58s]
Eight-4W fluorescent black light bulbs (Toshiba, FL 4BLB)	-	99.3%	TiO ₂	-	[59s]
A fluorescent black light bulb (Toshiba, FL 4BLB, 4 W)	-	80%	Porous TiO ₂	-	[60s]
1700 W air-cooled Xenon Lamps		Close to 100%	P25 and PC500	20%	[14]
Phillips UVC/8W/T5)	wavelength 365 nm.	99/6%	TiO ₂ -C	30%	Present study

the pollutants. Among these four samples, the highest and fastest total photocatalytic degradation efficiency was related to the TiO₂-C catalyst. The catalyst also had the highest stability and highest degradation efficiency. After degradation, all chemical products were determined by GC-MS analyzer.

5. Acknowledgements

The authors wish to thank from Research Institute of Petroleum Industry (RIPI), and University of Science and Technology, Narmak, Tehran, Iran for supporting this work.

6. References

- [1] K.-S. Lin, N.V. Mdllovu, C.-Y. Chen, C.-L. Chiang, K. Dehvari, Degradation of TCE, PCE, and 1,2-DCE DNAPLs in contaminated groundwater using polyethylenimine-modified zero-valent iron nanoparticles, *J. Clean. Prod.*, 175 (2018) 456-466. <https://doi.org/10.1016/j.jclepro.2017.12.074>
- [2] F.V. Lopes, R.A. Monteiro, A.M. Silva, G.V. Silva, J.L. Faria, A.M. Mendes, V.J. Vilar, R.A. Boaventura, Insights into UV-TiO₂ photocatalytic degradation of PCE for air decontamination systems, *Chem. Eng. j.*, 204 (2012) 244-257. <https://doi.org/10.1016/j.cej.2012.07.079>
- [3] A. Gupta, A. Pal, C. Sahoo, Photocatalytic degradation of a mixture of Crystal Violet (Basic Violet 3) and methyl red dye in aqueous suspensions using Ag⁺ doped TiO₂, *Dyes and Pigments*, 69 (2006) 224-232. <https://doi.org/10.1016/j.dyepig.2005.04.001>
- [4] A.G. Akerdi, S.H. Bahrami, Application of heterogeneous nano-semiconductors for photocatalytic advanced oxidation of organic compounds: A Review, *J. Environ. Chem. Eng.*, 7 (2019) 103283. <https://doi.org/10.1016/j.jece.2019.103283>
- [5] A. Fernandes, M. Gągol, P. Makoś, J.A. Khan, G. Boczkaj, Integrated photocatalytic advanced oxidation system (TiO₂/UV/O₃/H₂O₂) for degradation of volatile organic compounds, *Sep. Purif. Technol.*, 224 (2019) 1-14. <https://doi.org/10.1016/j.seppur.2019.05.012>
- [6] W.-K. Jo, J.-H. Park, H.-D. Chun, Photocatalytic destruction of VOCs for in-vehicle air cleaning, *J. Photochem. Photobiol. A: Chem.*, 148 (2002) 109-119. [https://doi.org/10.1016/S1010-6030\(02\)00080-1](https://doi.org/10.1016/S1010-6030(02)00080-1)
- [7] A. Babuponnusami, K. Muthukumar, Advanced oxidation of phenol: a comparison between Fenton, electro-Fenton, sono-electro-Fenton and photo-electro-Fenton processes, *Chem. Eng. J.*, 183 (2012) 1-9. <https://doi.org/10.1016/j.cej.2011.12.010>
- [8] H. Shemer, Y.K. Kunukcu, K.G. Linden, Degradation of the pharmaceutical metronidazole via UV, Fenton and photo-Fenton processes, *Chemosphere*, 63 (2006) 269-276. <https://doi.org/10.1016/j.chemosphere.2005.07.029>
- [9] K. Li, M.I. Stefan, J.C. Crittenden, Trichloroethene degradation by UV/H₂O₂ advanced oxidation process: product study and kinetic modeling, *Environ. Sci. Technol.*, 41 (2007) 1696-1703. <https://doi.org/10.1021/es0607638>
- [10] K. Sivagami, R.R. Krishna, T. Swaminathan, Photo catalytic degradation of pesticides in immobilized bead photo reactor under solar irradiation, *Solar Energ.*, 103 (2014) 488-493. <https://doi.org/10.1016/j.solener.2014.02.001>
- [11] N. Petit, A. Bouzaza, D. Wolbert, P. Petit, J. Dussaud, Photocatalytic degradation of gaseous perchloroethylene in continuous flow reactors: rate enhancement by chlorine radicals, *Catalysis Today*, 124(2007)266-272. <https://doi.org/10.1016/j.cattod.2007.03.050>
- [12] L.B.B. Ndong, M.P. Ibondou, X. Gu, M. Xu, S. Lu, Z. Qiu, Q. Sui, S.M. Mbadinga, Efficiently synthetic TiO₂ nano-sheets for PCE, TCE, and TCA degradations in aqueous phase under VUV irradiation, *Water, Air, Soil Pollut.*, 225 (2014) 1951. <https://doi.org/10.1007/s11270-014-1951-8>
- [13] S. Yamazaki, T. Tanimura, A. Yoshida, K. Hori, Reaction mechanism of photocatalytic

- degradation of chlorinated ethylenes on porous TiO₂ pellets: Cl radical-initiated mechanism, *J. Phys. Chem. A*, 108 (2004) 5183-5188. <https://doi.org/10.1021/jp0311310>
- [14] R.A. Monteiro, A.M. Silva, J.R. Ângelo, G.V. Silva, A.M. Mendes, R.A. Boaventura, V.J. Vilar, Photocatalytic oxidation of gaseous perchloroethylene over TiO₂ based paint, *J. Photochem. Photobiol. A Chem.*, 311 (2015) 41-52. <https://doi.org/10.1016/j.jphotochem.2015.06.007>
- [15] H. Yu, S. Lee, J. Yu, C. Ao, Photocatalytic activity of dispersed TiO₂ particles deposited on glass fibers, *J. Mol. Catal. A Chem.*, 246 (2006) 206-211. <https://doi.org/10.1016/j.molcata.2005.11.007>
- [16] A. Basso, A.P. Battisti, R.d.F.P.M. Moreira, H.J. José, Photocatalytic effect of addition of TiO₂ to acrylic-based paint for passive toluene degradation, *Environ. Technol.*, (2018) 1-12. <https://doi.org/10.1080/09593330.2018.1542034>
- [17] H. Rasoulnezhad, G. Hosseinzadeh, R. Hosseinzadeh, N. Ghasemian, Preparation of transparent nanostructured N-doped TiO₂ thin films by combination of sonochemical and CVD methods with visible light photocatalytic activity, *J. Adv. Ceram.*, 7 (2018) 185-196. <https://creativecommons.org/licenses/by/4.0/>.
- [18] S. Yamazaki, H. Tsukamoto, K. Araki, T. Tanimura, I. Tejedor-Tejedor, M.A. Anderson, Photocatalytic degradation of gaseous tetrachloroethylene on porous TiO₂ pellets, *Appl. Catal. B Environ.*, 33 (2001) 109-117. [https://doi.org/10.1016/S0926-3373\(01\)00167-9](https://doi.org/10.1016/S0926-3373(01)00167-9)
- [19] C. Martins, A.L. Cazetta, O. Pezoti, J.R. Souza, T. Zhang, E.J. Pilau, T. Asefa, V.C. Almeida, Sol-gel synthesis of new TiO₂/activated carbon photocatalyst and its application for degradation of tetracycline, *Ceram. Int.*, 43 (2017) 4411-4418. <https://doi.org/10.1016/j.ceramint.2016.12.088>
- [20] Y. Liang, B. Zhou, N. Li, L. Liu, Z. Xu, F. Li, J. Li, W. Mai, X. Qian, N. Wu, Enhanced dye photocatalysis and recycling abilities of semi-wrapped TiO₂@ carbon nanofibers formed via foaming agent driving, *Ceram. Int.*, 44 (2018) 1711-1718. <https://doi.org/10.1016/j.ceramint.2017.10.101>
- [21] F.H. Abdulrazzak, Enhance photocatalytic activity of TiO₂ by carbon nanotubes, *Int. J. Chem. Tech. Res.*, 9 (2016) 431-443. <https://sphinxsai.com/chemtech.php>
- [22] H. Liang, Z. Jia, H. Zhang, X. Wang, J. Wang, Photocatalysis oxidation activity regulation of Ag/TiO₂ composites evaluated by the selective oxidation of Rhodamine B, *Appl. Surf. Sci.*, 422 (2017) 1-10. <http://dx.doi.org/10.1016/j.apsusc.2017.05.211>
- [23] D. Zhang, J. Chen, P. Deng, X. Wang, Y. Li, T. Wen, Y. Li, Q. Xiang, Y. Liao, Hydrogen evolution promotion of Au-nanoparticles-decorated TiO₂ nanotube arrays prepared by dip-loading approach, *J. Am. Ceram. Soc.*, 109 (2019) 5873-5880. <https://doi.org/10.1111/jace.16441>
- [24] A. Martinez-Oviedo, S.K. Ray, H.P. Nguyen, S.W. Lee, Efficient photo-oxidation of NO_x by Sn doped blue TiO₂ nanoparticles, *J. Photochem. Photobiol. A Chem.*, 370 (2019) 18-25. <https://doi.org/10.1016/j.jphotochem.2018.10.032>
- [25] B. Niu, Z. Xu, From E-waste to Nb-Pb Co-doped and Pd-loaded TiO₂/BaTiO₃ heterostructure: highly efficient photocatalytic performance, *Chem. Sus. Chem.*, 12 (2019) 2819-2828. <https://doi.org/10.1002/cssc.201900071>.
- [26] H. She, H. Zhou, L. Li, L. Wang, J. Huang, Q. Wang, Nickel-doped excess oxygen defect titanium dioxide for efficient selective photocatalytic oxidation of benzyl alcohol, *ACS Sus. Chem. Eng.*, 6 (2018) 11939-11948. <https://doi.org/10.1021/acssuschemeng.8b02217>
- [27] L. Zhang, W. Yu, C. Han, J. Guo, Q. Zhang, H. Xie, Q. Shao, Z. Sun, Z. Guo, Large scaled synthesis of heterostructured electrospun TiO₂/SnO₂ nanofibers with an enhanced

- photocatalytic activity, *J. Electrochem. Soc.*, 164 (2017) H651-H656. <https://doi.org/10.1149/2.1531709jes>
- [28] F. Dong, S. Guo, H. Wang, X. Li, Z. Wu, Enhancement of the Visible Light Photocatalytic Activity of C-Doped TiO₂ Nanomaterials Prepared by a Green Synthetic Approach, *J. Phys. Chem. C*, 115 (2011) 13285-13292. <https://doi.org/10.1021/jp111916q>
- [29] G.B. Soares, B. Bravin, C.M. Vaz, C. Ribeiro, Facile synthesis of N-doped TiO₂ nanoparticles by a modified polymeric precursor method and its photocatalytic properties, *App. Catal. B Environ.*, 106 (2011) 287-294. <https://doi.org/10.1016/j.apcatb.2011.05.018>
- [30] H. Li, D. Wang, H. Fan, P. Wang, T. Jiang, T. Xie, Synthesis of highly efficient C-doped TiO₂ photocatalyst and its photo-generated charge-transfer properties, *J. Colloid Interface Sci.*, 354 (2011) 175-180. <https://doi.org/10.1016/j.jcis.2010.10.048>
- [31] T.-D. Pham, B.-K. Lee, Novel adsorption and photocatalytic oxidation for removal of gaseous toluene by V-doped TiO₂/PU under visible light, *J. Hazard. Mater.*, 300 (2015) 493-503. <https://doi.org/10.1016/j.jhazmat.2015.07.048>
- [32] J. Zhao, X. Yang, Photocatalytic oxidation for indoor air purification: a literature review, *Build. Environ.*, 38 (2003) 645-654. [https://doi.org/10.1016/S0360-1323\(02\)00212-3](https://doi.org/10.1016/S0360-1323(02)00212-3)
- [33] J. Mo, Y. Zhang, Q. Xu, J.J. Lamson, R. Zhao, Photocatalytic purification of volatile organic compounds in indoor air: A literature review, *Atmos. Environ.*, 43 (2009) 2229-2246. <https://doi.org/10.1016/j.atmosenv.2009.01.034>
- [34] M. Behpour, V. Atouf, Study of the photocatalytic activity of nanocrystalline S, N-codoped TiO₂ thin films and powders under visible and sun light irradiation, *Appl. Surf. Sci.*, 258 (2012) 6595-6601. <https://doi.org/10.1016/j.apsusc.2012.03.085>
- [35] T. Sugimoto, X. Zhou, A. Muramatsu, Synthesis of uniform anatase TiO₂ nanoparticles by gel-sol method: 3. Formation process and size control, *J. Colloid Interface Sci.*, 259 (2003) 43-52. [https://doi.org/10.1016/S0021-9797\(03\)00036-5](https://doi.org/10.1016/S0021-9797(03)00036-5)
- [36] G. Wu, T. Nishikawa, B. Ohtani, A. Chen, Synthesis and characterization of carbon-doped TiO₂ nanostructures with enhanced visible light response, *Chem. Mater.*, 19 (2007) 4530-4537. <https://doi.org/10.1021/cm071244m>
- [37] S.Y. Treschev, P.-W. Chou, Y.-H. Tseng, J.-B. Wang, E.V. Perevedentseva, C.-L. Cheng, Photoactivities of the visible-light-activated mixed-phase carbon-containing titanium dioxide: The effect of carbon incorporation, *Appl. Catal. B Environ.*, 79 (2008) 8-16. <https://doi.org/10.1016/j.apcatb.2007.09.046>
- [38] J. Abisharani, S. Devikala, R.D. Kumar, M. Arthanareeswari, P. Kamaraj, Green synthesis of TiO₂ Nanoparticles using Cucurbita pepo seeds extract, *Mater. Today: Proc.*, 14 (2019) 302-307. <https://doi.org/10.1016/j.matpr.2019.04.151>
- [39] A. Wanag, E. Kusiak-Nejman, J. Kapica-Kozar, A.W. Morawski, Photocatalytic performance of thermally prepared TiO₂/C photocatalysts under artificial solar light, *Micro & Nano Letters*, 11 (2016) 202-206. <https://doi.org/10.1049/mnl.2015.0507>
- [40] P. Zhang, C. Shao, Z. Zhang, M. Zhang, J. Mu, Z. Guo, Y. Liu, TiO₂@ carbon core/shell nanofibers: controllable preparation and enhanced visible photocatalytic properties, *Nanoscale*, 3 (2011) 2943-2949. <https://doi.org/10.1039/C1NR10269A>
- [SIP] SIP references (41-60s) have showed in supporting information page, <http://journal.amecj.com/index.php/AMECJ-01>



Separation and determination of lithium and manganese ions in healthy humans and multiple sclerosis patients based on nanographene oxide by ultrasound assisted-dispersive -micro solid-phase extraction

Seyed Majid Nabipour Haghighi^a and Negar Motakef Kazemi^{*a}

^a Department of Medical Nanotechnology, Faculty of Advanced Sciences and Technology, Tehran Medical Sciences, Islamic Azad University, Tehran, Iran.

ARTICLE INFO:

Received 3 Sep 2021

Revised form 6 Nov 2021

Accepted 30 Nov 2021

Available online 29 Dec 2021

Keywords:

Lithium, Manganese,
Human samples,
Multiple sclerosis patients,
Nano graphene oxide,
Ultrasound assisted-dispersive-micro-
solid phase extraction

ABSTRACT

Lithium regulates the concentration of nitric oxide in the human body and a high dose of nitric oxide causes multiple sclerosis (MS). Also, the amount of manganese in the cerebrospinal fluid alters the metabolic reactions associated with MS. In this study, the mixture of the ammonium pyrrolidine dithiocarbonate (APDC), the hydrophobic ionic liquid [HMIM][PF6] and acetone coated on the surface of graphene oxide nanoparticles (GONPs) and used for separation Li and Mn in human samples by ultrasound assisted-dispersive-ionic liquid-micro-solid phase extraction technique (USA-DIL- μ -SPE) at pH 6.0. After extraction and back-extraction, the amount of lithium and manganese in the blood, serum and urine samples was determined by the flame and the graphite furnace atomic absorption spectroscopy (F-AAS, GF-AAS), respectively. By optimizing parameters, the LOD, Linear ranges (LR) and preconcentration factor (PF) for Li and Mn ions were obtained (0.03 mg L⁻¹, 0.25 μ g L⁻¹), (0.1-0.4 mg L⁻¹, 0.08-1.5 μ g L⁻¹) and 10, respectively (%RSD<5). The capacity adsorption of APDC/IL/GONPs and GONPs was achieved (148.5 mg g⁻¹, 122.3 mg g⁻¹) and (41.3 mg g⁻¹, 33.7 mg g⁻¹) for Li and Mn ions in a static system, respectively. This method was successfully validated by spiking samples and certified reference materials (CRM).

1. Introduction

Multiple sclerosis (MS) is the most common chronic inflammatory disease of the central nervous system (CNS), affecting more than 2 million people worldwide and is currently incurable. No drug can completely prevent progressive neurodegeneration, which is usually diagnosed with impaired movement function, bladder control, and cognitive processes [1, 2].

Nitric oxide and its metabolites in the human body may be involved in the pathogenesis of several neurological disorders such as multiple sclerosis. Several studies have shown that lithium regulates NO levels in the central nervous system. High levels of compounds derived from reactive oxygen species (ROS) and reactive nitrogen species (RNS) have been detected in blood samples from RR-MS patients. In principle, increased production of NO and its metabolites in the peripheral blood of these patients has been shown [3]. Lithium may control NO formation in MS. There is a significant difference between

*Corresponding Author: Negar Motakef Kazemi

Email: motakef@iaups.ac.ir

<https://doi.org/10.24200/amecj.v4.i04.158>

serum lithium levels in RR-MS patients and healthy individuals. Extensive experimental and clinical studies show that lithium has protective effects on the pathogenesis of neurological diseases through several mechanisms (activation of nerve pathways, regulation of oxidative stress, anti-inflammatory responses, regulation of mitochondrial function, etc.). However, the use of high doses of lithium may lead to toxic effects [4]. Excessive accumulation of metal in the CNS stimulates oxidative stress, mitochondrial dysfunction, dysfunction of enzymes structural, regulatory, and catalytic functions in a variety of proteins, receptors, and carriers. Metals can cause nerve damage in PD, AD, and MS by disrupting mitochondrial function. The mechanism act with lower adenosine triphosphate (ATP) and produces ROS. Through these mechanisms, metals cause cell death by apoptotic or necrotic mechanisms [5]. Also, manganese is toxic to the CNS in excessive amounts. High manganese value can lead to a disease whose symptoms are similar to those of Parkinson's. Manganism is a type of extrapyramidal movement disorder of the Parkinson's type that has impaired motor and cognitive impairment due to neural processes [6]. Determination of metal ions in blood and body fluids can play an effective role in diagnosing the disease and various treatments. The characterization of nanomaterials in various fields, especially in medical science, caused to use for the determination of metals in human body fluids. Recently, the nanoparticles such as graphene oxide and activated carbon were used to measure the concentration of lead, mercury, lithium, silver and manganese ions in patients. For this purpose, a micro-extraction procedure based on solid-phase or liquid phase coupled to ultrasound was used to measure ions by atomic absorption spectroscopy [7]. Due to the toxicity of Li and Mn in the human body, its concentration must be determined in blood, serum and urine samples. Many technologies have been used for Li and Mn determination in different samples including, the isotope dilution atomic absorption

spectrometry (ID-ET-AAS) for Li determination in serum samples. ID-ET-AAS based on the partially resolved isotope shift was done by graphite furnace atomic absorption spectrometer [8]. Also, flame emission(FES), flame atomic absorption spectroscopy (F-AAS) and ion-selective electrode (ISE) were used for lithium determination in human patients [9, 10]. The concentration of beryllium, copper, chromium, cobalt, nickel, magnesium and iron in the blood of MS patients was determined by ICP-MS [11]. Moreover, the inductively coupled plasma sector field mass spectrometry (ICP-SFMS) and MC-ICP-MS was used for Li determination in serum samples [12, 13]. The Li in human samples was determined by high-resolution atomic absorption spectrometry (HR-AAS) and machine learning data(MLD) [14]. In addition, Mn ions in herbal teas were evaluated by FAAS and ICP-OES [15]. The cation exchange chromatography coupled to field ICP-MS was used for Mn determination in cerebrospinal fluid [16]. As in previous research, the Li and Mn were determined in metals of human blood samples by AAS after sample preparation techniques. Recently, the different treatments such as; the dispersive liquid-liquid microextraction (DLLME) [17], the cloud point extraction procedure (CPE) [18], and the solid-phase extraction (SPE) [19, 20] were used for metal analysis in various samples. Among them, the SPE as low cost, simple and good recovery is preferred to other methods.

In this research, a new adsorbent based on APDCIL/GONPs was used for extraction of Li and Mn in human biological samples by USA-DIL- μ -SPE procedure. Li and Mn ions were determined by F-AAS and ET-AAS, respectively after sample treatment. The method was validated by spiking real samples and CRM analysis in human blood, serum and urine samples.

2. Experimental

2.1. Instruments

The different instruments include a magnetic stirrer (Four E'S Scientific, model MI0102003)

with a variable speed made in china, a digital scale with an accuracy of one-thousandth of a gram made in Japan, a digital pH meter model 744 made in Switzerland, centrifuge with 3500-4000 rpm made in Iran (IRANLABXPO), hematocrit centrifuge with 12,000 rpm (AHN myLab® hematocrit centrifuge, AHN Biotechnologie GmbH, Germany), a magnetic heater, oven (Iran Lab), Austrian microwave device (Anton Paar, Vienna Austria), the sharp polyethylene pipes and Pyrex glass, the tube and balloon mixer, and the automatic sampling for different volumes between 0.01 mL to 1 mL were used in this research. The Mn and Li concentration was determined by flame atomic absorption spectrometer (FAAS, GBC 906, double beam, Aus.). The air-acetylene (C_2H_2), the deuterium lamp was used for Li evaluation. The limit of detection (LOD) and linear range of F-AAS for Li-ions in standard solutions was obtained 0.32 mg L^{-1} and $1\text{-}4 \text{ mg L}^{-1}$, respectively. The light of HCL for lithium was adjusted by maximum energy at a wavelength of 670.8 nm, slit of 0.5 nm and 5.0 mA. The ultra-trace analyzer, the electrothermal atomic absorption spectrophotometer (ET-AAS, GBC, Aus.) was used for the determination of Mn in human blood samples. The limit of detection (LOD) and linear range of Mn ions with ET-AAS was obtained $0.27 \text{ } \mu\text{g L}^{-1}$ and $2.5\text{-}15 \text{ } \mu\text{g L}^{-1}$, respectively. The Avanta software was used for calculating absorption results by the F-AAS and ET-AAS.

2.2. Reagents

The ultra-pure reagents were purchased from the Merck or Sigma Companies (Germany). All standard solutions and samples were diluted by ultra-pure distilled water (DW, $R \geq 18 \text{ M}\Omega \text{ cm}^{-1}$) from Millipore (Bedford, USA). The standard stock solution of lithium (LiCl , CASN: 7447-41-8) and manganese (MnCl_2 , CAS N.: 189302-40-7) was purchased from Sigma Aldrich (1000 mg L^{-1} in 1% nitric acid 500 mL). The calibration standard solutions of lithium (0.1, 0.2, 0.3, 0.4 mg L^{-1}) and manganese ($0.1\text{-}1.5 \text{ } \mu\text{g}$

L^{-1}) were prepared by diluting of stock solution with DW (1000 mg L^{-1}). Nitric acid (HNO_3), hydrochloric acid (HCl, CAS N.: 7647-01-0), sodium hydroxide (NaOH, CAS N.: 1310-73-2), potassium hydroxide (KOH, CAS N.: 1310-58-3), and all other reagents were purchased from Merck, Germany. The pH was adjusted by suitable buffer solutions. The different buffer solutions such as the sodium phosphate ($\text{H}_3\text{PO}_4 / \text{NaH}_2\text{PO}_4$, 0.15 mol L^{-1}) for pH 1.5-3, the ammonium acetate buffer ($\text{CH}_3\text{COOH} / \text{CH}_3\text{COONa}$) for pH 4-5.5, the sodium borate (NaBO_2/HCl) for pH 7 and the ammonium chloride ($\text{NH}_3/\text{NH}_4\text{Cl}$) were used for pH 8-10. Graphene oxide was prepared by the Petroleum Industry Research Institute (RIPI) and coated with a mixture of ionic liquid/APDC (99%, ammonium pyrrolidine dithiocarbonate, CAS N.: 5108-96-3, EC Number: 225-834-4) and acetone. Hydrophobic ionic liquid (1-Hexyl-3-methylimidazolium hexafluorophosphate, $[\text{HMIM}][\text{PF}_6]$, CAS N.: 304680-35-1) was prepared from Sigma, Germany.

2.3. Synthesis of APDC-IL coated on graphene oxide

The graphite oxide was prepared by modified Hummer technique by oxidation of natural graphite powder in the laboratory of RIPI. The GO was prepared by peeling off graphite oxide. First, 5 g of graphite powder and 2.5 g of NaNO_3 were combined with 120 mL H_2SO_4 (98%) and shaken vigorously for 30 min in an ice bath ($0\text{-}5 \text{ }^\circ\text{C}$). Simultaneously with stirring, 15 g of KMnO_4 was gradually added, and the temperature was tuned at below $15 \text{ }^\circ\text{C}$. The ice bath was then removed, and the mixture was stirred at $35 \text{ }^\circ\text{C}$ until it gradually turned brown form and then diluted gently with 250 mL of water. The reaction temperature rose rapidly to $98 \text{ }^\circ\text{C}$ with boiling and its colour changed to dark brown. Then, 30% H_2O_2 solution was added, and the colour of the mixture changed to a bright yellow colour, indicating complete oxidation of graphene. The graphene oxide was washed by rinsing and centrifugation with

dilute hydrochloride solution and then continued several times with deionized distilled water to neutralize the filtered solution. The graphene oxide suspension was centrifuged and sonicated for 15 minutes at 3000 rpm to obtain graphene oxide nanosheets. Finally, the prepared GONPs was air-dried for two hours in two stages at 55 °C. Ammonium pyrrolidine dithiocarbamate (APDC) was mixed with ionic liquid 1-hexyl-3-methylimidazolium hexafluorophosphate (hydrophobic) in the presence of acetone at 25 °C for 10 minutes. Then an organic mixture (ionic liquid, acetone, ammonium pyrrolidine dithiocarbamate) was used at 55 °C for coating of graphene oxide (IL /APDC-NGO) [21-23].

2.4. General Procedure

By procedure, a sample of lithium was prepared by diluting 1 ml of blood, urine and serum sample

with DW up to 10 mL. Also, 10 mL of human biological samples were used for manganese separation at optimized pH. 25 mg of APDC/IL/GONPs adsorbent was used to separate lithium and manganese ions from the blood, serum and urine of MS patients by the ultrasound assisted-dispersive-ionic liquid-micro-solid phase extraction technique (USA-DIL- μ -SPE). The standard solution of lithium (0.1 - 0.4 mg L⁻¹) and manganese (0.1 - 1.5 μ g L⁻¹) as the lower and upper limit of quantification (LLOQ, ULOQ) were used. After adding adsorbent to the human samples, it was placed in an ultrasonic bath for 5 minutes and the lithium and manganese ions were physically and chemically adsorbed by a sulfur bond of APDC ligand and the surface of the graphene oxide, respectively ($Mn^{+2}/Li^{+} \rightarrow NGO$; $Mn^{+2}/Li^{+} \rightarrow S-IL-NGO$). By the proposed

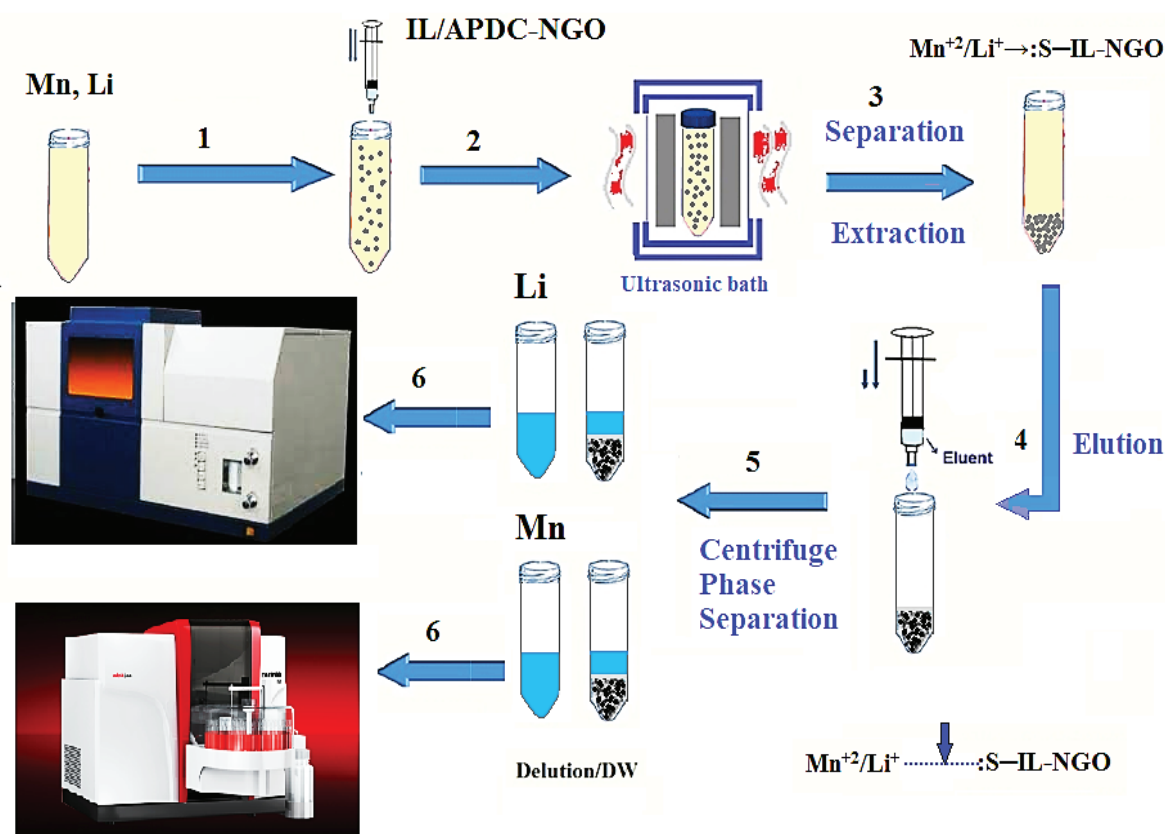


Fig. 1. Determination and separation lithium and manganese ions in human biological samples based on APDC/IL/GONPs by USA-DIL- μ -SPE procedure

procedure, lithium (Li) and manganese (Mn) ions are extracted by coordinate covalent bond at pH 5 and 6, respectively (more than 95%). The results showed us, at high pH, lithium and manganese ions were precipitated as hydroxide ions ($\text{Mn}(\text{OH})_2$ and LiOH). After the separated phase by centrifuging (3 min, 3500 rpm), the extracted lithium and manganese ions were trapped in the bottom of the conical tube by IL/GONPs. Then, the upper liquid phase was set aside with an auto-sampler and the loaded ions on the adsorbent (APDC/IL/GONPs) were back-extracted by the nitric acid solution (500 μL , 0.3 M) by shaking and centrifuging for 1 minute. Finally, the concentration of lithium and manganese ions was determined by the F-AAS and ETAAS, respectively after diluting eluent up to 1 mL with 0.5 ml of DW. Also, the extraction/separation of lithium and manganese ions based on GONPs in human biological samples and the standard solution was investigated in various pH. For urine analysis, 10 mL of sample was used under similar conditions. For validation of the method, the standard reference materials (SRM) and spike samples were used for standard and human samples. For calibration of lithium and manganese ions, 10 mL of a standard aqueous sample containing lithium (0.05, 0.1, 0.2, 0.3 and 0.4 mg L^{-1}) and manganese (0.1, 0.2, 0.4, 0.5, 1.0, 1.5 $\mu\text{g L}^{-1}$) were prepared from stock

solutions. In addition, the ICP-MS were used to validate the real samples.

3. Results and Discussion

3.1. Characterization of APDC/IL/graphene oxide

Fourier transform infrared (FT-IR) spectra were recorded by a Perkin Elmer spectrophotometer. The X-ray diffraction (XRD) was obtained based on a Panalytical X'Pert PRO X-ray diffractometer. The Bruker (D) FRA-106/S spectrometer was used for Raman spectra. Scanning electron microscopy (SEM) images were reported by a Tescan Mira-3. The transmission electron microscopes images (TEM, JEM 2100 plus) was achieved by JEOL Company, Germany.

3.1.1. Electron microscope images

As Figure 2(a, b) and 3(a, b), the scanning electron microscopy (SEM) and transmission electron microscope (TEM) images show that the APDC/IL/GONPs and GONPs has similar multi-layered with a smooth surface and some with folds. Wrinkled areas are at the APDC/IL/GONPs and GONPs level due to the presence of oxygenated functional groups (such as carboxyl, hydroxyl, and carbonyl). The APDC/IL/GONPs and GONPs both consist of randomly accumulated and wrinkled thin sheets.

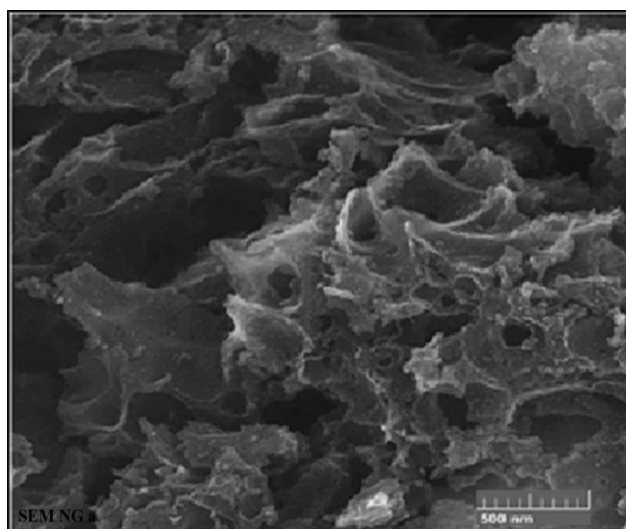


Fig. 2a. SEM image of APDC/IL/GONPs

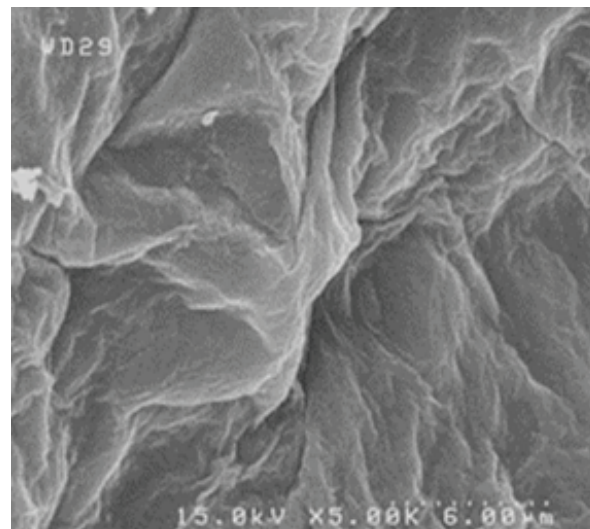


Fig. 2b. SEM image of GONPs

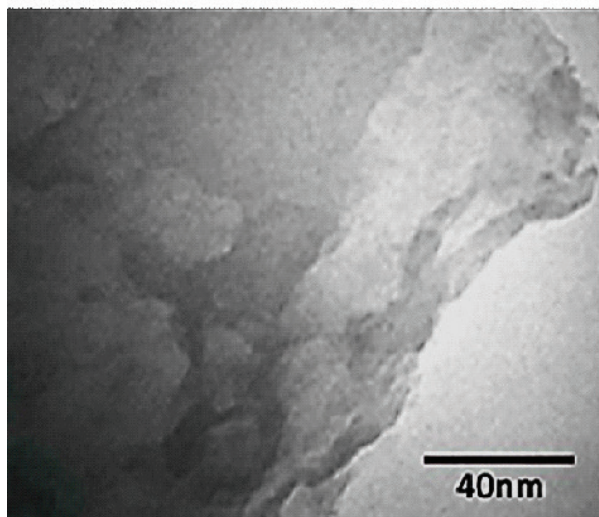


Fig. 3a. TEM image of APDC/IL/GONPs

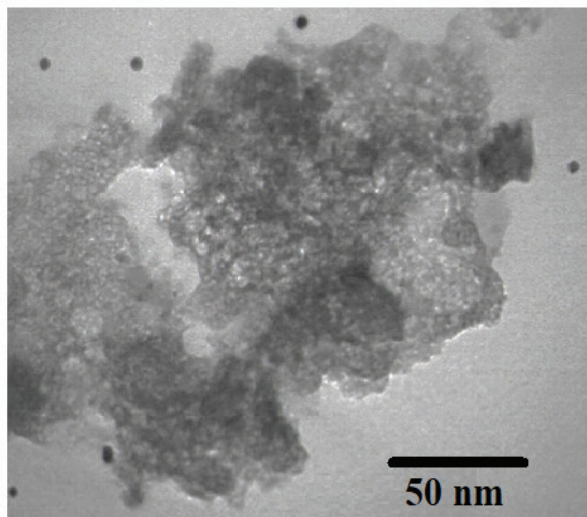


Fig. 3b. TEM image of GONPs

3.1.2. XRD and FT-IR analysis

In the XRD analysis of graphene oxide, a sharp peak was observed at $2\theta = 12.267$ ($d = 0.723$) with the usual GONPs nanoparticle diffraction peak. The distance d increases from 0.33 to 0.72 nm after the conversion of graphite to graphene oxide nanoparticles, which may be due to the formation of abundant oxygenated functional groups on the graphene oxide surface. In addition, the peaks at $2\theta = 12^\circ$ and $2\theta = 42.58^\circ$ are related to the diffraction planes of (002) and (100) respectively, which can be observed in the XRD patterns of both GONPs

and APDC/IL/GONPs. It showed that the XRD intensity of the peak at $2\theta = 12^\circ$ for the APDC/IL-coated on GONPs was significantly decreased (Fig.4a and b).

Oxygenated functional groups on the surface of graphene oxide nanoparticles by FT-IR analysis can be seen in the following diagram. Accordingly, the groups C=O and COOH/OH are represented by the peak of 1728 cm^{-1} and 3300 cm^{-1} , respectively. The C-O bonding is shown at peak 1011 cm^{-1} and the peak C=C is located at 1590 cm^{-1} by FTIR. As physically coated APDC/IL on GONPs any peak wasn't added to FTIR of GO (Fig.5).

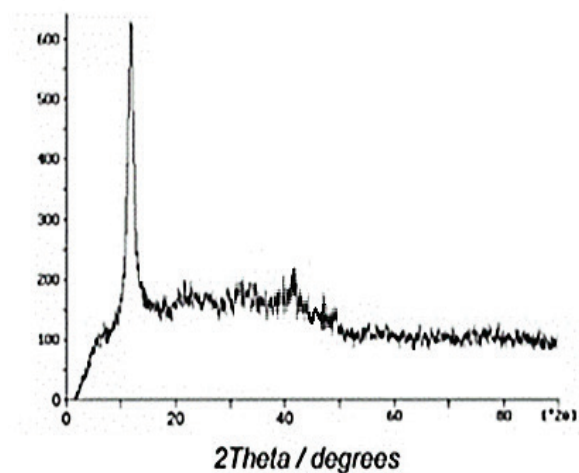


Fig. 4a. XRD of the GONPS

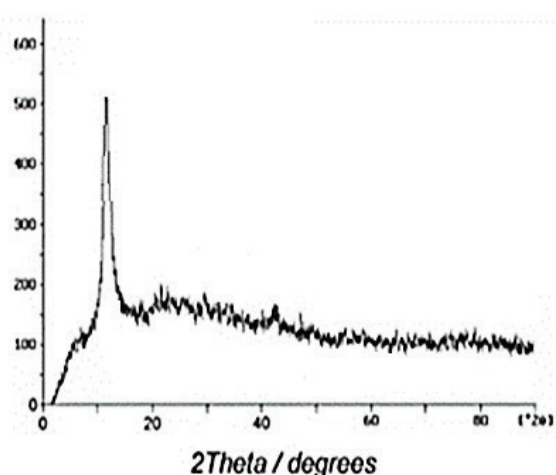


Fig. 4b. XRD of the APDC/IL/GONPS

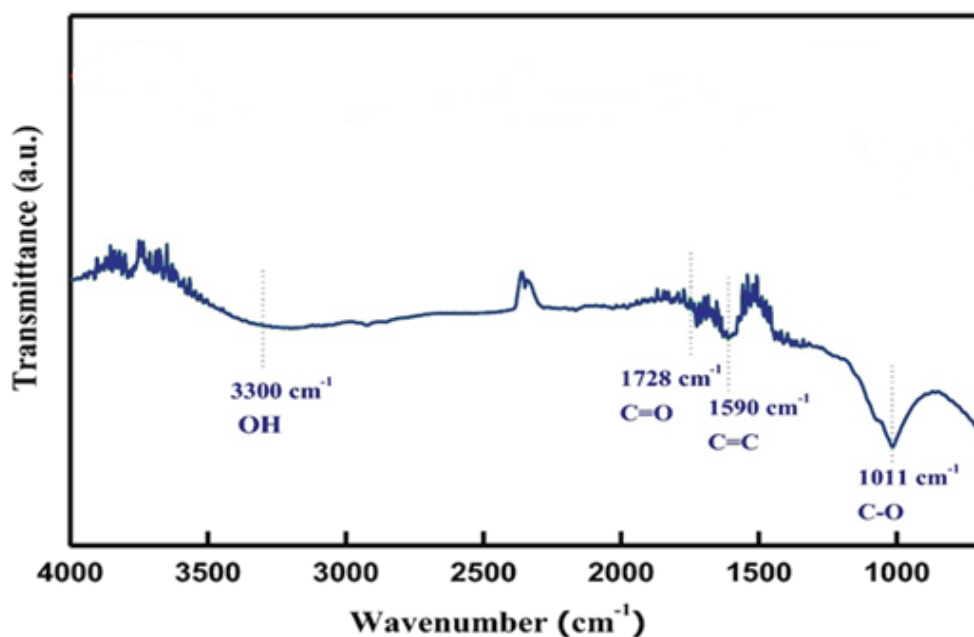


Fig.5. FT-IR analysis of the APDC/IL/GONPs

3.2. Optimization of Method

To achieve optimal conditions in solid-phase extraction for preconcentration/separation of lithium and manganese in human biological samples, the parameters such as pH, the amount of sorbent, the sample volume, the amount of ionic liquid, the concentration of APDC ligand, the shaking and centrifuge time, were investigated.

3.2.1. The pH optimization

The pH effects on the extraction of Li and Mn ions by APDC/IL/GONPs. So, the various pH between 2-11 was studied for Li and Mn extraction in human biological matrixes. The results showed, the sulfur group on the surface of GONPs adsorbent was caused to extraction Li and Mn ions at pH of 5-7. Due to the mechanism, the extraction was reduced at $\text{pH} < 5$ and $\text{pH} > 7$. Therefore, we used $\text{pH}=6$ for Li and Mn extraction in human biological samples (blood, serum, urine). The mechanism of absorption of Li and Mn ions was obtained based on the sulfur group (SH) on the surface of APDC/IL/GONPs. By a sulfur group of APDC, the coordinate covalent bond with Li and Mn ions in human liquid samples

was achieved ($\text{Mn}^{2+}/\text{Li}^+ \rightarrow \text{S-IL-NGO}$). At $\text{pH} < \text{pH}_{\text{PZC}}$, the adsorbent had a positive charge and due to similarity charges between Li and Mn and adsorbent, the extraction was decreased. Also, in pH 5 for Li and pH 6 for Mn, the surface of APDC/IL/GONPS based on negatively charged (HS^-) coordinated with a positive charge of Li and Mn. At pH more than 7, Li and Mn ions have participated as hydroxyl forms (Li OH , $\text{Mn}(\text{OH})_2$). Therefore, we used $\text{pH}=6$ for further studies (Fig. 6).

3.2.2. Optimization of adsorbent amount

The efficient extraction of Li and Mn ions in human samples were studied by different amount of APDC/IL/GONPs. For this purpose, the various mass of APDC/IL/GONPs was evaluated at $\text{pH}=6$. For Li and Mn extraction, 2-40 mg of APDC/IL/GONPs in blood, serum, urine and standard solution were studied and optimized by the USA-DIL- μ -SPE procedure. Based on the results, the efficient extractions for Li and Mn ions were obtained by 20 mg of adsorbent in human biological samples. So, 25 mg of APDC/IL/GONPs was used for further study (Fig. 7).

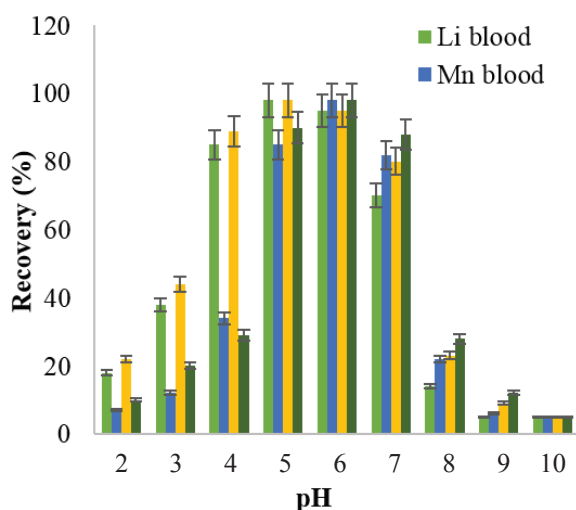


Fig.6. The effect of pH on Li/Mn extraction

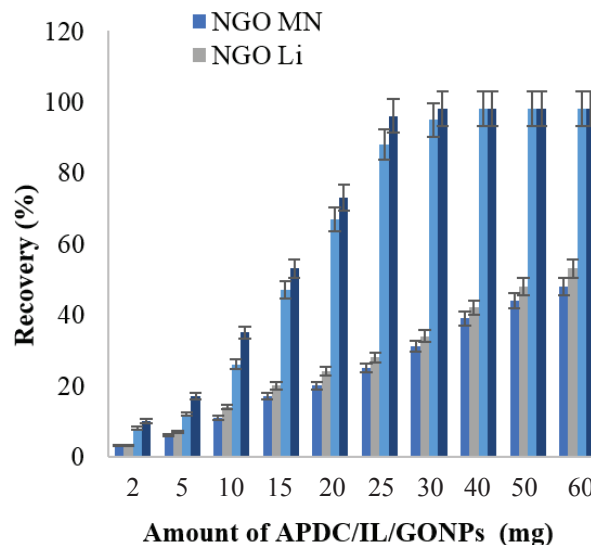


Fig.7. The effect of adsorbent mass on Li /Mn extraction

3.2.3. Optimization of sample volume and eluent

The effect of eluent on extraction Li and Mn ions based on APDC/IL/GONPs were studied at optimized pH. At low pH, the covalent bond between the metal and sulfur group was dissociated and the Li and Mn ions released into liquid phase. Therefore, the inorganic acid solutions with different concentrations and volumes (HCl, HNO₃, H₃PO₄, H₂SO₄) were used to evaluate the recovery of the back-extraction process for Li and

Mn ions in human biological samples. The eluent concentrations between 0.2-2.0 mol L⁻¹ was studied. The efficient extraction was obtained by HNO₃ (0.5 M, 0.25 mL) (Fig. 8). Also, the volume of human samples and the standard solution was evaluated from 2.0 mL to 20 mL for Li and Mn concentration (0.1-0.4 mg L⁻¹, 0.1-1.5 µg L⁻¹). As result, the high recovery occurred for 10 mL of human biological samples at pH 5-7 (Fig.9).

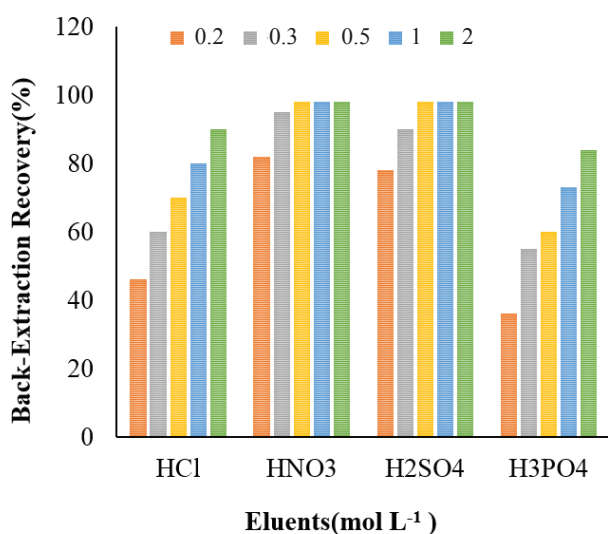


Fig.8. The effect of eluents on Li/Mn back-extraction

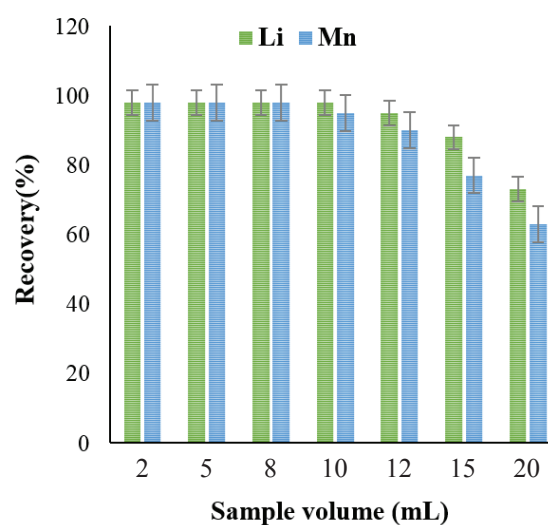


Fig.9. The effect of sample volume on Li /Mn extraction

3.2.4. Optimization of APDC ligand on adsorbent

The concentration of APDC is one of the important parameters which should be optimized by the USA-DIL- μ -SPE procedure method. For optimizing, 0.1×10^{-6} - 1.0×10^{-6} mol L⁻⁶ of APDC ligand was used in the human biological sample. The results showed that, by increasing ligand concentration up to 0.5×10^{-6} mol L⁻¹, the recoveries are also increased. Figure 10 shows that 0.35×10^{-6} mol L⁻¹ of APDC was necessary to obtain the maximum extraction efficiency. So, the amount of chelating agent (APDC) between 0.1-1 μ mol L⁻¹ was investigated and 0.35 μ mol L⁻¹ was found the best amount for Li and Mn extraction.

3.2.5. Optimization of time, reusability and absorption capacity

The dispersion of APDC/IL/GONPs in human blood, serum, urine or standard solution had a critical role for extraction Li(I) and Mn(II). The time extraction depended on chemical adsorption between the sulfur group with metals at pH 5-7. By the USA-DIL- μ -SPE procedure, the shaking time was examined between 1- 10 min. It has occurred that the shaking of 5.0 min was the favourite time for ions extraction in samples. In this study, the time of

shaking and centrifuging process were investigated and 5 min was found suitable for the shaking and 3 min for centrifuging process (3500 rpm). After sonication for 5 min, the APDC/IL/GONPs was trapped at the end of the conical tube and then the upper liquid phase was put out by auto-sampler. The reusability of APDC/IL/GONPs was obtained with many cycles extraction/back-extraction process. The results showed the adsorbent can be used for 12 cycles. The absorption capacities for cadmium depended on the characterization of APDC/IL/GONPs and surface area. The absorption capacities of APDC/IL/GONPs for Li and Mn was achieved at 148.5 mg g⁻¹, 122.3 mg g⁻¹, respectively.

3.2.6. Interference cations and anions

The effect of interference of ions on Li and Mn extraction in human biological samples were studied by the USA-DIL- μ -SPE procedure. The concentrations of ions were added to the standard solution and human samples with lithium (0.1 - 0.4 mg L⁻¹) and manganese (0.1 – 1.5 μ g L⁻¹) at optimized conditions. The results showed the interference of ions couldn't decrease the efficient extraction of Li and Mn ions at pH=6. (Table 1).

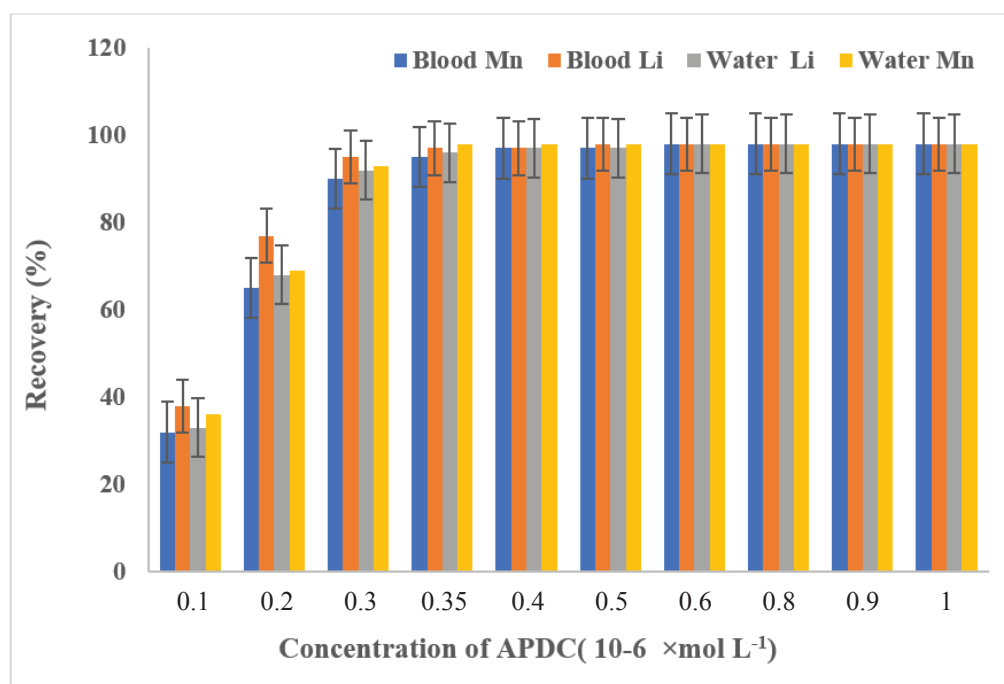


Fig.10. The effect of APDC concentration on Li /Mn extraction by the USA-DIL- μ -SPE procedure

Table 1. Interference cations and anions for Li and Mn extraction based on APDC/IL/GONPs by the USA-DIL- μ -SPE procedure

Interfering Ions(A)	Mean ratio ($C_A/C_{Li(0)}$)	Mean ratio ($C_A/C_{Mn(II)}$)	Recovery (%)	Recovery (%)
	Li	Mn	Li	Mn
Ni ²⁺ , Co ²⁺ , Se ²⁻	700	850	98.3	97.9
Cr ³⁺ , Al ³⁺ , Ag ⁺	600	700	97.1	97.3
I ⁻ , Br ⁻ , F ⁻ , Cl ⁻	1000	1100	97.8	98.4
Na ⁺ , K ⁺ , Ca ²⁺ , Mg ²⁺	1200	1300	98.8	99.1
CO ₃ ²⁻ , PO ₄ ³⁻ , NO ₃ ⁻	800	900	96.6	97.0
Zn ²⁺ , Cu ²⁺	500	750	97.5	98.5
Pb ²⁺ , Mo ²⁺ , Fe ²⁺	850	650	98.2	97.3
Hg ²⁺	100	80	96.2	98.5

3.2.7. Method validation

The concentration of Li and Mn in human blood and standard samples was determined by the USA-DIL- μ -SPE procedure. The results were obtained based on the average of three analyses in blood samples. The rate of recovery showed that the proposed method has good accuracy and precision in the blood matrix. The recovery of spiked blood samples and the standard solution was more than 95%. This method was satisfactory for the analysis of analytes in the human blood samples. Lithium and manganese concentrations were studied in

MS patients (40, subject) and healthy people (40, control) by the USA-DIL- μ -SPE procedure. Mean lithium and manganese concentrations in control groups were significantly lower than MS patients. In addition, for the validation of the method, standard reference materials (SRM) for Li and Mn were examined by the adsorbent. The results of blood samples in standard reference samples (SRM) was satisfactorily confirmed the accurate concentration of Li and Mn ions. The following table shows the validation of the USA-DIL- μ -SPE procedure based on APDC/IL/GONPs by spiking

Table 2. Validation of Mn determination in serum, blood and urine of MS patients by spiking samples with the standard solution by the USA-DIL- μ -SPE procedure coupled to ET-AAS

Sample	Added ($\mu\text{g L}^{-1}$) Mn	^a Found ($\mu\text{g L}^{-1}$) Mn	(%) Recovery
Blood	---	0.052 \pm 1.244	---
	0.5	0.117 \pm 1.729	97.0
	1.0	0.135 \pm 2.251	100.7
Serum	---	0.063 \pm 1.036	---
	0.5	0.072 \pm 1.531	99.0
	1.0	0.203 \pm 1.984	94.8
Urine	---	0.033 \pm 0.784	---
	0.5	0.065 \pm 1.293	101.8
	1.0	0.084 \pm 1.781	99.7

^aMean of three determinations of samples \pm confidence interval (P = 0.95, n = 8)

Table 3. Validation of Li determination in serum, blood and urine of MS patients by spiking samples with the standard solution by the USA-DIL- μ -SPE procedure coupled to F-AAS

Sample	Added (mg L ⁻¹) Li	^a Found (mg L ⁻¹) Li	(%) Recovery
Blood	---	0.07 ± 1.56	---
	1.0	0.12 ± 2.61	105.0
	1.5	0.14 ± 3.02	97.3
Serum	---	0.12 ± 2.16	---
	1.0	0.15 ± 3.11	95.0
	1.5	0.18 ± 3.63	98.0
Urine	---	0.033 ± 1.88	---
	1.0	0.065 ± 2.92	104.0
	1.5	0.084 ± 3.33	96.6

^aMean of three determinations of samples ± confidence interval (P = 0.95, n = 8)

real samples and standard reference materials. ICP-MS was used to prepare standard reference samples (SRM) for validation of methodology. In this study, the method was validated by spiking real samples with a standard Li and Mn solution in blood, serum and urine samples (Table 2 and 3). Also, the Li and Mn were validated by ICP-MS. Validation of Mn and Li extraction in human samples was obtained based on APDC/II/GONPs and standard reference materials (ICP-MS analysis) by the USA-DIL- μ -SPE procedure (Table 4 and 5). The results demonstrated the high

extraction and recovery for Li and Mn in human blood matrixes. As intra and inter-day analysis, the 40 MS patients were compared to healthy people by the USA-DIL- μ -SPE procedure (40 Men, 25-55 age, Iran) (Table 6). As Table 6, the concentration of lithium and manganese ions in the human body fluids for MS patients is significantly higher than the concentration of healthy people.

3.2.8. Discussion

The analysis of biological fluids is one of the most appropriate forms of evaluating environmental

Table 4. Validation methodology for Mn determination in human samples based on APDC/II/GONPs and standard reference materials (ICP-MS analysis) by the USA-DIL- μ -SPE procedure

Samples ^b	Added μ g L ⁻¹	Certified ^b μ g L ⁻¹	Found ^a μ g L ⁻¹	(%) Recovery
Serum	-----	0.02 ± 1.23	0.06 ± 1.21	98.4
	1.0	-----	0.12 ± 2.18	97.0
Blood	-----	0.01 ± 0.79	0.04 ± 0.81	102.5
	0.5	-----	0.05 ± 1.29	96.0
Urine	-----	0.02 ± 1.01	0.06 ± 0.98	97.1
	1.0	-----	0.09 ± 1.99	101.0

^aMean of three determinations of samples ± confidence interval (P = 0.95, n = 8)

^bICP-MS analyzer for blood, serum and urine as CRM (μ g L⁻¹)

Table 5. Validation methodology for Li determination in human samples based on APDC/II/ GONPs and standard reference materials (ICP-MS analysis) by the USA-DIL- μ -SPE procedure

Samples ^b	Added mg L ⁻¹	Certified mg L ⁻¹	Found ^a mg L ⁻¹	(%) Recovery
Serum	-----	0.05 ± 3.23	0.15 ± 3.14	97.2
	2.0	-----	0.24 ± 5.09	97.5
Blood	-----	0.02 ± 2.88	0.13 ± 2.86	99.3
	2.5	-----	0.24 ± 5.38	100.8
Urine	-----	0.01 ± 1.98	0.11 ± 2.02	102.1
	2.0	-----	0.09 ± 3.99	98.5

^aMean of three determinations of samples ± confidence interval (P = 0.95, n =8)

^bICP analyzer for blood, serum and urine as CRM (mgL⁻¹)

Table 6. The comparing of Li and Mn concentration in MS patients with healthy people by the USA-DIL- μ -SPE procedure

**Sample	*Patients MS		* Control		Patients MS			
	Li (mgL ⁻¹)	Mn (μ gL ⁻¹)	Li (mgL ⁻¹)	Mn (μ gL ⁻¹)	r Li	P value	r Mn	P value
Blood	6.19 ± 0.29	14.24 ± 0.65**	3.42 ± 0.15	3.12 ± 2.11**	0.202	<0.001	0.115	<0.001
Urine	4.35 ± 0.22	6.83 ± 0.31**	1.75 ± 0.07	2.42 ± 0.90	0.196	<0.001	0.076	<0.001
Serum	7.47 ± 0.33	1.34 ± 0.06	2.58 ± 0.12	0.63 ± 3.92	0.221	<0.001	0.109	<0.001

*Mean of three determinations of samples ± confidence interval (P = 0.95, n =40)

** Sample dilution (1:10) over a linear range of Mn

exposure to pollutants such as toxic metals. Metals are important constituents widely used in different industrial processes and can be present in biological fluids, namely urine, as a consequence of occupational exposure. Although atomic absorption spectrometric techniques, (flame or graphite furnace mode; FAAS and GFAAS) are a powerful analytical tool for the determination of trace metals. Determination of metals in urine, serum and blood samples is very difficult due to various factors, particularly low metal content and high salt content of the sample matrix. The use of a separation and preconcentration technique in the analytical process can solve these problems

and lead to easy determination of trace metals in urine, serum and blood samples. There are many methods for preconcentration/separation of trace heavy metals from human biological samples [24]. Komatsu et al reported determination of Li in whole blood by using colorimetric determination of lithium ions with a low limit of detection about 0.054 mM, and the coefficient of variance below 6.1%. A portion of whole blood has been placed on the end of the separation unit, plasma in the sample is automatically transported to the detection unit, which displays a diagnostic color [25]. This method has higher LOD and RSD% as compared to the USA-DIL- μ -SPE procedure. Also, a wide linear range

between 0.1-0.4 mg L⁻¹ was used based on APDC/IL/GONPs. Suherman et al reported electrochemical detection and quantification of lithium ions in authentic human saliva using LiMn₂O₄-modified electrodes. The sensing strategy is based on an initial galvanostatic delithiation of LMO followed by linear stripping voltammetry (LSV) to detect the re-insertion Li⁺ in the analyte. The process was investigated using powder X-ray diffraction (PXRD) and voltammetry. LSV measurements reveal a measurable lower limit of 50.0 μM in both LiClO₄ aqueous solutions and synthetic saliva samples [26]. Filippini et al showed that the determinants of serum manganese levels in an Italian population. They employed an inductively coupled plasmasector field mass spectrometry (ICP-SFMS) instrument for Mn determination in medium resolution mode. The LOD for Mn-peaks in SEC-ICP-DRC-MS was calculated as 3 σ-criterion and found between 28-35 ng L⁻¹ [27]. This method is expensive and sample preparation needs before analysis. On the other hand, as normal level Mn in serum or blood (μg L⁻¹), the USA-DIL-μ-SPE procedure has a sufficient rate. Zabłocka et al reported an applied method for evaluation Zn, Cu and Mn in serum /whole blood samples and their relation to redox status in lung cancer patients. In their study for whole blood preparation, 0.5 ml was performed twice by microwave –technique wet mineralization in a closed system using MLS 1200 Mega, with mixture 1:5 of H₂O₂(30%) and HNO₃(69–70%) and graphite furnace atomization was used for the determination of Mn. They reported analytical values of Zn, Mn and Cu were: 8.97 mg L⁻¹, 47.3 μg L⁻¹ and 2.47 mg L⁻¹, respectively. Mean accuracy (n = 6) was as follows: 98,3% (Zn), 105.9% (Mn) and 91.6% (Cu) which was comparable to the USA-DIL-μ-SPE procedure for Mn determination [28]. In this study, we used the USA-D-μ-SPE procedure based on APDC/IL/GONPs for micro-extraction and determination of lithium and manganese concentration in human biological samples. The surface charge of GONPs is negative so, the electrostatic attraction between negatively charged of adsorbent and positive charge of Li⁺ and Mn²⁺ ions have occurred at optimized pH=6. In addition,

quantitative extraction of more than 95% was observed in the optimized sample volume. It was also noticed that higher sample volumes, partially solubilized the ionic liquid phase, leading to non-reproducible results and increased the amount of GONPs. It was also observed that the extraction efficiency was remarkably affected by GONPs and IL amount, so they were examined within the range of 2 to 60 mg and 10 to 100 mg for GONPs and IL, respectively. Quantitative extraction was observed at 25 mg of GONPs for Li and Mn which was lower or similar amount as compared to other methods. The USA-DIL-μ-SPE method was applied to determine Li⁺ and Mn²⁺ for 1 mL and 10 ml in human biological samples, respectively. The spiked serum and blood were prepared to demonstrate the reliability of the method for extraction and determination of Mn and Li. At optimized condition, the LOD of the method was found 0.03 mg L⁻¹ for Li and 0.026 μg L⁻¹ for Mn²⁺ and working ranges was found 0.3-1.0 mg L⁻¹ for Li and 0.08-5 μg L⁻¹ for Mn. The mean of Mn²⁺ and Li⁺ concentration in blood, urine and serum of MS patients and healthy people were determined by the USA-DIL-μ-SPE procedure which was near to recently reported. The results showed that the concentration of Li⁺ and Mn²⁺ ions in the blood, urine and serum of MS patients were higher than healthy people, (6.19±0.29 μg L⁻¹ vs 3.42±0.15 μg L⁻¹, P<0.05 for Li in the blood and 6.83±0.31 mg L⁻¹ vs 2.42±0.90 mg L⁻¹, P<0.05 for Mn in urine). The adsorption capacity of APDC/IL/GONPs for Li⁺ and Mn²⁺ ions were found at 148.5 mg g⁻¹, 122.3 mg g⁻¹, respectively. This study showed that the application of APDC/IL/GONPs as the SPE procedure is a fast and low-cost separation route without nonabsorbent loss. Therefore, APDC/IL/GONPs is considered to be excellent and potential adsorbent for the extraction of Li⁺ and Mn²⁺ ions in human biological fluids.

4. Conclusions

A novel APDC/IL/GONPs was used for separation/extraction and determination of Li and Mn ions in human blood, serum and urine samples by the USA-DIL-μ-SPE procedure. The IL ([HMIM]

[PF₆]) property was helped to collect the GONPs phase from the liquid phase in the bottom of the conical tube. By the proposed procedure, a fast and simple, efficient extraction and perfect separation were achieved at pH 5-7 (RSD ≤ 5%). The APDC ligand coated on nanoparticles of GONPs enhanced the Li and Mn extraction in blood samples. By the USA-DIL-μ-SPE procedure many advantages such as good reusability, perfect separation, low cost, and high recovery (more than 95%) were achieved as compared to ICP-MS and other techniques. Therefore, the separation and determination of Li and Mn ions in human samples were achieved in optimized conditions. The results showed the detection limits (LOD), pre-concentration factor and the linear range of the method for Li and Mn were obtained (0.03 mg L⁻¹ and 0.025 μg L⁻¹), (9.72, 10.2) and (0.1-0.4 mg L⁻¹ and 0.08-1.5 mg L⁻¹), respectively. The adsorption capacity of graphene oxide for lithium and manganese was achieved at 148.5 mg g⁻¹ and 122.3 mg g⁻¹, respectively. Validation of the method was performed by spiking samples and standard reference materials (SRM) in the human blood, serum and urine.

5. Acknowledgements

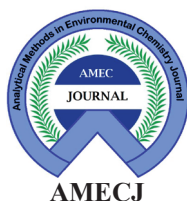
The analysis and sampling of Li /Mn blood samples based on the association declaration of Helsinki was approved by the Ethical Committee of the Azad University (Ethical Refecence: R.IAU.PS.REC.1398.272)

6. References

- [1] V.L. Feigin, A.A. Abajobir, K.H. Abate, F. Abd-Allah, A.M. Abdulle, S.F. Abera, Global regional and national burden of neurological disorders during 1990–2015: a systematic analysis for the Global Burden of disease study 2015, *Lancet Neurol.*, 16 (2017) 877-897. [https://doi.org/10.1016/S1474-4422\(17\)30299-5](https://doi.org/10.1016/S1474-4422(17)30299-5)
- [2] M.D. Napier, Heavy metals, organic solvents, and multiple sclerosis: an exploratory look at gene-environment interactions, *Arch. Environ. Occup. Health*, 71 (2016) 26-34. <https://doi.org/10.1080/19338244.2014.937381>
- [3] A. Karimi, K. Bahrapour, M.A.M. Moghaddam, G. Asadikaram, G. Ebrahimi, M. Torkzadeh-Mahani, Evaluation of lithium serum level in multiple sclerosis patients: A neuroprotective element, *Mult. Scler. Relat. Disord.*, 17 (2017) 244-48. <https://doi.org/10.1016/j.msard.2017.08.019>
- [4] D.F.D. Mota, B. D. Leversson, J. L. Goossens, Lithium in medicine: mechanisms of action, *Met. Ions Life Sci.*, 16 (2016) 557-584. https://doi.org/10.1007/978-3-319-21756-7_15
- [5] C. Garza-Lombó, Y. Posadas, L. Quintanar, M. E. Gonsebatt, R. Franco, Neurotoxicity linked to dysfunctional metal ion homeostasis and xenobiotic metal exposure: redox signaling and oxidative stress, *Antioxid. Redox Signal*, 28 (2018) 1669-1703. <https://doi.org/10.1089/ars.2017.7272>
- [6] P. Chen, S. Chakraborty, S. Mukhopadhyay, E. Lee, M. M.B. Paoliello, A. B. Bowman, M. Aschner, Manganese homeostasis in the nervous system, *J. Neurochem.*, 134 (2015) 601-610. <https://doi.org/10.1111/jnc.13170>
- [7] R. Nicholas, R. Waqar, Multiple sclerosis, *Am. Fam. Physician*, 87 (2013) 712-714. <https://pubmed.ncbi.nlm.nih.gov/23939450/>
- [8] A. Winckelmann, D. Morcillo, S. Richter, S. Recknagel, J. Riedel, J. Vogl, U. Panne, C. Abad, Determination of lithium in human serum by isotope dilution atomic absorption spectrometry, *ChemRxiv*, (2021). <https://doi.org/10.26434/chemrxiv.14130080.v1>
- [9] M. Aliasgharpour, H. Hagani, Evaluation of lithium determination in three analyzers: flame emission, FAAS and ion-selective electrode, *Am. J. Med.*, 1 (2009) 244-246. <https://dx.doi.org/10.4297%2Fnajms.2009.5244>
- [10] M. Aliomrani, M. A. Sahraian, H. Shir Khanloo, M. Sharifzadeh, M. R. Khoshayand, M. H. Ghahremani, Blood concentrations of cadmium and lead in multiple sclerosis patients from Iran, *Iran. J. Pharm. Sci.*, 15 (2016) 825-833. <https://www.ncbi.nlm.nih.gov/pubmed/28243279>

- [11] M. de Oliveira, T.M. Gianeti, F.C. da Rocha, P.N. Lisboa-Filho, M. Piacenti-Silva, A preliminary study of the concentration of metallic elements in the blood of patients with multiple sclerosis as measured by ICP-MS, *Sci. Rep.*, 10 (2020) 13112. <https://doi.org/10.1038/s41598-020-69979-9>
- [12] U. Kramer, M. Kress, H. Reinauer, M. Spannagl, P. Kaiser, Candidate reference measurement procedures for chloride, potassium, sodium, calcium, magnesium, and lithium by inductively coupled plasma (isotope dilution) sector field mass spectrometry (ICP-(ID) SFMS) in serum, *Clin. Lab.*, 59 (2013) 1017-1029. <https://doi.org/10.7754/clin.lab.2012.120902>
- [13] J. Lin, Y. Liu, Z. Hu, L. Yang, K. Chen, H. Chen, K. Zong, S. Gao, Accurate determination of lithium isotope ratios by MC-ICP-MS without strict matrix-matching by using a novel washing method, *J. Anal. At. Spectrom.*, 31 (2016) 390-397. <https://doi.org/10.1039/C5JA00231A>
- [14] A. Winkelmann, S. Nowak, S. Richter, S. Recknagel, J. Riedel, J. Vogl, U. Panne, C. Abad, High-Resolution atomic absorption spectrometry combined with machine learning data processing for isotope amount ratio analysis of lithium, *ChemRxiv*, (2021). <https://doi.org/10.26434/chemrxiv.13583024.v1>
- [15] E. Marguí, R. Dalipi, E. Sangiorgi, M. B. Štefan, K. Sladonja, V. Rogga, J. Jablan, Determination of essential elements (Mn, Fe, Cu and Zn) in herbal teas by TXRF, FAAS and ICP-OES, *Xray Spectrom.*, (2021)1-10. <https://doi.org/10.1002/xrs.3241>
- [16] N. Solovyev, M. Vinceti, P. Grill, J. Mandrioli, B. Michalke, Redox speciation of iron, manganese, and copper in cerebrospinal fluid by strong cation exchange chromatography–sector field inductively coupled plasma mass spectrometry, *Anal. Chim. Acta*, 973 (2017) 25-33. <https://doi.org/10.1016/j.aca.2017.03.040>
- [17] H. Shir Khanloo, M. Ghazaghi, M. M. Eskandari, Cloud point assisted dispersive ionic liquid-liquid microextraction for chromium speciation in human blood samples based on isopropyl 2-[(isopropoxycarbothioly) disulfanyl] ethane thioate, *Anal. Chem. Res.*, 10 (2016) 18-27. <https://doi.org/10.1016/j.ancr.2016.10.002>
- [18] D. Zou, Y. Qing, Y. Li, M. Liu, Y. Yang, Determination of manganese (VII), chromium (VI) and nickel (II) in medicinal herb samples by cloud point extraction and high-performance liquid chromatography, *J. Iran. Chem. Soc.*, 11 (2014) 415-422. <https://doi.org/10.1007/s13738-013-0313-6>
- [19] K. M. Diniz, C. R. T. Tarley, Speciation analysis of chromium in water samples through sequential combination of dispersive magnetic solid-phase extraction using mesoporous amino-functionalized $\text{Fe}_3\text{O}_4/\text{SiO}_2$ nanoparticles and cloud point extraction, *Microchem. J.*, 123 (2015) 185-195. <https://doi.org/10.1016/j.microc.2015.06.011>
- [20] M. Rezvani, A.A. Asgharinezhad, H. Ebrahimzadeh, N. Shekari, A polyaniline-magnetite nanocomposite as an anion exchange sorbent for solid-phase extraction of chromium (VI) ions, *Microchim. Acta*, 181 (2014) 1887-1895. <https://doi.org/10.1007/s00604-014-1262-1>
- [21] M. K. Abbasabadi, A. Rashidi, S. Khodabakhshi, Benzenesulfonic acid-grafted graphene as a new and green nano adsorbent in hydrogen sulfide removal, *J. Nat. Gas Sci. Eng.*, 28 (2016) 87-94. <https://doi.org/10.1016/j.jngse.2015.11.043>
- [22] J. Hummers, S. William, R. E. Offeman, Preparation of graphitic oxide, *J. Am. Chem. Soc.*, 80 (1958) 1339. <https://doi.org/10.1021/ja01539a017>
- [23] M. K. Abbasabadi, D. Azarifar, Magnetic Fe_3O_4 -supported sulfonic acid-functionalized graphene oxide ($\text{Fe}_3\text{O}_4@ \text{GO-naphthalene-SO}_3 \text{H}$): a novel and recyclable nanocatalyst for green one-pot synthesis of 5-oxo-dihydropyrano [3, 2-c] chromenes and 2-amino-3-cyano-1,

- 4, 5, 6-tetrahydropyrano [3, 2-c] quinolin-5-ones, *Res. Chem. Intermed.*, 45 (2019) 2095-2118. <https://doi.org/10.1007/s11164-018-03722-y>
- [24] R. M. Cespón-Romero, M. C. Yebra-Biurrun, Determination of trace metals in urine with an on-line ultrasound-assisted digestion system combined with a flow-injection preconcentration manifold coupled to flame atomic absorption spectrometry, *Anal. Chim. Acta*, 609 (2008) 184-191. <https://doi.org/10.1016/j.aca.2008.01.002>
- [25] T. Komatsu, M. Maeki, A. Ishida, H. Tani, M. Tokeshi, Based device for the facile colorimetric determination of lithium ions in human whole blood, *ACS Sens.*, 5 (2020) 1287-1294. <https://doi.org/10.1021/acssensors.9b02218>
- [26] A. L. Suherman, B. Rasche, B. Godlewska, P. Nicholas, S. Herlihy, N. Caiger, P. J. Cowen, R. G. Compton, Electrochemical detection and quantification of lithium ions in authentic human saliva using LiMn_2O_4 -modified electrodes, *ACS sens.*, 4 (2019) 2497-2506. <https://doi.org/10.1021/acssensors.9b01176>
- [27] T. Filippini, B. Michalke, P. Grill, C. Malagoli, M. Malavolti, L. Vescovi, S. Sieri, V. Krogh, A. Cherubini, G. Maffei, R. Lucchini, Determinants of serum manganese levels in an Italian population, *Mol. Med. Rep.*, 15 (2017) 3340-3349. <https://doi.org/10.3892/mmr.2017.6379>
- [28] K. Zabłocka-Słowińska, S. Płaczkowska, A. Prescha, K. Pawełczyk, I. Porębska, M. Kosacka, L. Pawlik-Sobecka, H. Grajeta, Serum and whole blood Zn, Cu and Mn profiles and their relation to redox status in lung cancer patients, *J. Trace Elem. Med. Biol.*, 45 (2018) 78-84. <https://doi.org/10.1016/j.jtemb.2017.09.024>



Removal of benzene vapor from the air based on novel tantalum metal-organic framework (Ta-MOF) adsorbent by gas flow solid-phase interaction before determination by gas chromatography

Mohammad Bagher Aghebat Bekheir^a, Mohammad Reza Rezaei Kahkha^b, Nasser Hasheminejad^a and Ali Faghihi-Zarandi^{a*}

^a Department of Occupational Health and Safety at Work, Kerman University of Medical Sciences, Kerman, Iran

^b Department of Environmental Health Engineering, Faculty of Health, Zabol University of Medical Sciences, Zabol, Iran

ARTICLE INFO:

Received 12 Aug 2021

Revised form 15 Oct 2021

Accepted 17 Nov 2021

Available online 29 Dec 2021

Keywords:

Adsorption,
Gas flow solid-phase interaction,
Tantalum metal-organic framework,
Gas chromatography

ABSTRACT

Benzene has a carcinogenic effect on the human body and adsorption from the air is the best way to control it. By this research, benzene vapor was removed from the air based on a tantalum metal-organic framework (Ta-MOF) by gas flow solid-phase interaction (GF-SPI). Benzene adsorption with Ta-MOF was studied in the static and dynamic systems at room temperature. The benzene concentration was analyzed by gas chromatography equipped with an FID detector (GC-FID). The factors affecting benzene removal efficiency like initial concentration of benzene, amount of adsorbent, exposure time, flow rate, and temperature were studied and optimized. The results showed us, the adsorption capacities range of Ta-MOF for benzene in the static and dynamic system were obtained between 90-160 mg g⁻¹ and 65-135 mg g⁻¹, respectively. Also, the high removal efficiency was achieved by more than 95% at 45°C, 67.5 mg L⁻¹ benzene concentration, 0.5 g of Ta-MOF, and the flow rate of 250 mL min⁻¹ for a dynamic system. By dynamic system, the benzene is generated in the chamber, stored in a bag, and then moved on the surface of Ta-MOF. The GF-SPI method was validated by GC-MS and spiking real samples.

1. Introduction

Volatile organic compounds (VOCs) contain a carbon structure with a high vapor pressure at room temperatures [1]. These compounds are known air pollutants released through industrial activities such as liquid fuels and cleaning supplies [2]. Benzene is a hazardous pollutant in the air that workers in various industries (oil and chemicals) exposure to it [3]. Benzene has been classified as a

definitive carcinogen in humans since 1979 based on sufficient evidence of leukemia. Benzene can replace by toluene or derivatives with less toxicity [4,5]. Benzene exists in fuels such as gasoline and is used in the production of styrene, dyes, inks and polymer products [6, 7]. Benzene enters into the air through different ways such as gasoline leakage, pipelines and petrochemical effluents[8]. Exposure to benzene can affect human health and cause cancer, CNS impairment, and kidney diseases [7, 9, 10]. The benzene is volatilized and distributed in air, soil, water and foods [11,12]. Exposure to BTEX products causes many problems in the

*Corresponding Author: [Ali Faghihi-Zarandi](mailto:Ali.Faghihi-Zarandi)

Email: Alifaghihi60@yahoo.com

<https://doi.org/10.24200/amecj.v4.i04.155>

human body [13-15]. By increasing stringent environmental standards, the actual control for the removal of VOCs is the principal aim [16]. Methods developed to control and remove VOCs emission on industrial plants including, condensation, adsorption, catalytic oxidation, and biodegradation methods. Whereas adsorption onto sorbents such as activated carbon, zeolites, and cotton fibres has been the reliable option so far [17,18]. Adsorption is one of the most efficient ways to control the emission of VOCs [19]. Some common adsorbents for the adsorption process are carbon quantum dots (CQDs), graphene (NG), resin, zeolite, and carbon nanotubes [20]. Metal-organic frameworks (MOFs) are relatively new compounds made of porous crystal materials and are being studied as adsorbents since 1998 [21]. These materials are regular polymers that are formed from different metals and bonds between metals created by organic compounds [22]. Organic-metal framework compounds use in clean energy, as the most important storage devices for gases such as hydrogen and methane, as well as high-capacity adsorbents to meet various separation needs [23]. The previous studies have shown that these adsorbents have excellent performance in absorbing benzene vapours. For instance, in 2008, Bright and colleagues studied benzene adsorption efficiency on various adsorbents made from MOFs. The adsorption occurs at the same conditions at 25°C and 440 ppm benzene concentration. Also, the adsorption capacities of the adsorbents varied from 2 to 176 mg g⁻¹. The MOF-199 sorbent had the highest absorption rate [24]. In 2019, Vikrant et al. Examined conventional adsorbents such as activated carbon for the adsorption of gaseous benzene compared to the new adsorbent of the metal-organic framework. The results showed the highest efficiency of MOF-199 was 94.8 mg g⁻¹, which was slightly higher than the other adsorbent, activated charcoal (93.5 mg g⁻¹). Also, the adsorption efficiency of the adsorbent MOF(UiO-66) is 27.1 mg g⁻¹, which is lower than the activated charcoal adsorption efficiency [25]. In 2011, Young and colleagues studied the adsorption of VOCs by

the metal-organic framework, MIL-101(Cr), influenced by the shape and size of the molecule and concluded that benzene adsorption capacity in MIL-101 was 1291±77 mg g⁻¹ [21]. Ahmaruzzaman and Xiang et al showed that activated carbon has desirable physical and chemical properties, which made it useful as an adsorbent and was used in the industry for decades. Sone et al were reported the CNTs can be used for BTEX removal from the air. They showed the carbon nanotubes are promising better absorbed than other carbon materials due to their unique properties. The CNT has been defined as cylindrical porous with walls made of crystalline graphite layers. Many technologies, such as bio-filter system [26], surface interaction [27], separation [28], adsorption [29, 30], and nanocatalyst [31], were used for VOCs removal. In addition, the various adsorbents such as activated carbon based on cellulose acetate [32], carbon nanotube (MWCNTs) [33], Zeolite [34], the graphene-modified by IL [35] were reported for removal benzene and BTX from the air.

In this study, benzene vapour was removed from the air based on a tantalum metal-organic framework (Ta-MOF) by the gas flow solid-phase interaction (GF-SPI). Benzene adsorption based on Ta-MOF was evaluated in the static and dynamic systems. The benzene concentration was analyzed by the GC-FID. The main parameters such as temperature, flow rate, the adsorbent mass and benzene concentration were optimized.

2. Material and Methods

2.1. Instrumental and reagents

All of the chemical compounds such as benzene anhydrous (99.8%, CAS N.: 71-43-2), tantalum chloride (CAS N: 7721-01-9 TaCl₅), benzene tetracarboxylic acid (CAS N.: 89-05-4), the cetyltrimethylammonium-Bromide (CAS N.: 57-09-0), and propane had high purity and were purchased from the Merck/Sigma company (Germany). Five calibration solutions of benzene were prepared. The approximate concentrations of benzene were prepared from 0.1, 0.5, 1.0, 1.5, and 2.0% (v/v). The other chemicals

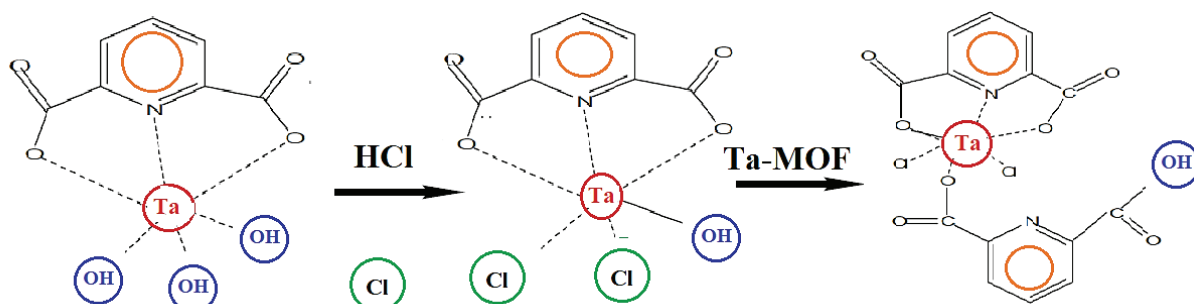


Fig.1. Preparation steps for synthesis of the tantalum metal-organic framework

based on GC grade and 99% purity were purchased from Merck (Germany). The characterization of the synthesized MOF was carried out via SEM-Philips XL 30, UK, and the X-ray diffraction equipment (XRD) Rigaku XDS 2000. The Agilent 7890A GC based on three detectors was used for benzene determination. The FID detector chosen was selected for benzene analysis in air. For injecting, slide the plunger carrier down and tighten the plunger thumb screw. Due to sampling valves, we introduce a sample of fixed size into the carrier gas stream. Valves are most frequently used to sample air or liquids. Gas sampling bags with valve and septum port (Tedlar) and air sampling apparatus (Bucket brigade) were prepared. The split/splitless injector, FID, and a column coated (50 m \times 0.2 mm id.) was used by GC. The injector temperature was adjusted to 200-210°C and the detector temperature at 240-250°C. The GC oven temperature was tuned at 220°C. Hydrogen as the carrier gas was used at a flow rate of 1.0 mL min⁻¹ with a split ratio of 1:100. Vials with PTFE air-tight cap (parker) were used as a batch/static system.

2.2. Preparation of the tantalum metal-organic framework

In this study, the MOF adsorbent was prepared by Rezaie and colleagues' research [36]. A solution of tantalum chloride (0.027 g) and benzene tetracarboxylic acid (0.011 g) was prepared in 17 mL double distilled water (DDW). The solution prepared from the reaction above and then added to the mixture of 0.77 g cetyltrimethylammonium-Bromide and 8 mL propane in a 50 mL Pyrex tube.

This new compound is then put in a microwave bath of 45°C and microwave bath with a power of 220 watts for 30 minutes. After 45 minutes of centrifuging, the MOF white crystals were formed, and then the product was left to dry in an argon atmosphere (Fig.1).

2.3. Benzene preparation in a dynamic system

First, the air was purified with an electro air cleaner (EA-HEPA600M) based on HEPA and activated carbon which was removed particles 200-300 nm (99.97%) and VOCs from the air, respectively. Then, the pure air passed through the chamber and entered to PVC bag (5 Li) by an SKC pump. The amount of H₂O (vapor) was controlled by adjusting the amount of water injection. All of the gas lines and bags were covered with heating jackets at 50-60 °C to prevent H₂O (vapor) and benzene from condensing (Fig.2).

2.4. Static and dynamic adsorption procedure

For the static experiment, 10 mL of different concentrations of benzene were drawn with a syringe and injected into the vials that were air-tightened with a PTFE lid and contained the Ta-MOF adsorbent. After a specific time, 100-500 microliter air from the vial was extracted and injected into the GC-FID analyzer for determining benzene. The effect of four exposures, times (5, 10, 15, and 20 minutes), the amount of Ta-MOF adsorbent in four amounts (0.5, 1, 1.5, and 2 mg), four different concentration levels (30, 50, 70, and 100 mg L⁻¹ of benzene) and, two temperatures of 25 and 45°C based on Ta-MOF adsorbent were studied (Fig.3).

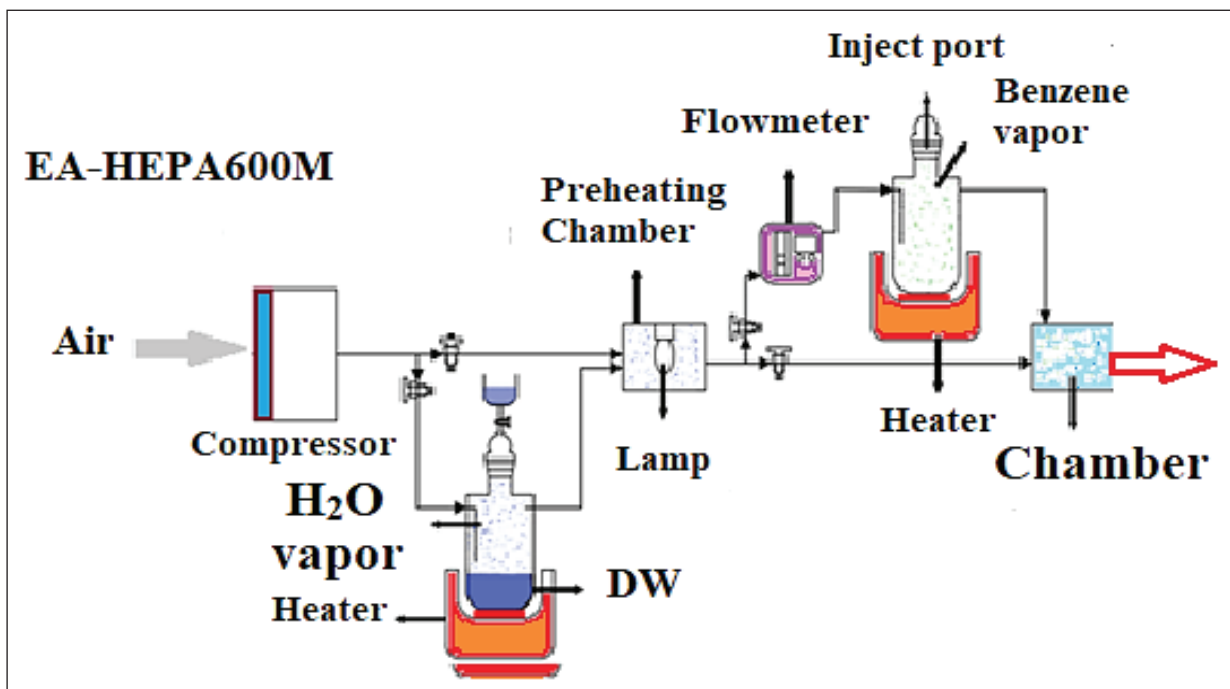


Fig.2. The generation of benzene vapor in pure air by chamber

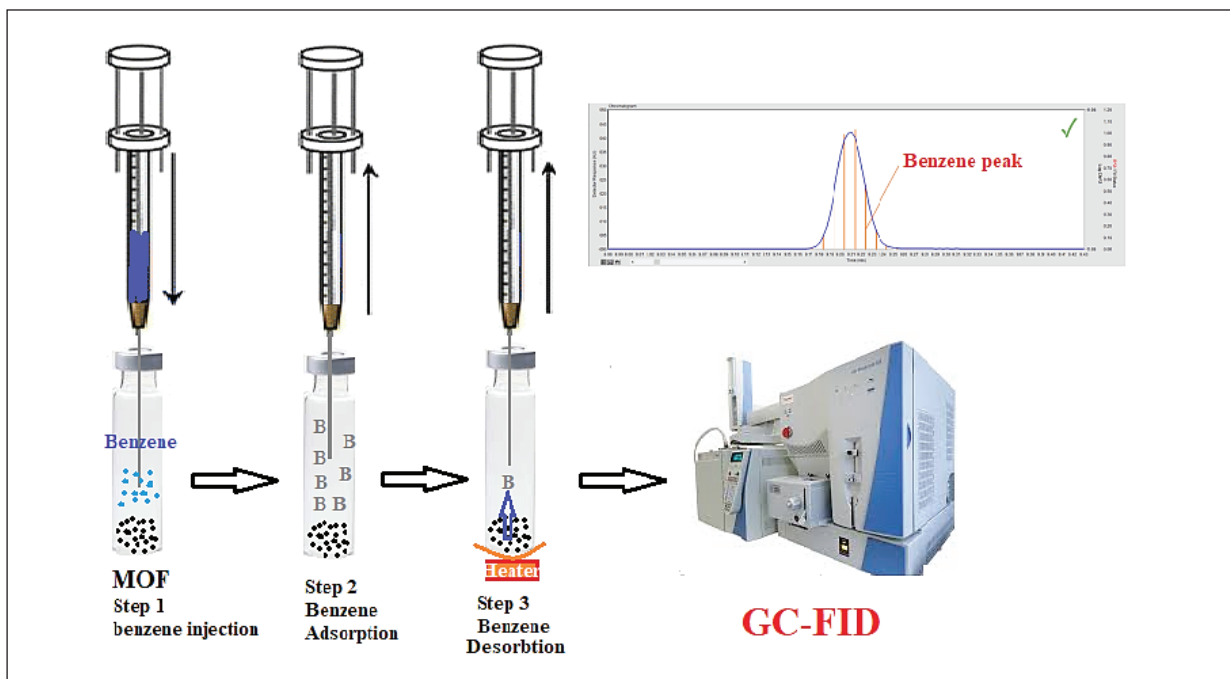


Fig.3. Static procedure for benzene removal from air by the Ta-MOF adsorbent

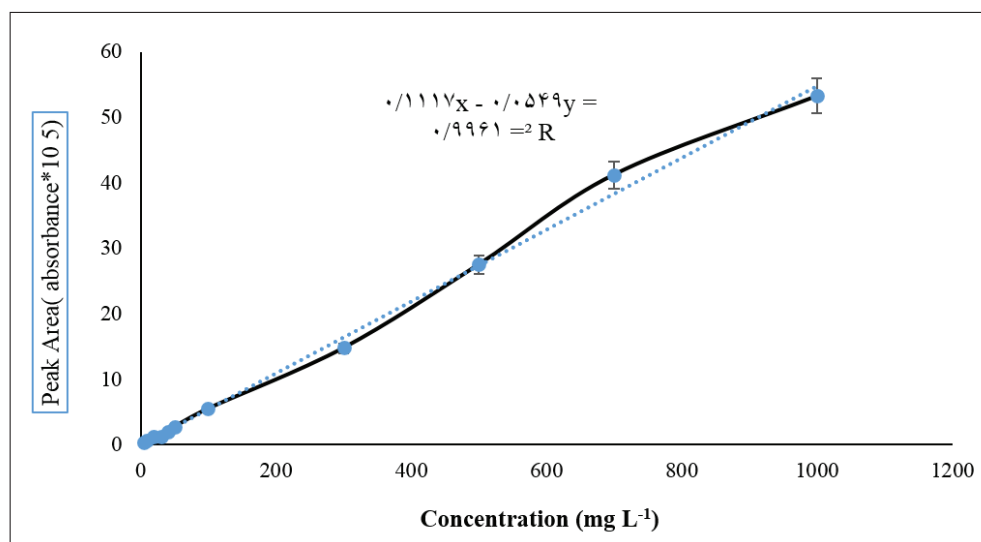


Fig.4. The calibration curve of benzene based on Ta-MOF adsorbent by GC-FID

The adsorption efficiency for static adsorption was obtained from the following equation:

$$Q = \frac{(C_0 - C_e) \times V}{m}$$

In the equation, Q is adsorption efficiency in (mg g^{-1}), C_0 is benzene's primary concentration in (mg L^{-1}), C_e is benzene's equilibrium concentration in the vial in (mg L^{-1}), m is the amount of adsorbent in (g), and V is the vial's volume in (L).

To draw the calibration curve from different standard concentrations of benzene in the ranges between 10 - 1000 mg L^{-1} were prepared in Tedlar sampling bags. Then, 100-500 microliters of the air vial containing benzene were prepared by a micro GC syringe. At last, the calibration curve was plotted by considering standard solutions and adsorption peak areas by GC-FID (Fig.4).

By dynamic procedure, 20 mg of Ta-MOF sorbent tubes connected to a sampling pump (SKC, UK). The flow rate was adjusted to 50-400 mL min^{-1} . The benzene vapour was mixed with pure air in the chamber, the different value of benzene in the air was passed through the Ta-MOF sorbent. After adsorption of benzene on Ta-MOF, the adsorbent was heated by thermal accessory at 80-100 $^{\circ}\text{C}$ in the presence of Ar gas and then, the benzene was

desorbed from Ta-MOF and flowed/stored in a polyethylene bag. Finally, the 100 -500 microliters of air were aspirated with Hamilton syringes and injected into an injector of GC-FID. Based on the dynamic procedure, Ta-MOF had efficient extraction and recovery for the removal of benzene from the air. The results showed that the absorption capacity of the static system was higher than the dynamic system at a flow rate of 250 ml min^{-1} .

3. Results and Discussion

3.1. SEM, TEM and XRD analysis

The morphology and size distribution of Ta-MOF nanoparticles were studied by a scanning electron microscope (SEM) and transmission electron microscopy (TEM). In this study, characterization of tantalum MOF adsorbent was carried out by SEM, TEM and XRD devices. SEM's microscopic images of Ta-MOF showed that the average size of particles in tantalum MOF adsorbent is 48 nanometers (Fig.5a). TEM of Ta-MOF showed a nanometric size of about 30 nm. The Ta-MOF sample has homogenous morphology with similar particle size (Fig.5b). Also, XRD images showed that tantalum MOF adsorbent has a cubic crystal structure (Fig.6). the X-ray diffraction pattern of porous Ta-MOF that prepared by the ultrasonic method. A comparison of Ta-MOF diffraction with the other MOF revealed a triclinic crystalline structure of Ta-

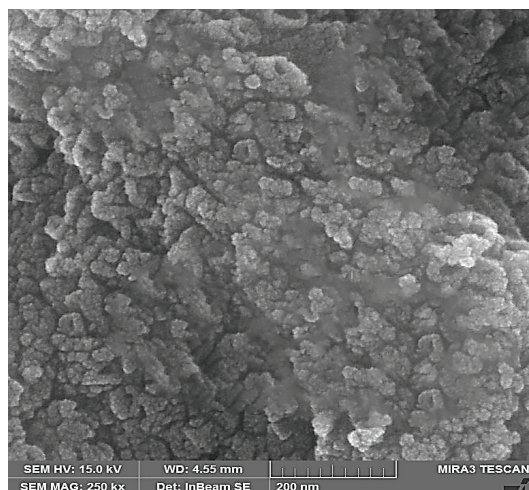


Fig. 5a. SEM images of tantalum Ta-MOF

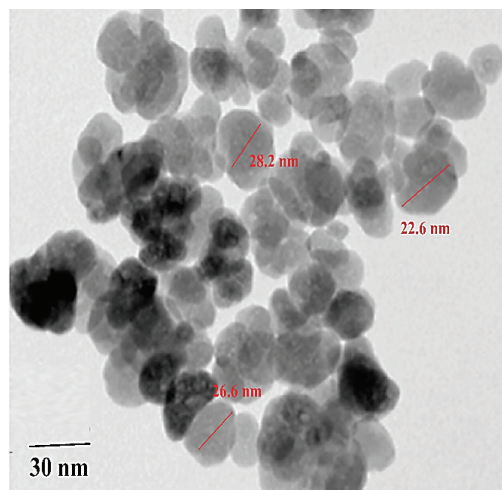


Fig. 5b. TEM images of tantalum Ta-MOF

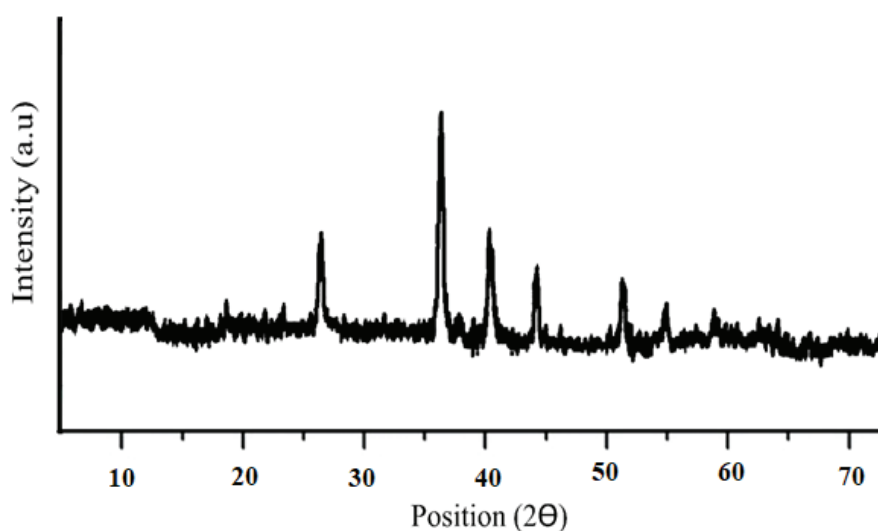


Fig. 6. XRD images of the tantalum MOF adsorbent

MOF. As TEM images any agglomeration wasn't seen in the structure of Ta-MOF.

3.2. The effect of benzene concentration on adsorption efficiency

The effect of benzene's primary concentration varying from 10 to 100 mg L⁻¹ on tantalum MOF adsorbent was studied. The results showed tantalum adsorbent became saturated at a concentration of 70 mg L⁻¹ (Fig. 7).

3.3. The Effect of exposure time on adsorbent efficiency

The effect of different times from 5 to 20 minutes

for benzene removal based on tantalum MOF in different concentrations of benzene between 10-100 mg L⁻¹ was studied. In this study, it was observed that increasing the exposure time has a positive effect on the recovery and adsorption capacity of Ta-MOF adsorbent. The results showed, the adsorption rate increases up to 10 minutes and then remains almost constant (Fig.8).

3.4. The effect of the amount of Ta-MOF on adsorption efficiency

The effect of the amount of the adsorbent (Ta-MOF) in the range of 0.1 to 2 mg for benzene removal include the benzene concentration (10 - 100 mg L⁻¹)

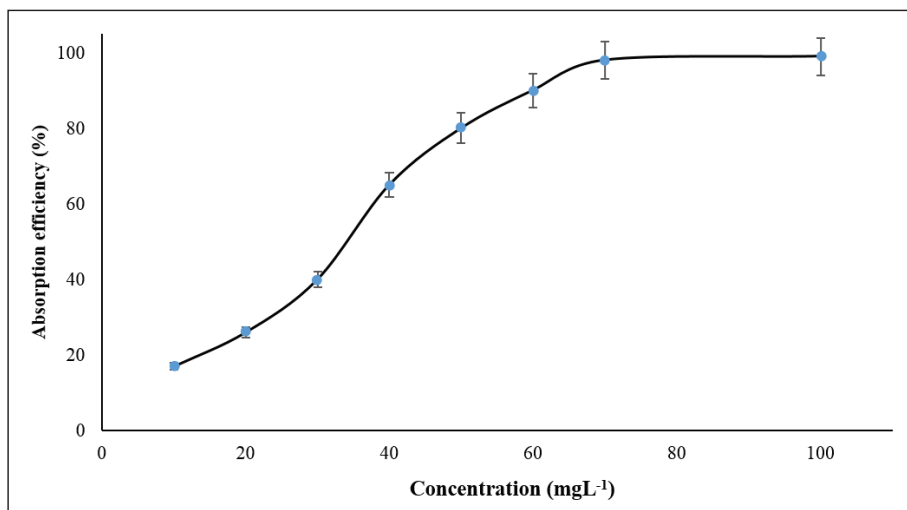


Fig.7. The effect of benzene concentration on Ta-MOF adsorption efficiency

was studied in optimized conditions. The results showed the maximum adsorption efficiency for benzene was achieved for 0.5 mg of Ta-MOF by 70 mg L⁻¹. Due to Figure 9, for an extra amount of adsorbent, the adsorption capacity increased and then constant (Fig. 9).

3.5. The effect of temperature on adsorption efficiency of Ta-MOF

For efficient removal of benzene from the air, the effect of temperature on adsorption/desorption of Ta-MOF must be optimized. The results showed us, the optimized temperature for adsorption and desorption of benzene from sorbent was achieved

at 45 °C and 90 °C, respectively. The effect of temperature on benzene removal was studied in optimized conditions. For this purpose, the different concentrations of benzene in the range of 10 to 100 mg L⁻¹ of benzene at a temperature between 25 - 60°C were evaluated. The results showed us, the maximum absorption capacity and efficiency were obtained at the temperature of 45 °C. For evaluating, 100-500 microliters of air containing benzene in static and dynamic procedure injected into GC. As shown in Figure 10, by increasing temperature, the absorption capacity and efficiency decreased (Fig.10).

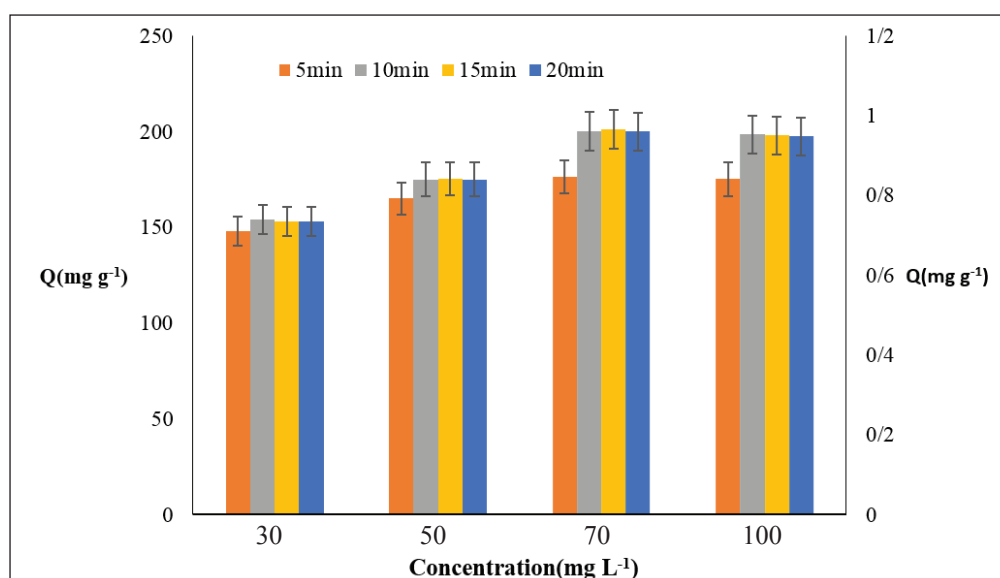


Fig. 8. The Effect of exposure time on adsorbent efficiency

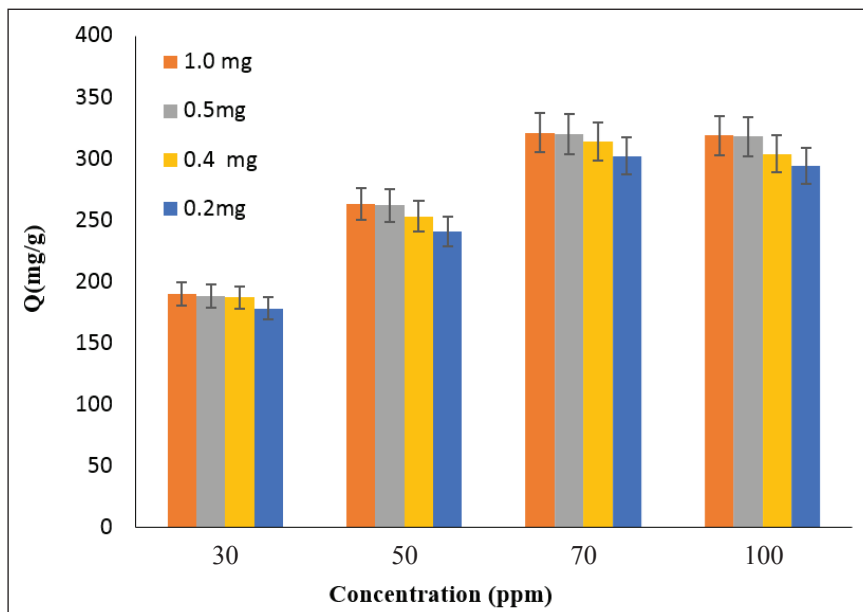


Fig. 9. The effect of the amount of Ta-MOF on adsorption capacity

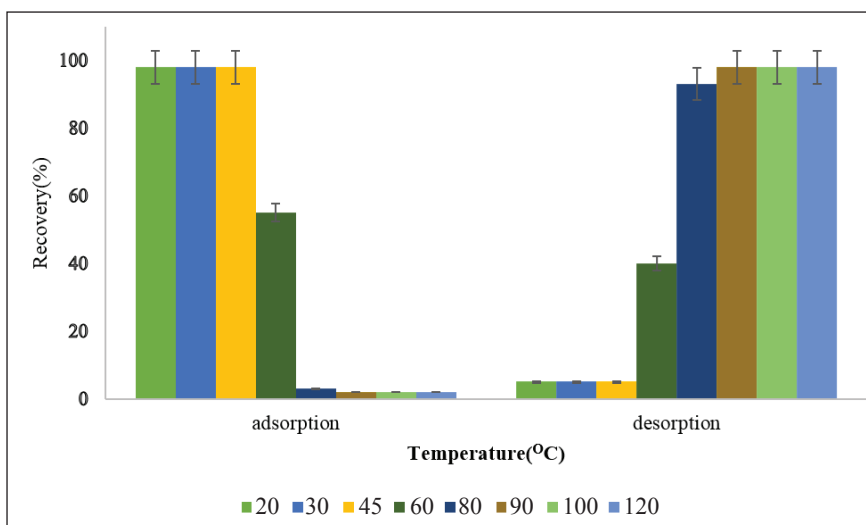
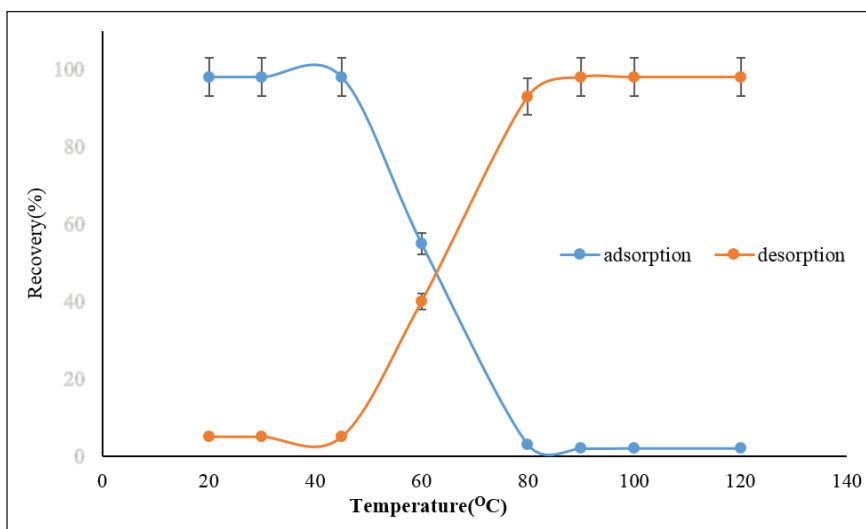


Fig.10. The effect of temperature on adsorption efficiency of Ta-MOF

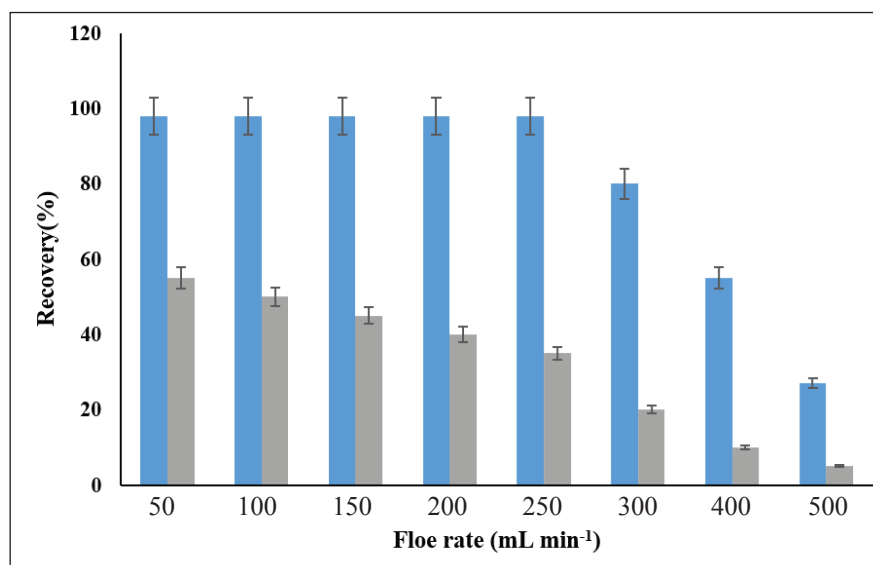


Fig.11. The effect of flow rate on adsorption efficiency of Ta-MOF (blue, 45 °C; grey, 60 °C)

3.6. Effect of flow rate

By procedure, the effect of different flow rates between 50 -500 mL min⁻¹ was studied by Ta-MOF adsorbent. The flow rate was measured by a digital rotameter. The removal efficiency and adsorption capacity of Ta-MOF were reduced in more than 300 mL min⁻¹ of flow rate. So, 250 mL min⁻¹ of flow rate was used as optimum flow rate for removal of benzene from the air. A higher

flow rate was significantly reduced the adsorption efficiency of benzene. Figure 11 shows the removal efficiency and adsorption capacity decreased by increasing the flow rate in optimized temperature (blue, 45 °C). Therefore, benzene cannot absorb at a higher flow rate by the sorbent. The results showed us the removal efficiency and the adsorption capacity was decreased at 60 °C (grey).

Table 1. Validation of GF-SPI method in a dynamic system based on Ta-MOF adsorbent by spiking benzene (ppm)

Air Samples	Added(ppm)	GF-SPI, GC-FID ppm	Recovery (%)
A	---	11.9 ± 0.4	---
	10	21.7 ± 1.1	98.1
B	---	18.5 ± 0.8	---
	20	38.2 ± 1.7	98.5
C	---	31.7 ± 1.4	---
	30	61.9 ± 2.9	100.6

^aMean of three determinations ± confidence interval (P = 0.95, n = 5)

3.7. Validation of methodology

The Ta-MOF was used for the removal of benzene vapour from the air. By the proposed method, a mixture of 10-100 ppm of benzene vapour in pure air (Ar gas) was passed through Ta-MOF sorbent by an SKC pump. Before adsorption, the standard of benzene in the air was validated by GC-MS in different concentrations. For validation, the spiked benzene concentration was done to demonstrate the reliability of the method by Ta-MOF (Table 1). At optimized conditions, at different times based on 250 mLmin⁻¹, the different concentrations of benzene in the air were generated and used for validation by spiking samples. The efficient recovery of spiked samples confirmed the capability of flow solid-phase interaction (GF-SPI) for the removal of benzene from the air.

3.8. Discussion

MOF adsorbent is one of the strongest adsorbents regarding the removal of volatile compounds from the air. In this study, the effect of tantalum organic metal framework adsorbent (Ta-MOF) for the removal of benzene vapour was investigated. The efficiency of different MOF adsorbents for benzene adsorption is shown in Table 2. Due to results, the tantalum MOF adsorbent has a higher adsorption efficiency as compared to the other adsorbents. In 2010, Lu and colleagues conducted a study regarding the removal of benzene, toluene, ethylbenzene, and para-xylene with carbon nanotubes oxidized by sodium hypochlorite and concluded that at first, with the increase of

exposure time, benzene adsorption efficiency also increased and then decreased [37]. As compared to the Ta-MOF, by increasing exposure time, the adsorption efficiency increased. Moreover, the maximum amount of adsorption occurred at 10 minutes and then the amount of adsorption remained constant. Also, in 2018, Hua Xie and colleagues carried out a study and concluded that the increase in temperature when using the MOF adsorbent, BUT-66 (Zr), lowered adsorption efficiency. In this study, it was found that the adsorbent at 25 and 80 °C had 2.54 mmol g⁻¹ and 1.65 mmol g⁻¹ of benzene adsorption, respectively [5], while in the present study at 25 and 45 °C, by increasing temperature, the amount of adsorption has decreased slightly. Also, the effect of temperature in the different adsorbents such as nano activated carbons and activated carbon has also been observed, which is confirmed by the study of Golbabai et al. to remove xylene vapor by these adsorbents. The results from Bright and colleagues research in 2008 regarding benzene adsorption efficiency using the adsorbents such as (MOF-5) (Zn₄O(CO₂)₆), (MOF-3)(C₈H₅NO₄-2), (MOF-177) (Zn₄O(btb)₂) and (MOF-199) (Cu₂(CO₂)₄), at benzene concentration levels of 440 ppm, showed that benzene adsorption efficiency for each 1gr adsorbent, was 2, 56, 1, and 176 milligrams of benzene, respectively [38]. However, in the present study, a trace amount of Ta-MOF can be absorbed by a high concentration of benzene (70 ppm) with a significant adsorption rate of 155.3 mg g⁻¹ which indicated the high adsorption capacity of the Ta-MOF adsorbent.

Table2. Comparing of adsorption capacities of Ta-MOF with other adsorbents

Adsorbate	Adsorbents	A _{sur} (m ² g ⁻¹)	Q _a	T	Refs.
Benzene	(Zn ₄ O(CO ₂) ₆) MOF-5	2205	2 mg g ⁻¹	25° c	[24]
	(C ₈ H ₅ NO ₄ -2)IRMO-3	1568	56 mg g ⁻¹	25° c	[24]
	(Zn ² O ₂ (CO ₂) ₂)MOF-74	632	96 mg g ⁻¹	25 °c	[24]
	(Zn ₄ O(btb) ₂)MOF-177	3875	1 mg g ⁻¹	25 °c	[25]
	(Cu ₂ (CO ₂) ₄)MOF-199	1264	176 mg g ⁻¹	25 °c	[24,25]
	IRMO-62	1814	109 mg g ⁻¹	25 °c	[24]
	MIL-101 (Cr)	3980	1291±77 mg g ⁻¹	25 °c	[17]
	Ta-MOF	1200	350 mg g ⁻¹	45 °c	This study

4. Conclusion

In the present study, a new Ta-MOF adsorbent was used for the removal of benzene from air and the absorption efficiency studied. For benzene analysis, 100-500 microliter air from the vial (static) or polyethylene bag (dynamic) was extracted and injected into the GC-FID analyzer. To evaluate the adsorbent capacity, the effect of four independent factors such as benzene concentration, the adsorbent amount, the exposure time, and temperature on the amount of benzene adsorption were investigated. The absorption capacities of static and dynamic procedures based on Ta-MOF were obtained 155.3 mg g⁻¹ and 124.6 mg g⁻¹, respectively based on 0.5 g of Ta-MOF and the flow rate of 250 mL min⁻¹. The results showed the Ta-MOF adsorbent had more adsorption capacity than other conventional adsorbents.

5. Acknowledgements

The authors wish to thank the Department of Occupational Health and Safety at Work, Kerman University of Medical Sciences, Kerman, Iran for supporting this work.

6. References

- [1] G. Zhang, Y. Liu, S. Zheng, Z. Hashisho, Adsorption of volatile organic compounds onto natural porous minerals, *J. Hazard. Mater.*, 364 (2019) 317-324. <https://doi.org/10.1016/j.jhazmat.2018.10.031>.
- [2] P. Liu, C. Long, Q. Li, H. Qian, A. Li, Q. Zhang, Adsorption of trichloroethylene and benzene vapors onto hypercrosslinked polymeric resin, *J. Hazard. Mater.*, 166 (2008) 46-51. <https://doi.org/10.1016/j.jhazmat.2008.10.124>.
- [3] D. Loomis, K.Z. Guyton, Y. Grosse, F. El Ghissassi, V. Bouvard, L. Benbrahim-Tallaa, N. Guha, N. Vilahur, H. Mattock, K. Straif, Carcinogenicity of benzene, *Lancet. Oncol.*, 18 (2017) 1574-1575. [https://doi.org/10.1016/s1470-2045\(17\)30832-x](https://doi.org/10.1016/s1470-2045(17)30832-x).
- [4] R. Althouse, J. Huff, L. Tomatis, J. Wilbourn, Chemicals and industrial processes associated with cancer in humans. IARC Monographs, IARC. Monogr. Eval. Carcinog. Risk. Chem. Hum. Suppl., 1-20 (1979) 1-71. <https://monographs.iarc.who.int/wp-content/uploads/2018/06/mono71.pdf>
- [5] L.H. Xie, X. M. Liu, T. He, J. R. Li, Metal-Organic frameworks for the capture of trace aromatic volatile organic compounds, *Chem.*, 4 (2018) 1911-1927. <https://doi.org/10.1016/j.chempr.2018.05.017>.
- [6] P. Gaurh, H. Pramanik, Production of benzene/toluene/ethyl benzene/xylene (BTEX) via multiphase catalytic pyrolysis of hazardous waste polyethylene using low-cost fly ash synthesized natural catalyst, *Waste. Manag.*, 77 (2018) 114-130. <https://doi.org/10.1016/j.wasman.2018.05.013>.
- [7] D.M. Chambers, C.M. Reese, L.G. Thornburg, E. Sanchez, J.P. Rafson, B.C. Blount, J.R.E. Ruhl, V.R. De Jesús, Distinguishing petroleum (Crude Oil and Fuel) from smoke exposure within populations based on the relative blood levels of benzene, toluene, ethylbenzene, and xylenes (BTEX), styrene and 2,5-Dimethylfuran by pattern recognition using artificial neural networks, *Environ. Sci. Technol.*, 52 (2018) 308-316. <https://doi.org/10.1021/acs.est.7b05128>.
- [8] E. Farsouni Eydi, A. Shariati, M.R. Khosravi-Nikou, Separation of BTEX compounds (benzene, toluene, ethylbenzene and xylenes) from aqueous solutions using adsorption process, *J. Dispers. Sci. Technol.*, 40 (2019) 453-463. <https://doi.org/10.1080/01932691.2018.1472007>.
- [9] A.L. Bolden, C.F. Kwiatkowski, T. Colborn, New look at BTEX: Are ambient levels a problem?, *Environ. Sci. Technol.*, 49 (2015) 5261-5276. <https://doi.org/10.1021/es505316f>.
- [10] M.I. Konggadinata, B. Chao, Q. Lian, R. Subramaniam, M. Zappi, D.D. Gang, Equilibrium, kinetic and thermodynamic studies for adsorption of BTEX onto ordered mesoporous carbon (OMC), *J. Hazard. Mater.*, 336 (2017) 249-259. <https://doi.org/10.1016/j.jhazmat.2017.04.073>.

- [11] R. Montero-Montoya, R. López-Vargas, O. Arellano-Aguilar, Volatile organic compounds in air: sources, distribution, exposure and associated illnesses in children, *Ann. Glob. Health*, 84 (2018) 225-238. <https://doi.org/10.29024/aogh.910>.
- [12] F.A. Kuranchie, P.N. Angnunavuri, F. Attiogbe, E.N. Nerquaye-Tetteh, Occupational exposure of benzene, toluene, ethylbenzene and xylene (BTEX) to pump attendants in Ghana: Implications for policy guidance, *Cogent. Environ. Sci.*, 5 (2019) 1603418. <https://doi.org/10.1080/23311843.2019.1603418>.
- [13] H. Huang, H. Huang, Q. Feng, G. Liu, Y. Zhan, M. Wu, H. Lu, Y. Shu, D.Y. Leung, Catalytic oxidation of benzene over Mn modified TiO₂/ZSM-5 under vacuum UV irradiation, *Appl. Catal. B*, 203 (2017) 870-878. <https://doi.org/10.1016/j.apcatb.2016.10.083>.
- [14] W. Yang, H. Zhou, C. Zong, Y. Li, W. Jin, Study on membrane performance in vapor permeation of VOC/N₂ mixtures via modified constant volume/variable pressure method, *Sep. Purif. Technol.*, 200 (2018) 273-283. <https://doi.org/10.1016/j.seppur.2018.02.044>.
- [15] V. Binas, V. Stefanopoulos, G. Kiriakidis, P. Papagiannakopoulos, Photocatalytic oxidation of gaseous benzene, toluene and xylene under UV and visible irradiation over Mn-doped TiO₂ nanoparticles, *J. Mater.*, 5 (2019) 56-65. <https://doi.org/10.1016/j.jmat.2018.12.003>.
- [16] Y. Wang, H. Tao, D. Yu, C. Chang, Performance assessment of ordered porous electrospun honeycomb fibers for the removal of atmospheric polar volatile organic compounds, *Nanomater. (Basel)*, 8 (2018) 350. <https://doi.org/10.3390/nano8050350>.
- [17] K. Yang, Q. Sun, F. Xue, D. Lin, Adsorption of volatile organic compounds by metal-organic frameworks MIL-101: influence of molecular size and shape, *J. Hazard. Mater.*, 195 (2011) 124-131. <https://doi.org/10.1016/j.jhazmat.2011.08.020>.
- [18] K. Vellingiri, P. Kumar, A. Deep, K.-H. Kim, Metal-organic frameworks for the adsorption of gaseous toluene under ambient temperature and pressure, *Chem. Eng. J.*, 307 (2017) 1116-1126. <https://doi.org/10.1016/j.cej.2016.09.012>.
- [19] W. Song, D. Tondeur, L. Luo, J. Li, VOC Adsorption in circulating gas fluidized bed, *Adsorption*, 11 (2005) 853-858. <https://doi.org/10.1007/s10450-005-6035-z>.
- [20] Z. Zhao, S. Wang, Y. Yang, X. Li, J. Li, Z. Li, Competitive adsorption and selectivity of benzene and water vapor on the microporous metal organic frameworks (HKUST-1), *Chem. Eng. J.*, 259 (2015) 79-89. <https://doi.org/10.1016/j.cej.2014.08.012>.
- [21] S. Gwardiak, B. Szczeńsiak, J. Choma, M. Jaroniec, Benzene adsorption on synthesized and commercial metal-organic frameworks, *J. Porous. Mater.*, 26 (2018) 775-783. <https://doi.org/10.1007/s10934-018-0678-0>.
- [22] L.Y. Filippova, V.N. Shubina, N.P. Kozlova, S.B. Putin, Adsorption properties of the MOF-5 metal-organic framework in relation to water and benzene, *Russ. J. Appl. Chem.*, 86 (2013) 1388-1391. <https://doi.org/10.1134/S1070427213090126>.
- [23] Zhou H-C, Long JR, Yaghi OM, Introduction to Metal-Organic Frameworks, *Chem. Rev.*, 112 (2012) 673-674. <https://doi.org/10.1021/cr300014x>.
- [24] D. Britt, D. Tranchemontagne, O.M. Yaghi, Metal-organic frameworks with high capacity and selectivity for harmful gases, *Proc. Natl. Acad. Sci.*, 105 (2008) 11623. <https://doi.org/10.1073/pnas.0804900105>.
- [25] K. Vikrant, C. J. Na, S.A. Younis, K. H. Kim, S. Kumar, Evidence for superiority of conventional adsorbents in the sorptive removal of gaseous benzene under real-world conditions: Test of activated carbon against novel metal-organic frameworks, *J. Clean. Prod.*, 235 (2019) 1090-1102. <https://doi.org/10.1073/pnas.0804900105>.

- [26] D. Wu, X. Quan, Y. Zhao, S. Chen, Removal of p-xylene from an air stream in a hybrid biofilter, *J. hazard. Mater.*, 136 (2006) 288-295. <https://doi.org/10.1016/j.jhazmat.2005.12.017>.
- [27] S. Pedram, H.R. Mortaheb, F. Arefi-Khonsa, Optimization of benzene removal by air gap membrane distillation using response surface methodology, *J. Water Supp. Res. Technol.*, 68 (2019) 231-242. <https://doi.org/10.2166/aqua.2019.067>.
- [28] Y. Yang, P. Bai, X. Guo, Separation of xylene isomers: a review of recent advances in materials, *Ind. Eng. Chem. Res.*, 56 (2017) 14725-14753. <https://doi.org/10.1021/acs.iecr.7b03127>.
- [29] Z. Vahdat Parast, H. Asilian, A. Jonidi Jafari, Adsorption of xylene from air by Natural Iranian zeolite, *Health. Scope*, 3 (2014) e17528. <https://dx.doi.org/10.17795/jhealthscope-17528>.
- [30] S.T. Lim, J.H. Kim, C.Y. Lee, S. Koo, D. W. Jerng, S. Wongwises, H.S. Ahn, Mesoporous graphene adsorbents for the removal of toluene and xylene at various concentrations and its reusability, *Sci. Rep.*, 9 (2019) 1-12. <https://doi.org/10.1038/s41598-019-47100-z>.
- [31] K.W. Shah, W. Li, A Review on catalytic nanomaterials for volatile organic compounds removal and their applications for healthy buildings, *Nanomater. (Basel)*, 9 (2019) 910. <https://doi.org/10.3390/nano9060910>.
- [32] K. Patil, S. Jeong, H. Lim, H. S. Byun, S. Han, Removal of volatile organic compounds from air using activated carbon impregnated cellulose acetate electro spunmats, *Environ. Eng. Res.*, 24 (2019) 600-607. <https://doi.org/10.4491/eer.2018.336>.
- [33] M. Bagheri Hossein Abadi, H. Shirkhanloo, J. Rakhshshah, Air pollution control: the evaluation of TerphApm@MWCNTs as a novel heterogeneous sorbent for benzene removal from air by solid phase gas extraction, *Arab. J. Chem.*, 13 (2020) 1741-1751. <https://doi.org/10.1016/j.arabjc.2018.01.011>.
- [34] S. KP Veerapandian, N. De Geyter, J. M. Giraudon, J.-F. Lamonier, R. Morent, the use of zeolites for VOCs abatement by combining non-thermal plasma, adsorption, and/or catalysis: a review, *Catalysts*, 9 (2019) 98. <https://doi.org/10.3390/catal9010098>.
- [35] H. Shirkhanloo, M. Osanloo, O. Qurban-dadras, Nobel method for toluene removal from air based on ionic liquid modified nano-graphene, *Int. J. Occup. Hyg.*, 6 (2014) 1-5. <https://ijoh.tums.ac.ir/index.php/ijoh/article/view/89>
- [36] M.R. Rezaei Kahkha, M. Kaykhaii, G. Sargazi, B. Rezaei Kahkha, Determination of nicotine in saliva, urine and wastewater samples using tantalum metal organic framework pipette tip micro-solid phase extraction, *Anal. Methods*, 11 (2019) 6168-6175. <https://doi.org/10.1039/C9AY01773A>.
- [37] F. Su, C. Lu, S. Hu, Adsorption of benzene, toluene, ethylbenzene and p-xylene by NaOCl-oxidized carbon nanotubes, *Colloids. Surf. A. Physicochem. Eng. Asp.*, 353 (2010) 83-91. <http://dx.doi.org/10.1016/j.colsurfa.2009.10.025>.
- [38] M. Jafarizaveh, H. Shirkhanloo, F. Golbabaee, A. Tabrizi, K. Azam, M. Ghasemkhani, Nobel method for xylene removal from air on nano activated carbon adsorbent compared to NIOSH approved carbon adsorbent, *J. Health Safe. Work*, 6 (2016) 23-30. https://jhs.w.tums.ac.ir/browse.php?a_id=5374&sid=1&slc_lang=en



Adsorption of nitrate from aqueous solution with ZSM-5/Fe nanosorbent based on optimizing of the isotherms conditions before determination by UV-Vis Spectrophotometry

Mostafa Hassani^a, Mohsen Zeeb^{a,*}, Amirhossein Monzavi^b, Zahra Khodadadi^a and Mohammad Reza Kalaei^c

^aDepartment of Applied Chemistry, Faculty of Science, Islamic Azad University, South Tehran Branch, Tehran, Iran

^bDepartment of Polymer and Textile Engineering, Islamic Azad University, South Tehran Branch, Tehran, Iran

^cDepartment of Polymer and Chemical Engineering, Islamic Azad University, South Tehran Branch, Tehran, Iran

ARTICLE INFO:

Received 28 Jul 2021

Revised form 7 Oct 2021

Accepted 10 Nov 2021

Available online 30 Dec 2021

Keywords:

Adsorption,
ZSM-5/Fe nanozeolite,
Freundlich,
Langmuir,
UV-Vis Spectrophotometry

ABSTRACT

The life-threatening nature of high nitrate concentrations in various water resources motivated the present study to investigate the nitrate adsorption by ZSM-5 nanozeolite and the feasibility of increasing nitrate removal efficiency using iron-doped ZSM-5 (ZSM-5/Fe) nanoadsorbent. The optimal adsorption conditions were determined first by modeling the central composite design (CCD) using Design Expert.7 software based on four influential factors of contact time, pH, adsorbent dosage and initial nitrate concentration. Then, the isotherms of nitrate adsorption under optimized conditions were investigated using the degree of fit of experimental data with Langmuir and Freundlich models for mathematical modelling of the nitrate adsorption process. Based on the test design results, the highest nitrate removal efficiency (%93.1) was determined with UV-Vis spectrophotometry at the contact time of 150 min, pH value of 3, the adsorbent dosage of 4 g L⁻¹ and initial concentration of 40 mg L⁻¹. Analysis of adsorption isotherms also confirmed the greater fit of the experimental data with the Freundlich equation, so that the correction factor of the Freundlich equation was greater than the Langmuir equation, due to the heterogeneous distribution of active sites for adsorption on the ZSM-5/Fe nanosorbent surface. Therefore, it can be concluded that ZSM-5/Fe is a high efficiency nanosorbent for nitrate removal from water resources.

1. Introduction

Nitrate is known to be one of the most serious threats to human health in the world, which enters the human body through the penetration into groundwater and surface water resources following the excessive use of chemical fertilizers and uncontrolled discharge without nitrification of municipal and industrial wastewater in the environment [1-3]. This ion is

relatively non-toxic in nature, but its reduction to nitrite by microorganisms can pose serious health risks to humans, including blue baby syndrome, also known as infant methemoglobinemia [4-7]. Accordingly, the EPA has recommended that the maximum permissible concentration of nitrate is 10 mg L⁻¹ in drinking water [8]. Hence, various methods have been previously employed to remove nitrate from aqueous solutions, such as adsorption, ion exchange, reverse osmosis, chemical and biological methods. In recent years, adsorption methods have attracted much attention

*Corresponding Author: [Mohsen Zeeb](mailto:mohsen.zeeb@iaut.ac.ir)

Email: zeeb.mohsen@gmail.com

<https://doi.org/10.24200/amecj.v4.i04.154>

in the removal of mineral ions, including fluoride, nitrate, bromate and perchlorate from water and wastewater. Conventional chemical adsorbents today include those based on carbon, clay, zeolite, chitosan, bilayer compounds (hydroxide/hydroxalite), agricultural and industrial wastes, and miscellaneous group [9-19]. Many researchers at present are focusing on zeolites as natural adsorbents of environmental pollutants through ion exchange or adsorption or both due to large specific surface area, unique channel structure, high-temperature hydrothermal stability and high modifiability to enhance adsorption efficiency [20-25]. Kamarehie et al. fabricated a natural nanosorbent using granular activated carbon from grape wood coated with iron nanoparticles to remove nitrate from aqueous solutions. The adsorption was then investigated by the Freundlich isotherm model. Their results showed that more than 99% of nitrate was removed from the solution with this nanosorbent [26]. Mazarji et al removed nitrate from the aqueous solution using modified granular activated carbon. They modified a commercial granular activated carbon with sodium hydroxide to increase nitrate removal efficiency, followed by examining parameters such as adsorbent dosage, solution pH, contact time and initial nitrate concentration and temperature in the nitrate adsorption process. They concluded that the use of two-step treatment could be a promising method in improving the efficiency of activated carbon to remove nitrate from water [27]. Hafeshjani et al. used sugarcane residues to remove nitrate from aqueous solutions, and investigated the physicochemical properties of the adsorbent such as morphology, element composition, ion exchange capacity and specific surface area. They measured parameters such as pH, adsorbent dosage, contact time, initial nitrate concentration and temperature using different adsorption kinetic models such as Freundlich, Langmuir and others. Their results indicated that the maximum nitrate removal efficiency was achieved at pH value of 4.64, contact time of 60 minutes, adsorbent dosage of 2 g L⁻¹ and the best models were Langmuir

isotherm model and Pseudo-second-order kinetic model [28]. Meftah et al modified natural nanozeolite with 3-aminopropyl triethoxysilane and investigated the optimal conditions for nitrate adsorption capacity of modified zeolite in aqueous solutions. Their results revealed that the best nitrate removal capacity (80.12 %) was obtained at the lowest pH value of 3 and nitrate concentration of 50 mg L⁻¹ and adsorbent dosage of 4 g L⁻¹ [29]. Alimohammadi et al optimized the nitrate removal efficiency using magnetic multi-walled carbon nanotubes by response surface methodology (RSM). They measured two parameters of pH and D/C ratio with quadratic models using RSM, and reported the maximum nitrate removal efficiency (%97.15) at pH = 4 and D/C = 40 mg per mg L⁻¹. It is worth mentioning that they used the Freundlich adsorption isotherm to interpret the adsorption dosage [30]. Azari et al. fabricated a zeolite modified with hydrochloric acid to remove nitrate from aqueous solutions, and investigated the effects of pH, strings speed, contact time, and optimum adsorbent dosage for this nanosorbent under isotherm equations. Their results revealed that the optimum conditions for pH, contact time and adsorbent dosage for maximum nitrate removal with this nanosorbent were 5, 180 min and 16 g L⁻¹, respectively, confirming higher removal efficiency compared to simple unmodified zeolite due to the presence of larger sites [31]. Sepehri et al. presented a natural zeolite-supported zero-valent iron nanoparticles (ze-Nzvi adsorbent) using the sodium borohydride reduction method with the aim of removing nitrate from aqueous solution. Then, they measured the parameters of contact time, adsorbent dosage, initial nitrate concentration, initial pH, the results of which showed that the nitrate removal efficiency was decreased with increasing the initial solution pH and the adsorbent dosage but elevated with increasing the initial nitrate concentration [32]. Fataei et al investigated the effects of iron and sand nanoparticles on nitrate removal efficiency on a laboratory scale. In this research, they tested the effect of pH, sand and iron particles parameters on nitrate removal efficiency.

The mixture of iron and sand particles elevated efficiency and specific area. The results showed that the efficiency of iron nanoparticles was 65% in the first 20 min and 45% in the next times when the pH of the reactions increased. Therefore, the results confirmed that the initial solution pH was important in the maximum nitrate removal efficiency [33]. Bhatnagar et al. introduced nanoalumina to remove nitrate from aqueous solution. In their study, they examined the parameters of contact time, pH, nitrate concentration with a pseudo-second-order kinetic model. The highest nitrate removal efficiency was achieved at a concentration of 4 mg g⁻¹, a temperature of 23-27°C and a pH value of 4.4. Langmuir isotherm model was performed to analyze the nitrate adsorption. The results of this study verified the nano-alumina as a useful and effective adsorbent for the nitrate removal from aqueous solutions [34].

Given that metals such as Al, Sn, Zn, Fe and Ni are effective agents for remediation of contaminated groundwater, hence the present study tested iron metal due to its availability, inexpensiveness, non-toxicity, high efficiency and rapid reaction in the decomposition of contaminants to functionalize ZSM-5 nanozeolite with the aim of determining the optimal conditions and effective factors in nitrate removal, including pH, contact time and adsorbent dosage using RSM as well as evaluating the adsorption isotherms.

2. Experimental

2.1. Material

The ZSM-5 nanocatalyst powder (from the Zeolites family) was purchased from Sigma Aldrich with a crystal size of 0.5 µm and a pore size of 5.5 Å⁰. Ferric chloride (FeCl₃), sodium hydroxide (NaOH), Potassium nitrate (KNO₃), Hydrochloric acid (HCl) and %98 sulfuric acid (H₂SO₄) were also obtained from Merck Germany.

2.2. Materials characterization

X-ray diffraction (XRD, STADI-P, the USA) and energy-dispersive X-ray spectroscopy (EDX, MIRA III SAMX, Czech Republic) was used to

investigate ferrous (Fe) metal in the nanocatalyst structure functionalized with these metal. Brunauer-Emmett-Teller (BET) surface area analysis (Belsorb apparatus, Japan) was used to determine the SSA of nanocatalyst particles. The concentration of nitrate was determined by spectrophotometer UV-Vis (Hach model Dr2800) was used.

2.3. Preparation of ZSM-5/Fe Nanozeolite

To Preparation the functionalized ZSM-5 nanocatalyst, first 2.5 g of ZSM-5 nanozeolite powder was placed in the furnace at a temperature of 500°C for 4 hours and calcined. Then, 0.5 g of ferric chloride (FeCl₃) powder was dissolved in distilled water twice for one hour, added to the calcined ZSM-5 nanozeolite powder and mixed for another 30 minutes, and filtered with a filter paper. The resulting powder was rinsed three times with distilled water and placed in an oven at a temperature of 80°C for 2 hours. Next, the powder was separated from the filter paper and re-calcined at a temperature of 500°C for 4 hours. The method of preparation above nanocatalyst is schematically illustrated in Fig.1.

2.4. Preparation of solutions

To prepare a standard concentrated potassium nitrate solution, 7 g of anhydrous KNO₃ was dried at 100°C for an hour. After cooling, 1.805 g of KNO₃ was dissolved in a volumetric flask and diluted to 250 mL, thus preparing a standard solution of 1000 mg L⁻¹ or 1.0 mg mL⁻¹. HCL and NaOH solutions were prepared to set the pH values. Then, nitrate solutions with concentrations of 20, 40, 60, 80, 100 and 120 mg per liter were prepared from the standard solution of potassium nitrate 1000 mg L⁻¹.

2.5. Procedure

In this research, the experimental design table was first provided using the effective variables of pH, contact time and stirring speed in the intervals defined to RSM and the central composite design (CCD) by Design Expert.7 software. Then, the value of each parameter was provided according to the experimental design table and finally the

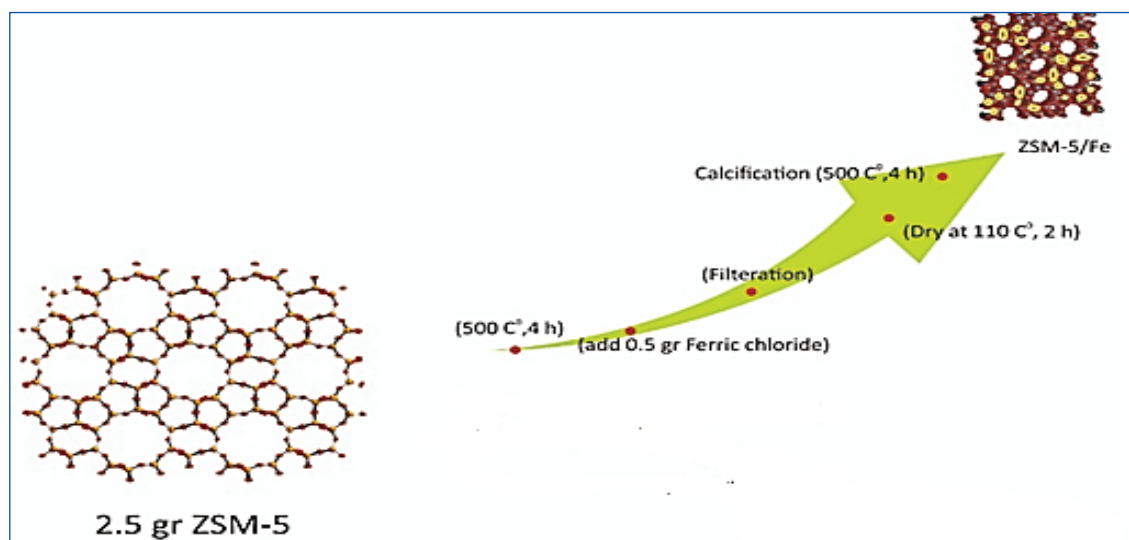


Fig.1. Schematic of ZSM-5/Fe nanosorbent fabrication method

absorbance values or nitrate concentrations were measured by UV-Vis spectrophotometry. The results were analyzed by experimental design software, and the optimal values of pH, contact time and stirring speed were determined. In the next step, the isotherms of nitrate adsorption under optimized conditions were investigated using the degree of fit of experimental data with Langmuir and Freundlich models for mathematical modeling of the nitrate adsorption process.

2.6. Langmuir adsorption model

The mathematical model of this isotherm is shown in Equation 1 and 2 .

$$q_e = q_{\max} \frac{bc}{1+bc_e} \quad (\text{Eq. 1})$$

$$1/q_e = 1/q_{\max} \frac{bc_e + 1}{q_{\max}} \quad (\text{Eq. 2})$$

Where, q_{\max} and b stand for experimental constants, q_e for the amount of substance adsorbed per unit mass of adsorbent (mg g^{-1}) and C_e for the equilibrium adsorbate concentration in solution (mg L^{-1}).

2.7. Freundlich adsorption model

Equation 3 shows the mathematical model of the Freundlich isotherm. Where, q_e and C_e are similar to the Langmuir isotherm, and n and K stand for Freundlich constants. The linear equation of the Freundlich isotherm is as equation 4.

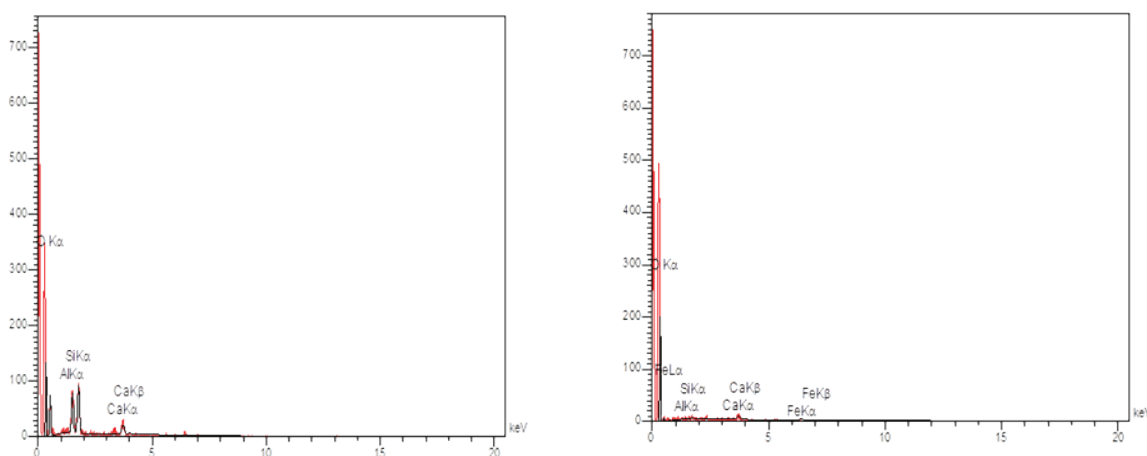


Fig. 2. Energy-dispersive X-ray spectroscopy (EDX) analysis of the ZSM-5 and ZSM-5/Fe

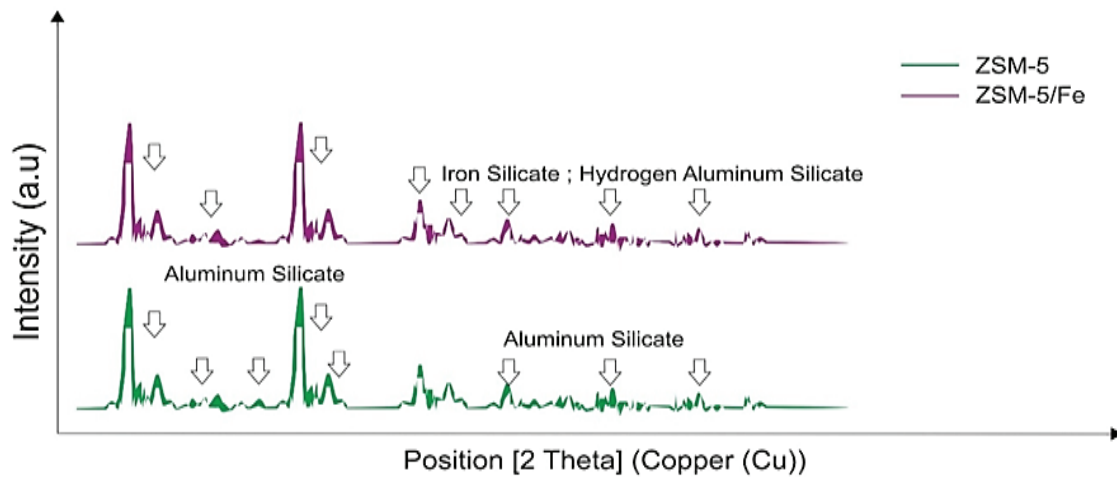


Fig. 3. Investigation of nickel doping by X-ray diffraction (XRD) analysis

$$q_e = K_f C_e^{1/n} \quad (\text{Eq. 3})$$

$$\log q_e = \log K + 1/n \log C_e \quad (\text{Eq. 4})$$

3. Results and Discussion

3.1. Investigation of electrode surface modification by EDX and XRD analysis

According to [Figure 2](#) the presence of iron particles in the nanosorbent structure is quite evident. The

XRD spectrum for the ZSM-5/Fe nanozeolite confirms the presence of iron particles doped with silicate particles ([Fig.3](#)).

3.2. BET characterization

By comparing the BET parameter ([Fig.4](#) and [Table 1](#)), in each of the four BET analysis curves of the nanozeolite, the highest SSA was related to the catalyst functionalized with Fe metal (ZSM-5/Fe, which was determined to be $408.41 \text{ m}^2 \text{ g}^{-1}$).

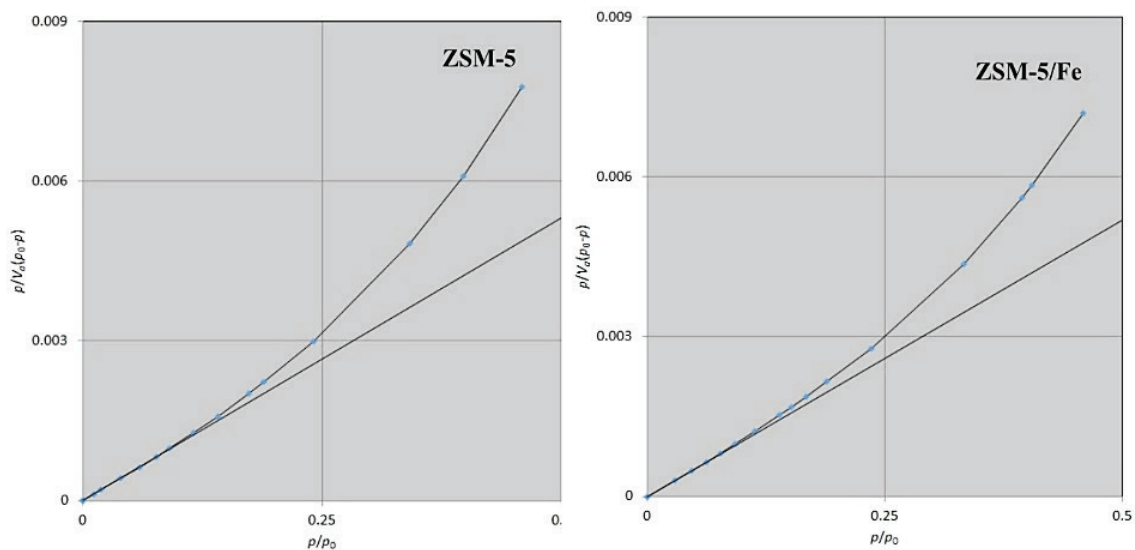


Fig.4. BET curves of prepared nanosorbent

Table 1. The specific surface area of prepared nanozeolite

Row	Nanocatalysts	BET	Unit
1	ZSM-5	374.66	m ² g ⁻¹
2	ZSM-5/Fe	408.41	m ² g ⁻¹

3.3. Optimization and experimental design

In this research, the experimental design using RSM in combination with CCD method was performed to investigate the effects of influential variables of pH (in the range of 2-8) (A), contact time (30-180 minutes) (B) and adsorbent dosage (1-5 g L⁻¹) (C) on nitrate removal efficiency. Due to the extensive use of research on (A), (B) and (C) parameters for the nitrate removal process, these parameters were selected as effective factors in optimizing nitrate removal [35-40] [41s,42s, This referenceshowed in supporting nformation page, SIP]. The RSM method is a mathematical and statistical method used for the analysis and empirical modeling of problems where a given answer is influenced by several variables and the RSM can be calculated to determine the optimal conditions. One advantage of this method is to reduce the number of empirical tests performed to obtain statistically valid results. In addition, the RSM method can also analyze the interactions between variables. Therefore, the use of this method in optimization can report more comprehensive and accurate data by performing the least number of experiments [43s-44s, SIP]. Table 2 shows the range of independent variables and design levels of the experiments examined in this study. The

results of the complete design of the test and the exact responses of the tests listed in Table 3. According to the results of the data analysis in Table 4, a quadratic function model can fit well to the empirical results. The fit of this model was evaluated by Analysis of Variance (ANOVA), normal probability plot and residual analysis. The quadratic function for nitrate removal efficiency is expressed as follows:

$$\% \text{Removal Nitrate} = 51.29 - (11.26 \times A) + (4.76 \times B) - (3.64 \times C) + (11.90 \times D) + (5.41 \times A \times B) + (3.69 \times A \times C) - (0.062 \times A \times D) + (3.16 \times B \times C) + 5.76 \times B \times D - (2.77 \times C \times D) + (0.52 \times A^2) + (0.89 \times B^2) + (3.23 \times C^2) - (1.75 \times D^2)$$

In the Table 4, the ANOVA analysis showed the importance of each parameter in response to nitrate removal by P and F values. The smaller the P value, the higher its impact factor and its contribution to the response variable. The P values less than 0.05 indicate that the model expressions are significant. The P values more than 0.1 indicate that the model terms are insignificant. Accordingly, the seven terms of (AC), (BD), and (C²) are significant parameters of the model and have the greatest effect on nitrate removal efficiency. The P values of the other terms were greater than 0.05, which means that their effect on the response model was not statistically significant.

Figure 5 shows the residual curve in terms of the

Table 2. Factors and levels for CCD study.

Level	pH	Tempure	Time
α-	22.4874	-4.31981	-13.7046
-1	3	5	1
+1	8	50	72
α+	472.487	59.3198	86.7046

Table 3. Experimental range and values of different variables studied.

Std	Run	Block	pH	Time (min)	nitrate (mgL ⁻¹)	absorbent (grL ⁻¹)	%Removal Nitrate(mgL ⁻¹)
5	1	Block 1	7	60	40	4	48.76
7	2	Block 1	3	150	100	4	81.23
11	3	Block 1	5	105	70	3	53.22
8	4	Block 1	3	60	40	2	71.66
12	5	Block 1	5	105	70	3	54.6
1	6	Block 1	7	150	100	2	47.13
10	7	Block 1	5	105	70	3	50.62
3	8	Block 1	7	60	100	4	38.62
9	9	Block 1	5	105	70	3	55.91
6	10	Block 1	3	60	100	2	57.84
2	11	Block 1	7	150	40	2	33.56
4	12	Block 1	3	150	40	4	93.51
14	13	Block 2	8	105	70	3	28.64
17	14	Block 2	5	105	20	3	63.28
20	15	Block 2	5	105	70	5	61.17
22	16	Block 2	5	105	70	3	53.76
21	17	Block 2	5	105	70	3	50.44
15	18	Block 2	5	30	70	3	40.62
18	19	Block 2	5	105	120	3	47.19
13	20	Block 2	2	105	70	3	66.51
19	21	Block 2	5	105	70	1	21.13
16	22	Block 2	5	180	70	3	56.62

Table 4. Experimental design and actual results of nitrate removal efficiency.

Source	Sum of Squares	df	Mean Square	F Value	p-value Prob > F
Block	374.47	1	374.47	-----	-----
Model	5147.23	14	367.66	20.32	0.0007
<i>significant</i>					
A-pH	717.07	1	717.07	39.64	0.0007
B-Time	128.00	1	128.00	7.08	0.0375
C-gr nitrate	181.09	1	181.09	10.01	0.0195
D-gr absorbent	801.60	1	801.60	44.31	0.0006
AB	97.08	1	97.08	5.37	0.0597
AC	109.00	1	109.00	6.03	0.0495
AD	0.013	1	0.013	7.024E-004	0.9797
BC	79.70	1	79.70	4.41	0.0806
BD	110.03	1	110.03	6.08	0.0487
CD	61.44	1	61.44	3.40	0.1149
A ²	4.23	1	4.23	0.23	0.6457
B ²	12.30	1	12.30	0.68	0.4411
C ²	160.98	1	160.98	8.90	0.0245
D ²	47.05	1	47.05	2.60	0.1579
Residual	108.53	6	18.09		
Lack of Fit	87.66	2	43.83	8.40	0.0370
<i>significant</i>					
Pure Error	20.87	4	5.22		
Cor Total	5630.23	21			

predicted response for response of nitrate removal efficiency. This Figure shows that all empirical data are uniformly distributed around the mean response variable. This indicates that the proposed model is sufficient and there has been no deviation from the hypotheses made. As can be seen in Table 5, the

difference between the adjusted R^2 and the predicted R^2 is less than 0.2 and the precision of the model is 19.613 (which is greater than 4), indicating the used model is accurate.

Figure 6 shows a comparison between the actual

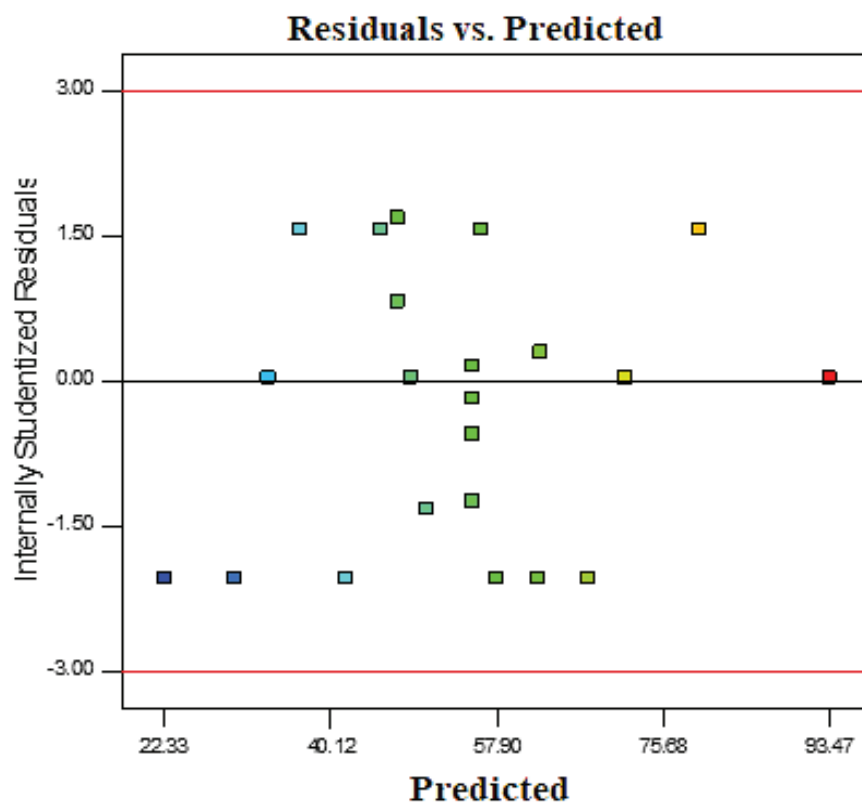


Fig.5. The residual value curve in terms of the predicted response

Table 5. Model equation statistical parameters for ANOVA model for nitrate removal efficiency.

Type of variables	Results
Std. Dev.	4.25
R-Squared	0.9793
Mean	53.46
Adj R-Square	0.9312
C.V. %	7.96
Pred R-Squared	-4.0544
PRESS	26564.71
Adeq Precision	19.613

response values obtained from the empirical results and the predicted response values obtained from the quadratic function model equation. It is observed that the model describes the empirical results and data fairly accurately, meaning that it has been successful in comparing the correlations between the three variables. In addition, there is a sufficient correlation with the linear regression coinciding with the R value of about 0.9793. In addition, Figure 7 shows the three-dimensional interaction curves of contact time, pH, adsorbent

dosage and initial nitrate concentration for nitrate removal efficiency. The highest nitrate removal efficiency was reported at the contact time of 150 min, pH value of 3, adsorbent dosage of 4 g L⁻¹ and initial concentration of 40 mg L⁻¹. Analysis of the diagrams in Figure 7 revealed higher nitrate removal efficiency at lower pH values and longer contact times.

3.4. Absorption isotherms and measurements

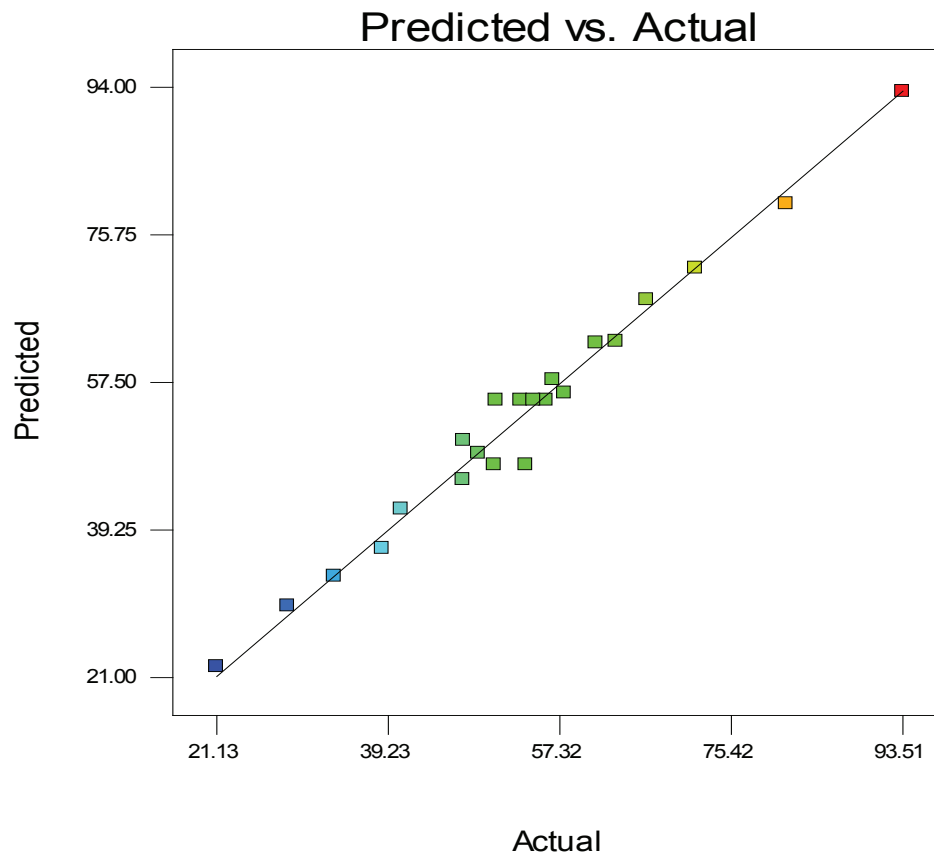
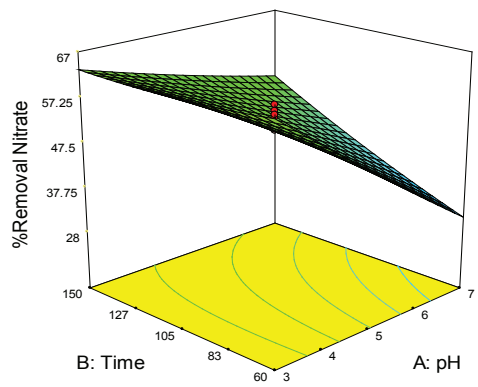
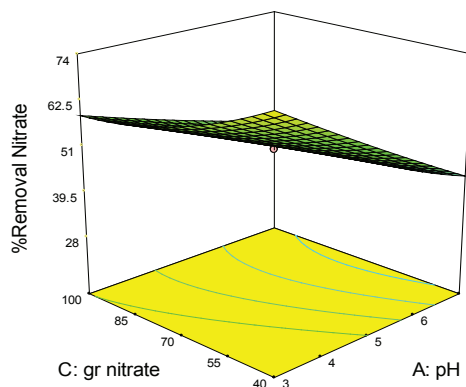


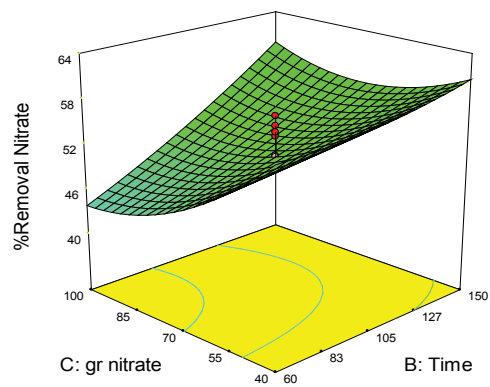
Fig. 6. Comparison between predicted and actual empirical values of nitrate removal efficiency



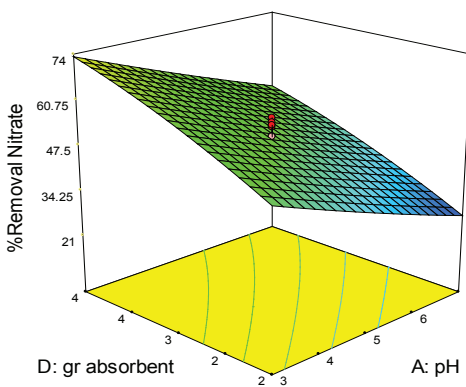
A



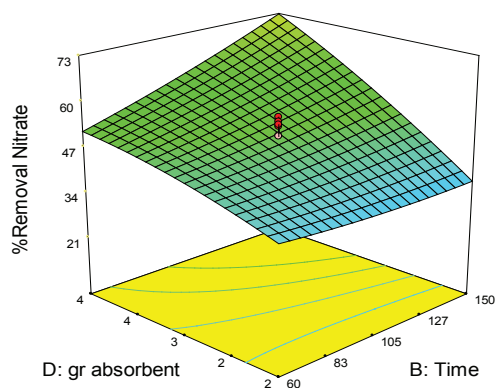
D



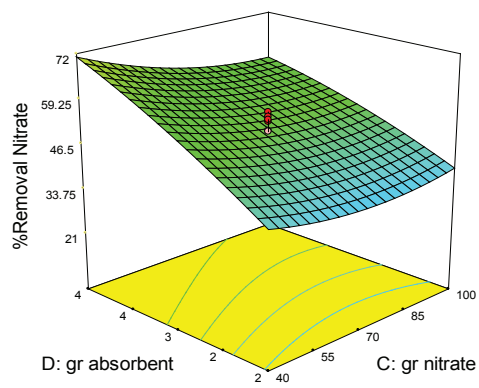
B



E



C



F

Fig.7. 3D response surface method curves of nitrate removal efficiency

The nitrate adsorption efficiency was measured by dissolving 4 g of adsorbent in 250 mL of nitrate solution at the initial concentrations of 20-120 mg at the contact time of 150 min at laboratory temperature and the stirring speed of 50 rpm. Finally, the equilibrium concentration of nitrate in solutions was determined by the UV-Vis spectrophotometry at 220 and 275 nm. The equilibrium nitrate adsorption capacity was calculated by the equation 5. Where, q_e is the equilibrium adsorption capacity (mg g^{-1}), C_e is the equilibrium concentration of nitrate ion (mg L^{-1}), V is the solution volume (L) and M is the adsorbent dosage (g).

$$q_e = (C_0 - C_e)V/M \quad (\text{Eq.5})$$

3.4.1. Nitrate adsorption isotherm

Nitrate adsorption on ZSM-5/Fe adsorbent was determined at laboratory temperature in terms of equilibrium concentration, as shown by the corresponding adsorption diagrams in Figures 8 and 9. Langmuir and Freundlich adsorption models were employed to evaluate the adsorption isotherm data. These models describe the relationship between the amount of ion adsorption desired on the adsorbent surface and its equilibrium concentration in the liquid phase. The Langmuir and Freundlich isotherms indicate mono-layer and multi-layer adsorption on surfaces, respectively. The Langmuir isotherm reveals active sites with a limited number, while the Freundlich equation represents heterogeneous surfaces [45s, SIP]. By

procedure, first the experimental data were fitted with Langmuir and Freundlich equations and then the constant parameters of the isotherm equations were calculated. The Langmuir and Freundlich models are explained by Equations 6 and 7, respectively.

$$q_e = (q_m K_L C_e) / (1 + K_L C_e) \quad (\text{Eq. 6})$$

$$q_e = K_F C_e^{1/N} \quad (\text{Eq. 7})$$

Where, q_m stands for the maximum adsorption capacity (mg g^{-1}), C_e for the equilibrium concentration of nitrate ion (mg L^{-1}), K_L for the constant of Langmuir isotherm (L mg^{-1}), and K_F (mg g^{-1}) and N are the constants of Freundlich isotherm.

According to the results, the correction factor for the Freundlich equation is larger than that for the Langmuir equation, indicating experimental data well-described with the Freundlich equation. This fact is probably due to the heterogeneous distribution of adsorption active sites on the adsorbent surface, because the Freundlich model assumes the adsorbent surface heterogeneity. The values of parameter N in Freundlich model are less than unit, which indicates an increase in bond energy with surface density and shows the optimal nitrate absorption conditions [46s-47s, SIP]. The effective parameters of isotherm models obtained from regression analysis of experimental data are reported in Table 6.

4. Conclusions

Table 6. Parameters of Langmuir and Freundlich adsorption isotherms for nitrate adsorption on ZSM-5/Fe adsorbent

R2	K_L (L mg^{-1})	q_m (mg g^{-1})	R2	N	K_F (mg g^{-1})
0.9881	0.290	8.072	0.9959	0.642	1.83

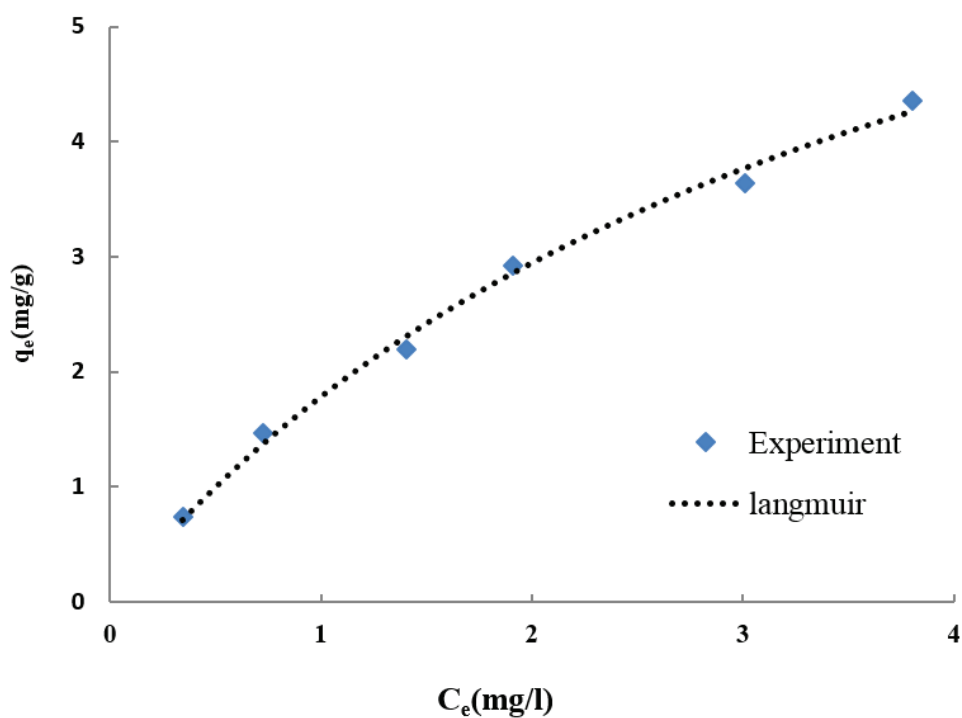


Fig. 8. Langmuir adsorption isotherm for nitrate adsorption on ZSM-5/Fe adsorbent

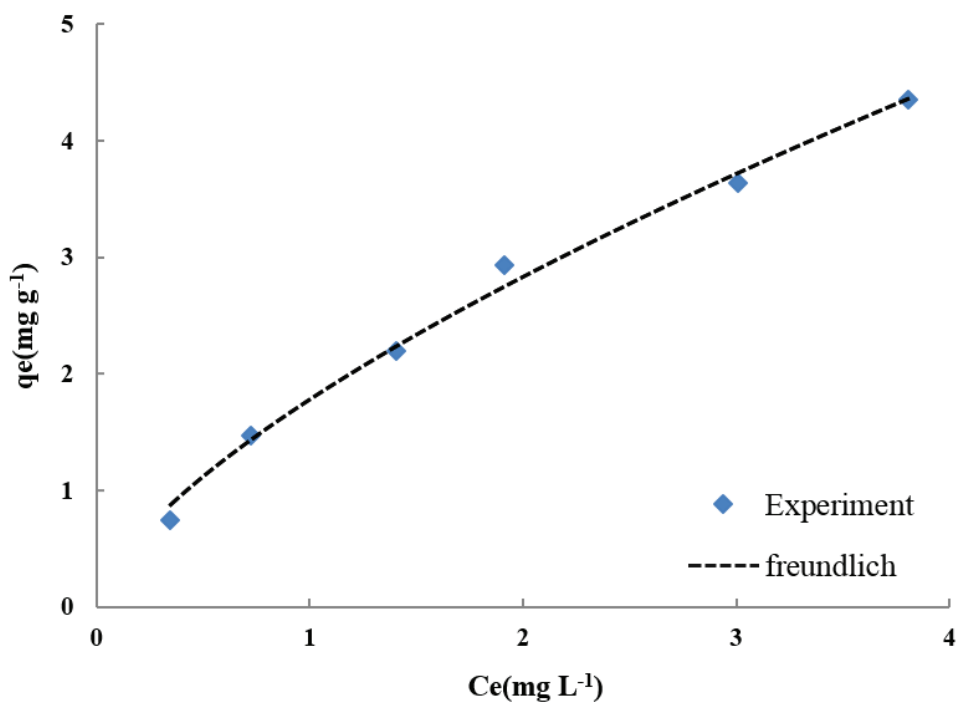


Fig. 9. Freundlich adsorption isotherm for nitrate adsorption on ZSM-5/Fe adsorbent

According to the results of the experimental design table, the pH value, contact time and initial nitrate concentration optimized for maximum nitrate removal (%93.51) were reported as 3, 150 minutes and 40 mg L⁻¹, respectively. In the results of the adsorption isotherms, the correction factor for the Freundlich equation is larger than that for the Langmuir equation, which shows that the experimental data are well described by the Freundlich equation, probably due to the heterogeneous distribution of active adsorption sites on the adsorbent surface because the Freundlich model assumes the adsorbent surface heterogeneity. The values of parameter N of the Freundlich model are less than unit, indicating the increase of bond energy with surface density and also the optimal conditions of nitrate adsorption. Therefore, it can be concluded that ZSM-5/Fe is a high efficiency nanosorbent for nitrate removal from aqueous solutions. The nitrate concentration in water samples was determined by UV-Vis spectrophotometry

5. Acknowledgments

The authors would like to thank and appreciate Hamid Reza Sardari, Personnel of Chemistry Laboratory at Islamic Azad University, South Tehran Branch, for providing laboratory facilities and equipment.

6. References

- [1] D.W. Cho, C.M. Chon, B.H. Jeon, Y. Kim, M.A. Khan, H. Song, The role of clay minerals in the reduction of nitrate in groundwater by zero-valent iron, *Chemosphere*, 81 (2010) 611-616. <https://doi.org/j.chemosphere.2010.08.005>
- [2] P. Mishra, R. Patel, Use of agricultural waste for the removal of nitrate-nitrogen from aqueous medium, *J. Environ. Manage.*, 90(2009)519-22. <https://doi.org/10.1016/j.jenvman.2007.12.003>
- [3] M. Nikaeen, S. Naseri, Evaluation of metallic iron (Fe⁰) application to remediate nitrate contaminated water, *Water Wastewater*, 17 (2007) 15-21. http://www.wwjournals.ir/article_2222.html?lang=en
- [4] S. Shadkam, F. Ludwig, P. van Oel, C. Kirit, P. Kabat, Impacts of climate change and water resources development on the declining inflow into Iran's Urmia Lake, *J. Great Lakes Res.*, 42 (2016) 942-952. <https://doi.org/10.1016/j.jglr.2016.07.033>.
- [5] Eslami A, Ghadimi M. Study of five years nitrite and nitrate content trends of Zanjan groundwater resources using GIS from 2006 to 2010, *J. Health Field*, 1 (2013) 30–6. <http://journals.sbmu.ac.ir/jhf>
- [6] R. Fouladi Fard, M. J. M. Abadi, M. R. Hosseini, Survey the nitrate concentration in drinking water distribution systems of Kashan county, Iran, *J. Saf. Environ. Health Res.*, 1 (2016) 36–39. <http://doi.org/10.22053/jsehr.2016.33387>
- [7] M. Dehghani, E. Haidari, S. Shahsavani, N. Shamsedini, Removal of nitrate in the aqueous phase using granular ferric hydroxide, *Jundishapur J. Health Sci.*, 7(2015) e26419. [http://doi.org/10.5812/jjhs.7\(2\)2015.26419](http://doi.org/10.5812/jjhs.7(2)2015.26419)
- [8] J. Rodríguez-Maroto, F. García-Herruzo, A. García-Rubio, C. Gómez-Lahoz, C. Vereda-Alonso, Kinetics of the chemical reduction of nitrate by zero-valent iron, *Chemosphere*, 74 (2009) 804-809. <http://doi.org/10.1016/j.chemosphere.2008.10.020>
- [9] I.F. Cheng, R. Muftikian, Q. Fernando, N. Korte, Reduction of nitrate to ammonia by zero valent iron, *Chemosphere*, 35 (1997) 2689–2695. [http://doi.org/10.1016/S0045-6535\(97\)00275-0](http://doi.org/10.1016/S0045-6535(97)00275-0)
- [10] Y.H. Huang, T.C. Zhang, Effects of low pH on nitrate reduction by iron powder, *Water Res.*, 38 (2004) 2631–2642. <https://doi.org/10.1016/j.watres.2004.03.015>
- [11] Y.M. Chen, C.W. Li, S.S. Chen, Fluidized zero valent iron bed reactor for nitrate removal, *Chemosphere*, 59 (2005) 753–759. <http://doi.org/10.1016/j.chemosphere.2004.11.020>
- [12] Y.H. Liou, S.L. Lo, C.J. Lin, C.Y. Hu, W.H. Kuan, S.C. Weng, Methods for accelerating nitrate reduction using zerovalent iron at near-neutral pH: effects of H₂-reducing pretreatment and copper deposition, *Environ. Sci. Technol.*, 39 (2005) 9643–9648. <http://doi.org/10.1021/es048038p><https://doi.org/>
- [13] S.C. Ahn, S.Y. Oh, D.K. Cha, Enhanced

- reduction of nitrate by zero-valent iron at elevated temperatures, *J. Hazard. Mater.*, 156 (2008) 17–22. <http://doi.org/10.1016/j.jhazmat.2007.11.04>
- [14] M. Dore, Ph. Simon, A. Deguin, J. Victot, Removal of nitrate in drinking water by ion exchange-impact on the chemical quality of treated water, *Water Res.*, 20 (1986) 221–232. [http://dx.doi.org/10.1016/0043-1354\(86\)90012-6](http://dx.doi.org/10.1016/0043-1354(86)90012-6)
- [15] S. Samatya, N. Kabay, U. Yuksel, M. Arda, M. Yuksel, Removal of nitrate from aqueous solution by nitrate selective ion exchange resins, *Reac. Funct. Polym.*, 66 (2006) 1206–1214. <http://doi.org/10.1016/j.reactfunctpolym.2006.03.009>
- [16] M. Chabani, A. Amrane, A. Bensmaili, Kinetic modelling of the adsorption of nitrates by ion exchange resin, *Chem. Eng. J.*, 125 (2006) 111–117. <http://doi.org/10.1016/j.cej.2006.08.014>
- [17] J.J. Schoeman, A. Steyn, Nitrate removal with reverse osmosis in a rural area in South Africa, *Desalination*, 155 (2003)15–26. [http://doi.org/10.1016/S0011-9164\(03\)00235-2](http://doi.org/10.1016/S0011-9164(03)00235-2)
- [18] M.I.M. Soares, Biological denitrification of groundwater, *Water Air Soil Pollut.*, 123 (2000) 183–193. <https://doi.org/10.1023/A:1005242600186>
- [19] A. Bhatnagar, M. Sillanpää, A review of emerging adsorbents for nitrate removal from water, *Chem. Eng. J.*, 168 (2011) 493–504. <http://doi.org/10.1016/j.cej.2011.01.103>
- [20] E.Y. Emori, F.H. Hirashima, C.H. Zandonai, C.A. Ortiz-Bravo, N.R.C. Fernandes-Machado, M.H.N. Olsen-Scaliente, Catalytic cracking of soybean oil using ZSM5 zeolite. *Catal. Today*, 279 (2017)168–176. <http://doi.org/10.1016/J.CATTOD.2016.05.052>.
- [21] Q. Zhang. G. Liu. L. Wang. X. Zhang, G. Li, Controllable decomposition of methanol for active fuel cooling technology, *Energy Fuels*, 28 (2014) 4431–4439. <http://doi.org/10.1021/ef500668q>
- [22] W. Li, G. Li, C. Jin, X. Liu, J. Wang, One-step synthesis of nanorod-aggregated functional hierarchical iron-containing MFI zeolite microspheres. *J. Mater. Chem. A*, 3 (2015) 14786–14793. <http://doi.org/10.1039/C5TA02662H>
- [23] T.J. Pinnavaia, Intercalated clay catalysts, *Sci.*, 220 (1983) 365–371. <http://doi.org/10.1126/science.220.4595.365>
- [24] K.G. Bhattacharyya, S.S. Gupta, Adsorption of a few heavy metals on natural and modified kaolinite and montmorillonite: a review, *Adv. Colloid Interface Sci.*, 140 (2008) 114–131. <http://doi.org/10.1016/j.cis.2007.12.008>
- [25] S. Wang, Y. Peng, Natural zeolites as effective adsorbents in water and wastewater treatment, *Chem. Eng. J.*, 156 (2010) 11–24. <https://doi.org/10.1016/j.cej.2009.10.029>
- [26] B. Kamarehie, E. Aghaali, S.A. Musavi, S.Y. Hashemi, A. Jafari, Nitrate removal from aqueous solutions using granular activated carbon modified with Iron nanoparticles, *Int. J. Eng. Transactions A*, 31 (2018) 554-563. <https://doi.org/10.5829/ije.2018.31.04a.06>
- [27] M. Mazarji, B. Aminzadeh, M. Baghdadi, A. Bhatnagar, Removal of nitrate from aqueous solution using modified granular activated carbon, *J. Mol. Liq.*, 233 (2017) 139-148. <https://doi.org/10.1016/j.molliq.2017.03.004>
- [28] L. Divband Hafshejani, A. Hooshmand, A.A. Naseri, A.S. Mohammadi, F. Abbasi, A. Bhatnagar, Removal of nitrate from aqueous solution by modified sugarcanebagasse biochar, *Ecol. Eng.*, 95 (2016) 101–111. <http://dx.doi.org/10.1016/j.ecoleng.2016.06.035>
- [29] T. Meftah, M. M. Zerfat, Nitrate removal from drinking water using organo-silane modified natural nano-zeolite, *Int. J. Nanosci. Nanotechnol.*, 12 (2016) 223-232. http://www.ijnnonline.net/article_22931.html
- [30] V. Alimohammadi, M. Sedighi, E. Jabbari, Response surface modeling and optimization of nitrate removal from aqueous solutions using magnetic multi-walled carbon nanotubes, *J. Environ. Chem. Eng.*, 4 (2016) 4525–4535. <http://dx.doi.org/10.1016/j.jece.2016.10.017>
- [31] A. Azari, A.H. Mahvi, S. Naseri, R. Rezaei

- Kalantary, M. Saberi, Nitrate removal from aqueous solution by using modified clinoptilolite zeolite, research center for environmental pollutants, Arch. Hyg. Sci., 3 (2014) 21-29. <http://jhygiene.muq.ac.ir>
- [32] S. Sepehri, M. Heidarpour, J. Abedi, Nitrate removal from aqueous solution using natural zeolite-supported zero-valent Iron nanoparticles, Soil Water Res., 9 (2014): 224–232. <https://doi.org/10.17221/11/2014-SWR>
- [33] E. Fataei, A. Seyyed Sharifi, H. Hasan Pour Kourandeh, A.S. Sharifi, S.T.S. Safavyan, Nitrate removal from drinking water in laboratory-scale using iron and sand nanoparticles, Int. J. Biosci., 10 (2013) 256-261. <http://dx.doi.org/10.12692/ijb/3.10.256-261>
- [34] A. Bhatnagar, E. Kumarb, M. Sillanpää, Nitrate removal from water by nano-alumina: characterization and sorption studies, Chem. Eng. J., 163 (2010) 317–323. <https://doi.org/10.1016/j.cej.2010.08.008>
- [35] R.M. McKeown, C. Scully, T. Mahony, G. Collins, V. O’Flaherty, Long-term (1243 days), low-temperature (4-15C), anaerobic biotreatment of acidified wastewaters, bioprocess performance and physiological characteristics, Water Res., 43 (2009) 1611-1620. <http://doi.org/10.1016/j.watres.2009.01.015>
- [36] C. Scully, G. Collins, V. O’Flaherty, Anaerobic biological treatment of phenol at 9.5-15 C in an expanded granular sludge bed (EGSB)-based bioreactor, Water Res., 40 (2006) 3737-3744. <http://doi.org/10.1016/j.watres.2006.08.023>
- [37] J. Lopez, V.M. Monsalvo, D. Puyol, A.F. Mohedano, J.J. Rodriguez, Low temperature anaerobic treatment of low-strength pentachlorophenol-bearing wastewater. Bioresour. Technol., 140 (2013) 349-356. <http://doi.org/10.1016/j.biortech.2013.04.049>
- [38] W.M. Bandara, H. Satoh, M. Sasakawa, Y. Nakahara, M. Takahashi, S. Okabe, Removal of residual dissolved methane gas in an upflow anaerobic sludge blanket reactor treating low-strength wastewater at low temperature with degassing membrane, Water Res., 45 (2011) 3533-3540. <http://doi.org/10.1016/j.watres.2011.04.030>
- [39] A.J.M. Stams, C.M. Plugge, Electron transfer in syntrophic communities of anaerobic bacteria and archaea, Nat. Rev. Microbiol., 7 (2009) 568-577. <http://doi.org/10.038/nrmicro2166>
- [40] T. Tian, S. Qiao, C. Yu, Y. Yang, J. Zhou, Low-temperature anaerobic digestion enhanced by bioelectrochemical systems equipped with graphene/PPy and MnO₂ nanoparticles/PPy-modified electrodes, Chemosphere, 218 (2019) 119-127. <http://doi.org/10.1016/j.chemosphere.2018.11.001>
- [SIP] SIP references (41-47s) have showed in supporting information page, <http://journal.amecj.com/index.php/AMECJ-01>



Recovery of Vanadium by ammonium chloride precipitation method using response surface methodology

Mahshid Gharagozlou^a, Hossein Sid Kalal^{b,*}, Alireza Khanchi^b,
Sohrab Ali Ghorbanian^a, Seyed Ebrahim Mosavi^a, Mohammad Reza Almasian^b,
Danial Niknafs^c, Akram Pourmatin^b, Neda Akbari^b

^a Department of Chemical Engineering, Faculty of Engineering, University of Tehran, Tehran, Iran.

^b Nuclear Fuel Research School, Nuclear Science and Technology Research Institute, AEOI, P.O. Box 3486-11365, Tehran, Iran.

^c Department of Chemistry, Mashhad Branch, Islamic Azad University, Mashhad, Iran.

ARTICLE INFO:

Received 6 Aug 2021

Revised form 27 Oct 2021

Accepted 25 Nov 2021

Available online 29 Dec 2021

Keywords:

Vanadium,
Recovery,
Ammonium chloride precipitation,
Alkaline leach solution

ABSTRACT

In this study, vanadium recovers from an alkaline solution based on the precipitation process and response surface methodology. A white salt ammonium metavanadate was obtained using the ammonium chloride precipitation method. Ammonium chloride was added directly to the alkaline liquor solution and the pH was adjusted approximately between 5 and 7 to form the white salt. The parameters affecting the recovery of vanadium, including the ammonium chloride concentration, the pH and the vanadium concentration in the caustic solution, were examined. The precipitation time had no significant influence on the vanadium recovery. The concentration of vanadium in the caustic solution and the concentration of ammonium chloride used for the precipitation were inversely related. It was found that a high recovery (over 90%) can be achieved with ammonium chloride and vanadium with concentrations over 4% (w/v) or 1000 mg L⁻¹ (in the lye solution). It has also been observed that working in the pH range of 5 to 7 results in over 90% recovery. The influence of the parameters mentioned on the recovery of impurities was examined and the optimal values determined. Ultimately, the maximum vanadium recovery (97.29%) was achieved at the optimal point obtained from the reaction surface methodology.

1. Introduction

Vanadium is of industrial and strategic importance due to its particular use. The main application of this element is in the steel industry. The highest production of vanadium in the world is in the form of vanadium pentoxide. Vanadium and its compounds are widely employed in the metallurgical, petrochemical, defense, electronics and paint and coating industries due to their excellent mechanical, catalytic, magnetic and other

physicochemical properties. The primary sources of vanadium compounds are ore feedstocks, concentrates, metallurgical slags, and petroleum residues [1,2]. Different methods have been applied for vanadium precipitation depending on leach solution (acidic, alkaline, or aqueous solutions). The followings are the studies and methods used to precipitate vanadium from these three leach solutions. Vanadium can be recovered from a leach solution by adjusting the pH with sulfuric acid or hydrochloric acid and adding an ammonium salt at temperatures between 22 and 28 °C [3]. Sodium hexavanadate Na₄V₆O₁₇ (red cake) can be

*Corresponding Author: Hossein Sid Kalal

Email: hsidkalal@aeoi.org.ir

<https://doi.org/10.24200/amecj.v4.i04.153>

precipitated by adding sulfuric acid with a pH of 2-3, and the precipitate is dissolved in an aqueous sodium carbonate solution. The red cake is cleaned and some impurities such as iron, aluminum, and silicon are separated from the solution by pH adjustment and precipitation. Then, ammonium chloride is added to the ammonium metavanadate precipitate. The calcination step is carried out, and vanadium pentoxide (V_2O_5) is finally obtained with a purity of 99.8% [4]. There is a relationship between the temperature of ammonium addition and the Precipitation Rate (PR), with the PR being 99.5% from 30 to 65°C while the PR decreases at temperatures below 35°C because the solubility of ammonium sulfate is not the same at different temperatures and dissolves faster at high temperatures. The presence of pollutants also affects the precipitation process. The sodium concentration influences the precipitation process, as sodium ions replace NH_4^+ ions. High sodium contents prevent the replacement of Na^+ by NH_4^+ . Therefore the amount should be controlled and below 25 g L⁻¹. The silicon concentration should be below 1.5 g L⁻¹. A high aluminum concentration prevents the formation of ammonium polyvanadate crystals, so the concentration should be below 0.1 g L⁻¹ [5]. In another study, the technology for extracting vanadium from coal was investigated. Scholars were able to precipitate ammonium metavanadate by leaching (with water) and adding acid (sulfuric acid or hydrochloric acid) to form polyvanadate. The precipitate was dissolved with sodium hydroxide, and ammonium salt was added. Then, calcination process was performed at 550 °C. Finally, vanadium pentoxide was obtained [6, 7]. Based on research by Wang et al., they worked on an alkaline sodium hydroxide leach solution containing 84.45 gL⁻¹ vanadium pentoxide.

Ammonium metavanadate was precipitated by adjusting the pH with hydrochloric acid in the range of 8 to 8.5. Ammonium chloride was added at 40 - 45 °C. Then, vanadium pentoxide was obtained with a purity of 99.12% by calcination at 550 °C for one hour [8]. Iron and nickel do not enter the solution in alkaline leaching with sodium hydroxide, but

aluminum and silicon enter the solution with vanadium. During acid leaching, sulfuric acid, iron, nickel, aluminum, and silicon enter the solution with vanadium. In leaching with sodium carbonate, only aluminum is introduced, and other metals do not get into the solution with vanadium. In the alkaline leaching process, sodium hydroxide was precipitated by adjusting the pH to 8 with sulfuric acid in the absence of ammonium chloride, aluminum, and silicon, while vanadium was in the solution. The addition of 1-2 M ammonium chloride solution and adjustment of the pH to 5 was resulted in the formation of a vanadium precipitate [9]. The technology of vanadium extraction from coal was also developed in another study. The focus was on cleaning the alkaline leach solution to remove silicon and aluminum. This purification took place in two stages. In the first stage, most of the sulfuric acid impurities were removed by adjusting the pH in the range of 8 to 9. In the second stage, the remaining silicon, aluminum, and other impurities such as phosphorus were removed by chemical precipitation. The chemical precipitation was obtained by adding 8 g L⁻¹ magnesium nitrate and 10 ml L⁻¹ ammonia at 60°C for 1 hour in a shaker with a speed of 500 rpm. The vanadium recovery in this process was 94.25% [10]. In another study, the focus was on vanadium recovery from consumer catalysts. Acid leaching and precipitation were performed by adjusting the pH to 6 – 7 with 1 M sodium carbonate solution. It was found that precipitation at pH levels above 7 should be avoided as this will lead to the precipitation of nickel and other metals [11]. The precipitation of vanadium can be achieved by adding ammonium chloride and an alkali such as sodium hydroxide to an acidic leach solution to adjust the pH. The solubility of sodium metavanadate increases with the pH value of the alkaline solution and temperature. Vanadium pentoxide was obtained with a purity of 99% [12]. In the recovery of vanadium from the acidic leach solution of charcoal, scholars could obtain vanadium pentoxide with a purity of 99%. Ammonium chloride was added to a solution at a pH of about 2, and the precipitate of ammonium

vanadate was taken out. The precipitate was roasted at 520 °C for 2 hours, and vanadium pentoxide was obtained with a purity of 99% [13]. The recovery of molybdenum and vanadium from consumable catalysts was investigated. Ammonium chloride is widely used for vanadium precipitation in the industry because of its economic cost. An excessive amount of ammonium chloride is required because excess ammonium chloride causes vanadium precipitation and ammonium solubility. As a result, the solubility of ammonium vanadate in the solution decreases as the ammonium chloride concentration increases. More than 99% of vanadium precipitates if the concentration of vanadium pentoxide in the solution is 25 g L⁻¹, and the concentration of ammonium chloride is more than 40 g L⁻¹. It was found that the concentrations of vanadium pentoxide in the leach solution and ammonium chloride are heavily involved in the vanadium precipitation process and are interdependent. It is also stated that the precipitation reaction takes place at pH range of 8 to 9 [14,15]. Based on studies carried out and considering that the Saghand ore is of the titanium magnetite type and the amount of vanadium in the ore is about 5000 mg L⁻¹, the suitable method for vanadium recovery from this ore type is salt roasting with sodium carbonate and leaching with hot water. The leach solution used in our study has been prepared under the same conditions, ie salt roasting and leaching with hot water, and the precipitation process has been performed in the alkaline solution obtained by leaching with hot water. The reason for choosing the precipitation method is its low cost and simplicity of the process. Therefore, such a process is of great importance for large-scale use due to industrial needs and constraints. A thorough review of similar studies revealed that complete and accurate information about the optimal conditions for vanadium precipitation is not available. In this study, preliminary experiments were performed to determine the optimal precipitation conditions. The important parameters including ammonium chloride concentration, pH, precipitation time and vanadium concentration in the leach solution were investigated and their optimal values were specified

2. Experimental

2.1. Materials and analytical instruments

All materials and reagents including FeCl₃ (99%), NaVO₃ (98.5%), Al(NO₃)₃·9H₂O (95%), Ca(NO₃)₂ (100%), Mg(NO₃)₂·6H₂O (99%), Na₂MoO₄·2H₂O (99.5%), K₃PO₄·3H₂O (99%), SiO₂ (99%), NH₄Cl (99.5%), HCl (37%), H₂SO₄ (98%) and (NH₄)₂CO₃ (99.9%) were provided by Merck (Germany) in analytical grade. All solutions were made with deionized water. Concentration of the ions in the solutions was determined using inductively coupled plasma (ICP) (Varian liberty 150 XL). Inductively coupled plasma spectroscopy is a method of emission spectroscopy in which the atomization takes place with the aid of plasma that is generated by an inert gas, mainly argon. This method is used for elemental analysis (mainly cations) of most elements.

2.2. Precipitation process

First of all, the Saghand ore was roasted with 50% by weight sodium carbonate at 900 °C for two hours. Then, leaching was carried out with hot water at 90 °C for three hours with a liquid to solid ratio of 1 to 3. Impurities in the leach solution were identified by ICP analysis (Table 1). According to the exact amount of impurities, a simulation solution was prepared. The Saghand ore leach solution is in an alkaline media (pH about 10) and the simulation solution was made under the same condition. The salts listed in Table 2. and Table 3. Were used to prepare the alkaline leach solution. Vanadium precipitation from alkaline leach solutions can be carried out in two methods. In first method, by adjusting the pH value (pH = 2), the red precipitate of ammonium polyvanadate is formed together with some impurities. The red precipitate is dissolved in dilute sodium carbonate solution and impurities are removed by setting the pH value. Then ammonium chloride is added and the ammonium metavanadate precipitate is formed. In second method. Ammonium chloride is added directly to the alkaline leach solution and the pH value is set in the range of 5 to 7 to form the white salt called ammonium metavanadate. If the

Table 1. Chemical composition of the vanadium-associated impurities in the leaching solution

Composition	Al	Ca	Fe	Mg	Mo	P	Ti	Na	Si
Concentration, mg L ⁻¹	10.583	3.6	0.455	1.81	32.283	0.56	0.036	1383.33	72.916

Table 2. The precipitates of sodium vanadate salts

No.	pH	Vanadium Recovery (%)	Sodium (%) in precipitation
1	1.028	17.50	0.660
2	1.368	80.83	1.486
3	1.544	90.65	1.134
4	1.876	97.64	0.451
5	2.045	94.43	0.515
6	4.566	73.47	2.619
7	5.023	46.98	2.619
8	5.540	95.17	2.579
9	5.850	90.11	2.714
10	6.024	95.53	2.013
11	6.040	94.52	1.371
12	6.734	98.84	0.224

Table 3. Influence of the concentrations of vanadium in sodium vanadate salts in the presence of NH₄Cl and pH value of 5

Vanadium concentration, mg L ⁻¹	Ammonium chloride concentration (% w/v)								
	10				2.5				
	100	200	500	800	500	800	1000	2000	3000
Vanadium recovery (%)	91.125	95.396	95.833	97.948	66.433	94.406	98.125	99.125	99.288

amount of impurities in the leach solution is low, the second is recommended and there is no need for a separate step to remove impurities. Therefore, we employed the second method because the amount of impurities in the alkaline leach solution used in our study is low. In this study, the concentrated ammonium chloride was added to an alkaline leach solution. The pH was adjusted in the range of 5 – 7 with 0.5 M HCl. A white precipitate was formed, which corresponds to the ammonium metavanadate. The resulting precipitate was then washed with 2.5% ammonium chloride solution (w/v). Finally, the resulting precipitate dried at room temperature.

3. Results and discussion

3.1. Effect of pH

Preliminary tests were carried out to determine the optimal pH range for the vanadium precipitation on sodium vanadate salt. Sodium metavanadate (NaVO_3) with a purity of 98.5% and NH_4Cl with a purity of 99.8% were used in these experiments. Besides, 0.5 M HCl (with a purity of 32% and a density of 1.16 kg L^{-1}) was used to adjust the pH. In this case, 2.085 g of NaVO_3 was dissolved in 252 mL of distilled water. Then, 28 mL of 25% ammonium chloride (w/v) was added so that its amount in water was 2.5% (w/v). Finally, the pH was adjusted with 0.5 M HCl. Based on the experiments' results (Table 2), the highest vanadium recovery occurred at pH values close to 2 to and close to 7. Vanadium has polyvanadate and metavanadate structures at pH 2 and 7, respectively. For the rest of the experiments, the pH value was considered to be 7 for high vanadium recovery and minimum recovery of sodium.

3.2. Effect of ammonium chloride and vanadium concentrations

In order to investigate the influence of ammonium chloride concentration in sodium vanadate solution on the vanadium recovery, a solution containing sodium vanadate with different concentrations in the range of 100 to 3000 mg L^{-1} was tested by adding ammonium chloride salt at a pH of about 5.5. The corresponding results are shown in Table 3.

We find from the results in Table 3. that a vanadium recovery of 98% with a vanadium concentration of 1000 mg L^{-1} can be achieved in the presence of 2.5% ammonium chloride. At low vanadium concentrations, 10% ammonium chloride (which is a very high concentration) is required for a vanadium recovery of more than 95%. Similar experiments were carried out in simulation solution to examine the effect of ammonium chloride concentration. Finally, the concentration range of ammonium chloride was determined. The experiments were carried out under $\text{pH} = 5.5$, a precipitation time of 2 hours, and a 1000 mg L^{-1} vanadium concentration. Figure 1a shows how an increase in the ammonium chloride concentration affects the recovery of vanadium. With regard to the vanadium concentration (1000 mg L^{-1}), it is observed that an ammonium chloride with concentration of about 12% (w/v) must be used to achieve a recovery of over 90%, which is economically and industrially unprofitable. These tests show that the amount of ammonium chloride used depends on the vanadium concentration in the leach solution. The experiments were carried out under $\text{pH} = 6.35$, a precipitation time of 16 hours, and a vanadium concentration of 2100 mg L^{-1} . In Figure 1b, the effect of increasing the ammonium chloride concentration on the vanadium recovery can be observed. Ammonium chloride was added in the range of 6 to 14 % (w/v) to the solution containing 2100 mg L^{-1} of vanadium. The recovery rate of vanadium was over 95%. Increasing the concentration of ammonium chloride leads to increased vanadium recovery. Since Saghand ores contain about 5400 mg L^{-1} of vanadium, a range between 2 to 8% for the concentration of ammonium chloride and a range between 1400 and 2700 mg L^{-1} for vanadium concentration were considered for the remaining tests.

3.3. Effect of precipitation time

The result of time evaluation is shown in Figure 2a. These tests were carried out under $\text{pH} = 6.35$, 10% (w/v) ammonium chloride, different times, and vanadium concentration of 2100 mg L^{-1} .

The results showed that the increase in time did not significantly affect vanadium recovery. The difference in recovery rates related to precipitation data is less than 1% with a maximum and minimum time of 30 and 2 hours, respectively. So, it is better to choose the shortest time for precipitation to achieve the maximum recovery of vanadium. According to empirical observations, by increasing precipitation time, the amount of impurities in vanadium rises significantly. To prove this claim, the effect of time on the recovery of impurities, including aluminum,

molybdenum, sodium, and silicon was investigated. Over time, as shown in Figure 2b, this can lead to an increase in the amount of contaminants on ammonium metavanadate precipitate. In the case of elements such as silicon and aluminum, the passage of time, in contrast to molybdenum and sodium, significantly influenced the increase in ion precipitation. Our goal is to minimize the pollution caused by ammonium metavanadate precipitation. As described above, two hours was considered optimal for the precipitation process.

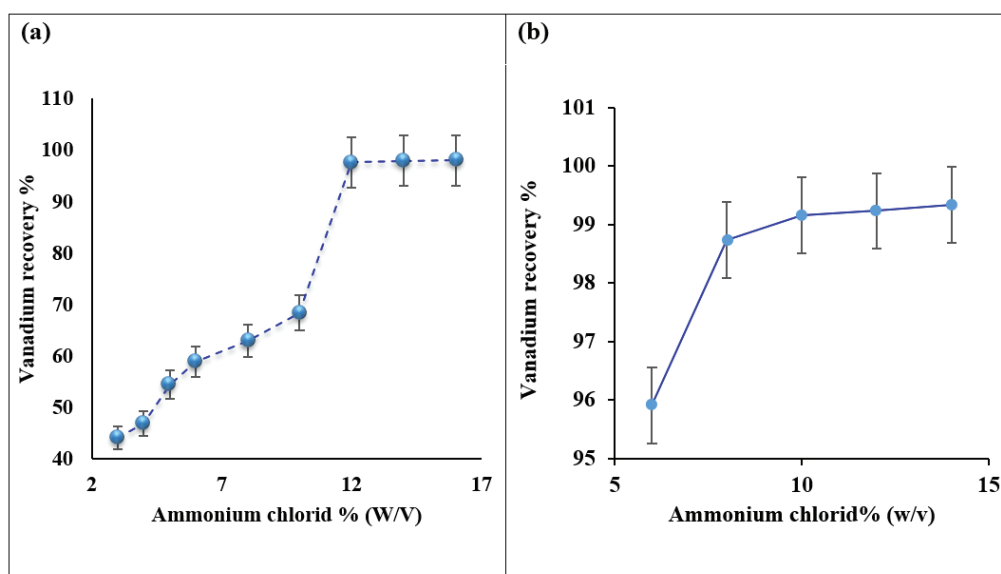


Fig. 1. Influence of the ammonium chloride concentration on the vanadium recovery for a solution with vanadium concentration of 1000 mg L⁻¹ (a) and 2100 mg L⁻¹ (b).

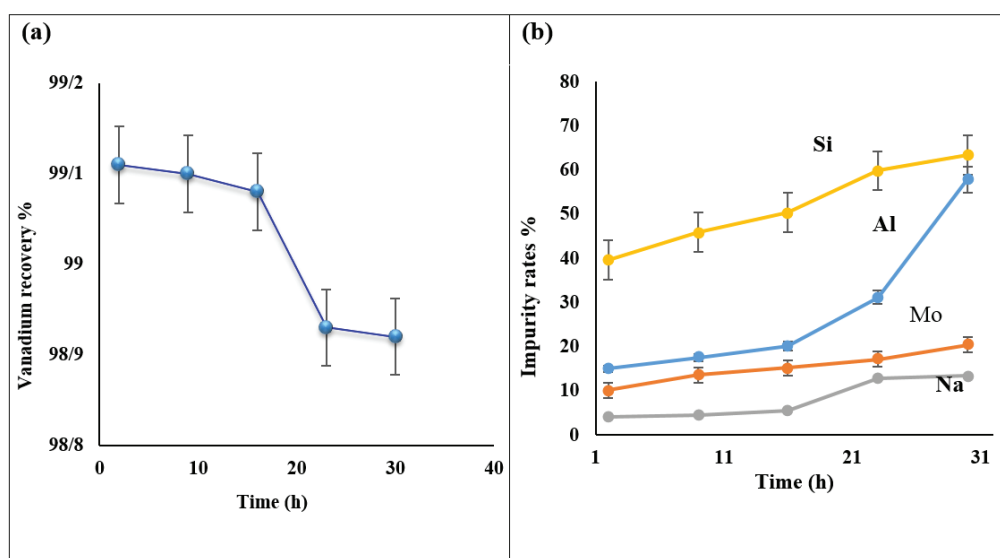


Fig. 2. a) Effect of time on vanadium recovery, b) Influence of time on the precipitation of various ions on ammonium metavanadate

3.4. The simultaneous effect of important parameters using design expert software

3.4.1. Design of experiments

The DOE (Design of Experiment) method is one of the new statistical methods that can be used to identify important variables that affect the product's quality. By Using DOE techniques, we can first identify the variables that will have the greatest impact on the output. Second, the effective input variables are determined to bring the response values closer to their nominal value, reduce their variability, and minimize the influence of uncontrollable factors on the response variable. One technique that is widely used to optimize the input variables is response surface methodology (RSM). Central composite designs, abbreviated as CCD or Box-Wilson, are common methods for response surface design. The CCD method is used to design experiments. In the CCD method, each factor has five different levels (including three points within limits specified for each factor and two points outside

the limits specified for each factor). CCD design is usually done in five stages, including $-\alpha$, -1 , 0 , $+1$, $+\alpha$. About the mentioned stages, -1 and $+1$ are the upper and lower levels, and $-\alpha$ and $+\alpha$ are the new limits of the factors. Zero is also at the heart of the design. In this experiment, the CCD experiment design was performed using the design-expert software to obtain the relationship between the three process variables. For the three variables pH ($X_1=A$), weight-volume percentage of the ammonium chloride concentration ($X_2=B$), and vanadium concentration in the leaching solution ($X_3=C$), 20 experiments were carried out to determine the interaction of the parameters. Each time the parameter is designed and executed by the software by determining the optimal point. The specifications of each Central Composite Design (CCD) test and their results are shown in Table 4. The experiment design was carried out with three factors in mind. The order and the range of the factors are given in Table 4. And the precipitation time was considered to be 2 hours.

Table 4. Design of the experiments

Std.	Run	Block	A: pH	B: NH ₄ Cl % w/v	C: V ₂ O ₅ mg L ⁻¹
11	1	1	6.15	2.98	2100
5	2	1	5.6	4	2500
3	3	1	5.6	7	1700
6	4	1	6.7	4	2500
19	5	1	6.15	5.5	2100
12	6	1	6.15	8.02	2100
17	7	1	6.15	5.5	2100
1	8	1	5.6	4	1700
7	9	1	5.6	7	2500
4	10	1	6.7	7	1700
13	11	1	6.15	5.5	1427.28
18	12	1	6.15	5.5	2100
15	13	1	6.15	5.5	2100
10	14	1	70.7	5.5	2100
20	15	1	6.15	5.5	2100
2	16	1	6.7	4	1700
9	17	1	5.23	5.5	2100
16	18	1	6.15	5.5	2100
14	19	1	6.15	5.5	2772.72
8	20	1	6.7	7	2500

3.4.2. Analysis of results

As shown in Figure 3a, pH changes have no significant effect on the increase or decrease in vanadium recovery. The recovery rate was almost high in the pH range under study. The low vanadium recovery was due to the low concentration of ammonium chloride. The pH values in the range of 5 to 7, with which the white precipitate of ammonium metavanadate is to be captured, can achieve high recovery of vanadium. So, the selection of all pH values in this range is acceptable. As shown in Figure 3b, the effect of pH on increasing vanadium recovery is not significant in this range. It has a maximum recovery for vanadium at pH=6.15 with an ammonium chloride (NH_4Cl) concentration of 7% (w/v). The arc curvature in the diagram (2b) at NH_4Cl concentration of 4 to 7% (w/v) and pH of 5.6 is approximately similar to the curvature of the arc at NH_4Cl concentration of 4 to 7% (w/v) and pH value of 5.88. Based on Figure 3C, at some vanadium concentrations (2100 mg/L), the recovery is below 60% of vanadium. This significant difference is due to the insufficient concentration of the ammonium chloride used (the minimum concentration used was 2.98% (w/v)). It can be concluded that the vanadium precipitation depends on both the concentration of ammonium chloride and the concentration of vanadium in the leaching solution. It was also found that the minimum concentration of ammonium chloride used, i.e., 2.98% (w/v), is what was considered for the formation of ammonium metavanadate. According to Figure 3b, it is evident that the vanadium recovery continues to grow with increasing ammonium chloride concentration. In this connection, the concentrated leaching solution leads to the high recovery of up to 100% vanadium. Fig.c also shows that the recovery of over 80% of vanadium can be achieved with the ammonium chloride concentration in the range of 4 to 6% (w/v), which is economically and industrially justified. As shown in Figure 3d, the vanadium recovery increased from 57% to 99% with growing ammonium chloride concentration

from 2.98% to 8.02% (w/v). It is clear that to achieve vanadium recovery above 80%, ammonium chloride concentrations above 4% (w/v) must be used. From the results of the tests, it can be concluded that the vanadium and ammonium chloride concentrations have to be correlated with the inverse ratio in the leaching solution so that the vanadium concentration in the leaching solution is less than 1000 mg L^{-1} , which means that the ammonium chloride requires a concentration about 12% (w/v) to achieve vanadium recovery of over 90%.

3.5. The effect of important parameters on recovery of impurities

3.5.1. Aluminum recovery

Figure 4a shows the effect of pH and ammonium chloride concentration on aluminum precipitation. As can be seen, the amount of aluminum precipitation grew slightly with increasing pH and ammonium chloride concentration. In order to reduce impurities in vanadium to a minimum, the ammonium chloride concentration and pH value were chosen to be in the range of 4 - 6% (w/v) and 5.5-6.5, respectively. From Figure 4b, it is known that the higher the vanadium concentration in the leaching solution, the more aluminum is deposited, so that the effect of the pH value is negligible compared to the vanadium concentration in the leaching solution. Therefore, it is better to use leach solutions with a higher liquid-to-solid (L/S) ratio to minimize the amount of contamination in vanadium. According to Figure 4c, it is clear that the precipitation of aluminum rises with increasing concentrations of ammonium chloride and vanadium in the leaching solution. For example, in a leach solution with a vanadium concentration of 1700 mg L^{-1} and an ammonium chloride of 4% (w/v), the amount of aluminum precipitation reached about 40%, while in a leach solution with a vanadium concentration of 2500 mg L^{-1} and ammonium chloride with a concentration of 7% (w/v) is about 65%. Since our goal is to minimize the amount of impurities in vanadium, the first leaching solution is preferable.

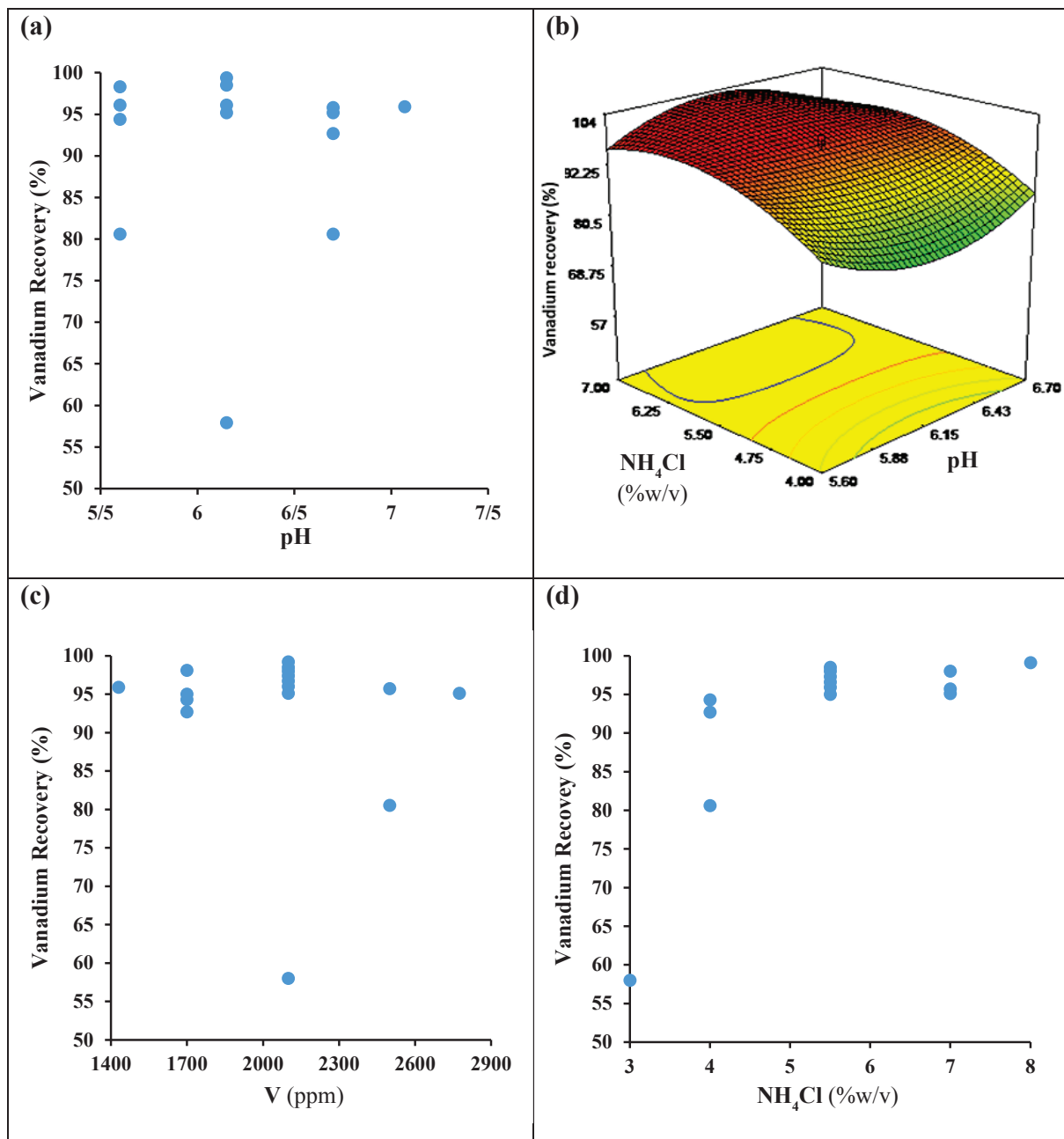


Fig. 3. Influence of pH value (a), Effect of ammonium chloride concentration and pH value on vanadium recovery(b), vanadium concentration (c) and ammonium chloride concentration (d) on the recovery of vanadium

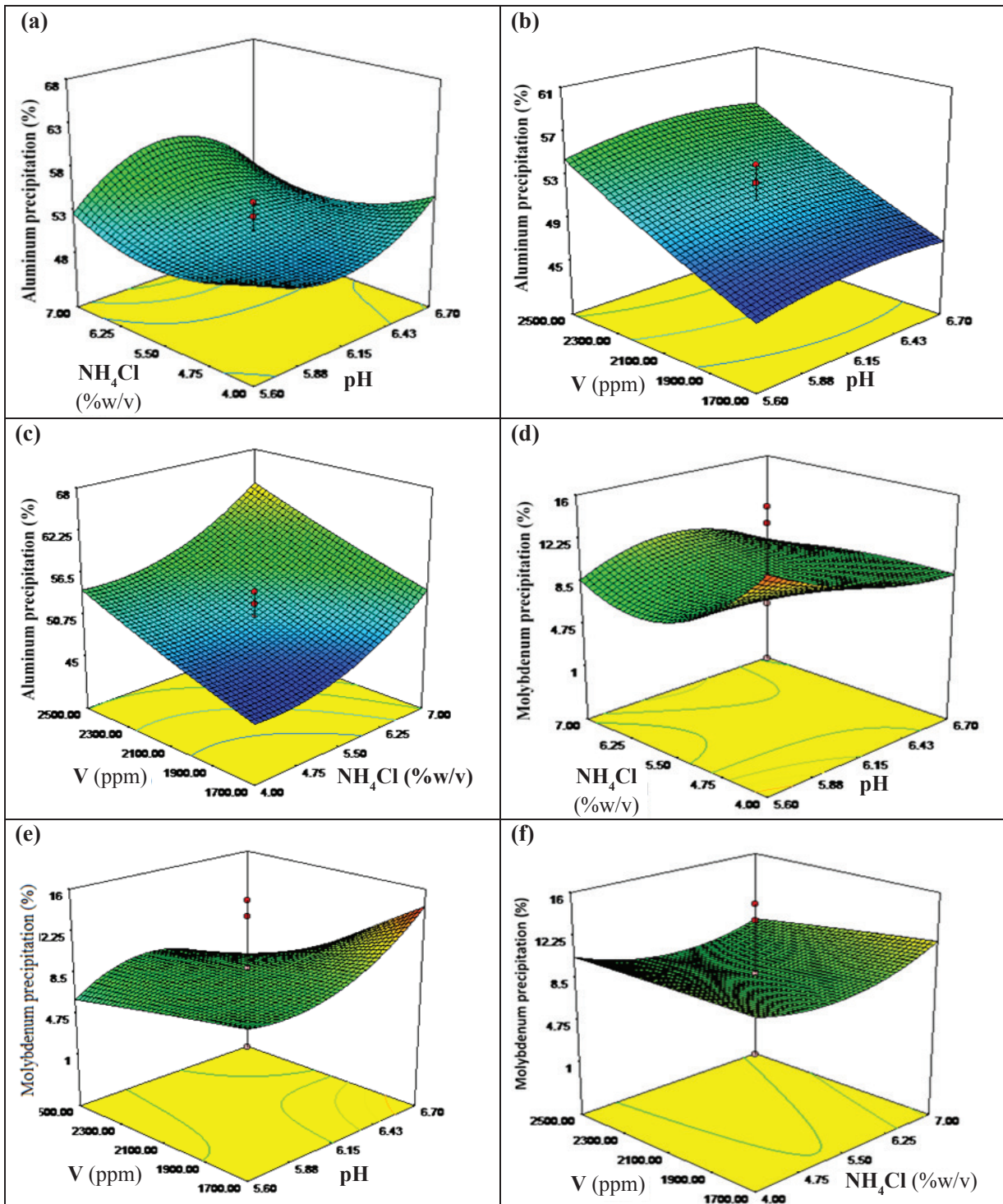


Fig. 4. Influence of pH value, vanadium concentration and ammonium chloride concentration on the recovery of Aluminium (**a – c**) Influence of pH value, vanadium concentration and ammonium chloride concentration on the recovery of Molybdenum (**d – f**)

3.5.2. Molybdenum recovery

It is clear from Figure 4d that the increase in pH, slightly reduces the amount of molybdenum precipitation. It is known that with increasing or decreasing the ammonium chloride concentration, the amount of molybdenum deposition varies between 8% and 10%. The minimal molybdenum precipitation is observed at an ammonium chloride concentration of 4.5 to 5.5% (w/v) and a pH of about 5.5 to 6.5. According to Figure 4e, it is observed that the rising in pH leads to an increase in the amount of molybdenum precipitation, but this increase is more pronounced for vanadium concentrations in leaching solution between 1700 to 2100 mg/L. Since our goal is to minimize the amount of molybdenum precipitation, a pH in the range of 5.5 to 6 was chosen. It is understandable from Fig. 3f that changes in the concentrations of ammonium chloride and vanadium in the leaching solution have little effect on molybdenum precipitation. According to the figure, the least amount of molybdenum precipitation is observed at concentrations of 5.5% (w/v) and 1200 mg L⁻¹ for ammonium chloride and vanadium, respectively. In

order to minimize the molybdenum precipitation, it is better to carry out experiments in this medium.

3.5.3. Sodium recovery

Based on Figure 5a, the sodium precipitation goes up with increasing vanadium concentration in the leaching solution. The highest amount of sodium precipitation was at a pH of 6.5 and a vanadium concentration of 2500 mg L⁻¹, and the lowest amount was at a pH range between 5.5 to 6.5 and a vanadium concentration of about 1700 mg L⁻¹. In this case, it is advisable to carry out the tests in the minimum point range. From Figure 5b, we can find that that increasing the vanadium concentration in the leaching solution leads to an expansion in the amount of sodium precipitate. In fact, the higher the concentration of the leach solution, the greater the deposition of other contaminants, including sodium along with ammonium metavanadate. Figure 5b also shows that increasing the ammonium chloride concentration at high vanadium concentrations reduces sodium precipitation. On the other hand, sodium formation is minimized at the minimum concentration of ammonium chloride and vanadium.

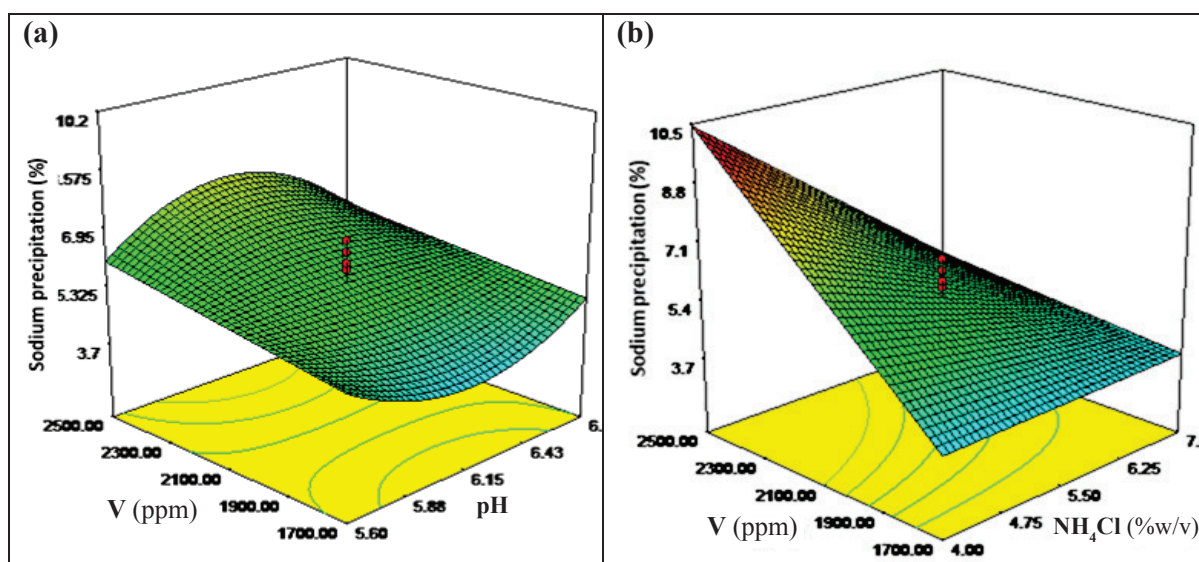


Fig. 5. Influence of pH value, vanadium concentration and ammonium chloride concentration on the recovery of Sodium (a, b)

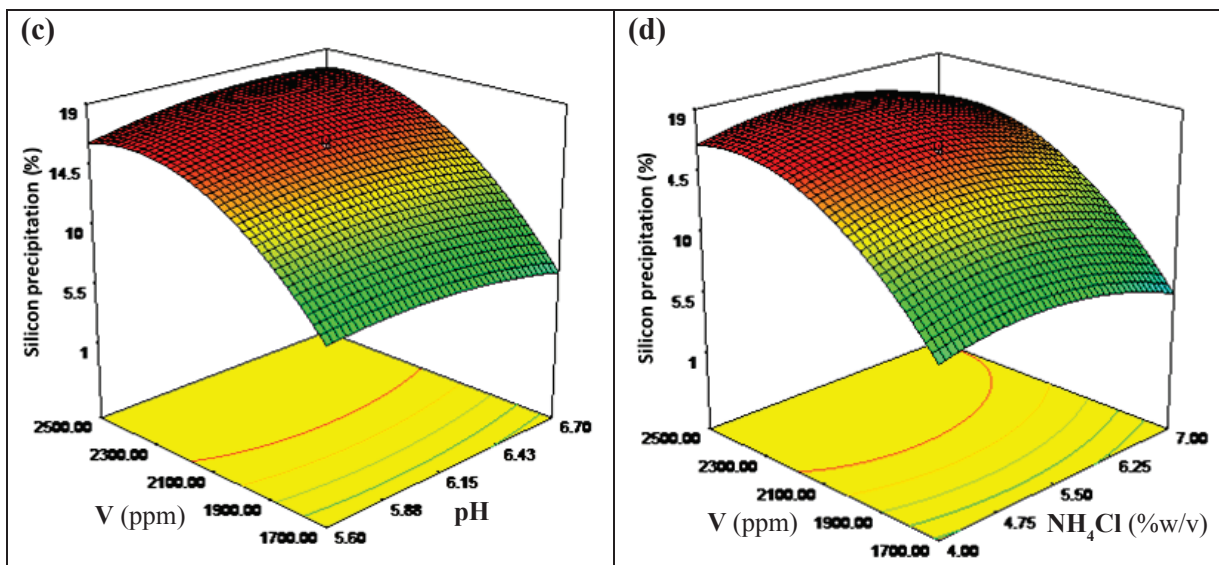


Fig. 5. Influence of pH value, vanadium concentration and ammonium chloride concentration on the recovery of Silicon (c, d)

3.5.4. Silicon recovery

The effect of the vanadium concentration and pH on the silicon precipitation in the leaching solution is shown in Figure 5c. One can deduce that the higher the vanadium concentration in the leaching solution, the higher the amount of silicon precipitation. The pH parameter had no significant influence on the formation of the silicon deposit. The vanadium concentrations below 2000 mg L⁻¹ and a pH of around 5.5 to 6.15 should be selected to minimize silicon sedimentation. It can be seen in Figure 5d that increasing the vanadium concentration in the leach solution increases the amount of silicon precipitation. An increase in the ammonium chloride concentration also has a minor influence on the amount of silicon deposit. The minimum amount of impurities can be achieved at a concentration of 4 to 5% (w/v) ammonium chloride and a vanadium concentration below 1000 mg L⁻¹.

3.6. The optimal point with maximum vanadium recovery

At the optimal point, we have the maximum recovery of vanadium and minimum precipitation of contaminants in the leach solution. The specified optimal point suggested by the software has the following conditions (Eq.1)

NH₄Cl conc. = 5.48% (w/v), pH = 5.82, Vanadium concentration in the leach solution = 1700 mg L⁻¹ (Eq.1)

The important factors during designing the tests are shown in Table 5. The p-value for the parameters determines the significance and influence of the factor. The more the p-value is less than 0.05, the more effective. The parameter of Lack of fit specifies the fitting of the data with the model. The more the p-value for the Lack of fit exceeds 0.05, the better the fit. Also, the amount of (R-Sq = 98.83% or R-Sq (Adj) = 97.10%) should be taken into account, which is acceptable for the design of the test.

The equation 2 obtained by the software is as follows:

$$R.V = (+5709.94005) - (1843.48600 * pH) - (612.88936 * NH_4Cl) - (1.05601 * V) + (208.76649 * pH * NH_4Cl) + (0.33175 * pH * V) + (5.05000E-003 * NH_4Cl * V) + (149.50072 * pH^2) - (2.79322 * NH_4Cl^2) - (16.99333 * pH^2 * NH_4Cl) - (0.026768 * pH^2 * V)$$

Where: NH₄Cl is the concentration of ammonium chloride, and V is the vanadium concentration in the leach solution. According to Table 6, vanadium with a high recovery and high purity (low contamination) can be obtained at the point where the software determines to be the optimal point. Therefore, this point was considered as the optimal point for the set of these tests.

Table 5. Results obtained from Design-Expert ANOVA

Source	p-value
pH	0.3742
V ₂ O ₅	0.8193
NH ₄ Cl	0.0001 <
pH * V ₂ O ₅	0.3713
pH * NH ₄ Cl	0.7308
NH ₄ Cl * V ₂ O ₅	0.0006
Lack of fit	0.2031 not significant

Table 6. Results obtained from the experiment at the optimal point

Vanadium mg L ⁻¹	ammonium chloride % w/v	pH	Vanadium recovery %	Vanadium Purity %
1700	5.48	5.82	97.29	88.89

4. Conclusions

The white ammonium metavanadate was formed with a pH value of 5 to 7. Vanadium had a high recovery at optimized pH. The effect of time on the vanadium recovery was examined, and it was found that the vanadium recovery rate does not change with increasing precipitation time. The time parameter had only a slight influence on the recovery rate of impurities in the leach solution. Since our goal is to maximize the vanadium recovery in the leach solution and minimize the recovery of impurities, we consider the shortest precipitation time of 2 hours. The vanadium concentration in the leach solution plays an effective role in the formation of precipitates. If the vanadium concentration in the leach solution is less than 1000 mg L⁻¹, we have to use more concentrated ammonium chloride (12% (w/v)) to achieve a vanadium recovery of over 90%. The higher the vanadium concentration in the leach solution than 1000 mg L⁻¹, the lower the concentration of ammonium chloride (4% (w/v)) must be used to achieve a vanadium recovery

above 90%. The ammonium chloride concentration plays the most important role in the vanadium precipitation. A high concentration of ammonium chloride leads to an increase in the recovery rate of vanadium. The optimal concentration of ammonium chloride for vanadium precipitation depends on the vanadium concentration in the leach solution. At high vanadium concentrations, a low concentration of ammonium chloride can lead to a high vanadium recovery. Concentrated ammonium chloride leads to a high recovery of vanadium at low vanadium concentrations.

5. Acknowledgements

The authors would like to acknowledge all those who aided in this work, and the nuclear science and technology research institute in Tehran for financial and technical supports.

6. Competing interests

The authors declare that they have no competing interests.

7. References

- [1] Z. Wang, S. Zheng, S. Wang, L.I.U. Biao, D. Wang, D.U. Hao, Y. Zhang, Research and prospect on extraction of vanadium from vanadium slag by liquid oxidation technologies, *Trans. Nonferrous Met. Soc. China*, 24 (2014) 1273–1288. [https://doi.org/10.1016/S1003-6326\(14\)63189-7](https://doi.org/10.1016/S1003-6326(14)63189-7)
- [2] R. Ahmadi, B. Sheykhi, Recovery of vanadium from secondary tailing of iron ore by salt roasting-alkaline leaching and solvent extraction processes, *Iran. J. Earth Sci.*, 11 (2019) 30-37. <https://doi.org/10.30495/IJES.2019.664778>
- [3] G. Bauer, V. Güther, H. Hess, A. Otto, O. Roidl, H. Roller, S. Sattelberger, S. Köther-Becker, T. Beyer, Vanadium and vanadium compounds, Wiley VCH Verlag GmbH & Co. KGaA, Ullmann's Encyclopedia of Ind. Chem., (2017) 1–22. ISBN: 9783527306732, https://doi.org/10.1002/14356007.a27_367.pub2
- [4] E. F. Baroch, U. Staff, Vanadium and vanadium alloys, *Kirk Othmer Encyclopedia of Chemical Technology* (2000) 1–18. <https://doi.org/10.1002/0471238961.22011401.a01.pub2>
- [5] P. Cao, W.W. Meng, L. Lei, Y. Peng, Effects of impurity on vanadium precipitation, *Adv. Mat. Res.*, 634 (2013) 3128–3133. <https://doi.org/10.4028/www.scientific.net/AMR.634-638.3128>
- [6] Y.M. Zhang, S.X. Bao, T. Liu, T.J. Chen, J. Huang, The technology of extracting vanadium from stone coal in China: history, current status and future prospects, *Hydrometallurgy*, 109(2011)116–124. <https://doi.org/10.1016/j.hydromet.2011.06.002>
- [7] H. Liu, Y.M. Zhang, J. Huang, T. Liu, N.N. Xue, Q.H. Shi, Optimization of vanadium (IV) extraction from stone coal leaching solution by emulsion liquid membrane using response surface methodology, *Chem. Eng. Res. Des.*, 123 (2017) 111-119. <https://doi.org/10.1016/j.cherd.2017.05.001>
- [8] M. Wang, X. Wang, P. Ye, Recovery of vanadium from the precipitate obtained by purifying the wash water formed in refining crude TiCl₄, *Hydrometallurgy*, 110 (2011) 40–43. <https://doi.org/10.1016/j.hydromet.2011.08.005>
- [9] R. Navarro, J. Guzman, I. Saucedo, J. Revilla, E. Guibal, Vanadium recovery from oil fly ash by leaching, precipitation and solvent extraction processes, *Waste Manage.*, 27 (2007) 425–438. <https://doi.org/10.1016/j.wasman.2006.02.002>
- [10] D. He, Q. Feng, G. Zhang, L. Ou, Y. Lu, An environmentally-friendly technology of vanadium extraction from stone coal, *Miner. Eng.*, 20 (2007) 1184–1186. <https://doi.org/10.1016/j.mineng.2007.04.017>
- [11] E. Romanovskaia, V. Romanovski, W. Kwapinski, I. Kurilo, Selective recovery of vanadium pentoxide from spent catalysts of sulfuric acid production: Sustainable approach, *Hydrometallurgy*, 200 (2021)105568. <https://doi.org/10.1016/j.hydromet.2021.105568>
- [12] H. Peng, A literature review on leaching and recovery of vanadium, *J. Environ. Chem. Eng.*, 7 (2019)103313. <https://doi.org/10.1016/j.jece.2019.103313>
- [13] Wang, M.; Cheng, Q.; Qi, J.Y.; Li, J.; Ning, X.X.; Jin, J.P. Process of vanadium extraction from stone coal vanadium ore by sulfuric acid low temperature curing and column leaching, *Min. Metall.*, 29(2020)62–67. <https://doi.org/10.3969/j.issn.1005-7854.2020.03.013>
- [14] V. Zeng, C.H. Yong-Cheng, A literature review of the recovery of molybdenum and vanadium from spent hydro desulphurisation catalysts, Part II: Separation and purification, *Hydrometallurgy*, 98(2009) 10–20. <https://doi.org/10.1016/j.hydromet.2009.03.012>
- [15] Z. Zhao, M. Guo, M. Zhang, Extraction of molybdenum and vanadium from the spent diesel exhaust catalyst by ammonia leaching method, *J. Hazard. Mater.*, 286 (2015) 402–409. <https://doi.org/10.1016/j.jhazmat.2014.12.063>



Determination of manganese in rat blood samples based on ionic liquid-liquid extraction and chelation therapy for evaluation of manganese toxicity in rats

S. Jamilaldin Fatemi^{a,*}, Tayyebeh Zandevakili^a, Fatemeh Khajooe Nejad^a, Marziyeh Iranmanesh^b and Mohammad Faghihi Zarandi^c

^a Department of Chemistry, Shahid Bahonar University of Kerman, Kerman, Iran

^b Department of Chemistry, Kerman Branch, Islamic Azad University, Kerman, Iran

^c Department of Foreign Languages, Shahid Bahonar University of Kerman, Kerman, Iran

ARTICLE INFO:

Received 22 Aug 2021

Revised form 28 Oct 2021

Accepted 23 Nov 2021

Available online 28 Dec 2021

Keywords:

Chelators,
Red blood cells,
Toxicity,
Ionic liquid-liquid extraction,
Flame atomic absorption spectrometry

ABSTRACT

In this study, the manganese ions were extracted in the blood of rats based on desferrioxamine (DFO), deferasirox (DFX) and deferiprone (DFP) as chelators (ligands) by ionic liquid-liquid phase extraction method (ILLEM) before being determined by F-AAS. Also, the toxic effects of manganese on blood serum and hematology parameters such as: RBC, WBC, HGB, PLT and HCT were investigated. Male Wistar rats were randomly divided into control and toxic groups. Manganese chloride was administrated orally in low and high doses. Orally (deferasirox and deferiprone) or intraperitoneally (desferrioxamine) for 2 weeks. Results showed that exposure to manganese significantly increased both counts of hematology parameters and concentration of this metal ion in serum compared to the control group. By procedure, manganese was chelated with ligands in the blood of rats and then the hydrophobic ionic liquid (IL, [HMIM][PF₆]) was added to blood samples. After shaking and centrifuging, the upper liquid phase was separated by an auto-sampler and manganese loaded in a mixture of IL/ligand was settled down in the bottom of the conical tube. The manganese ions were back-extracted from IL phase and the remained acid solution was determined with F-AAS. The linear range, LOD and enrichment factor for 10 mL of blood rats were obtained 25- 180 $\mu\text{g L}^{-1}$, 6.5 $\mu\text{g L}^{-1}$ and 19.92, respectively. By chelation therapy extra manganese ions were removed from human serum and the normal hematology parameters were achieved.

1. Introduction

Trace elements like manganese are essential for normal development and body function across the life span, and are widely distributed in the tissues. Manganese is required for normal amino acid, lipid, protein, and carbohydrate metabolisms. Enzyme families that are Mn-dependent include

oxidoreductases, transferases, hydrolases, lyases, isomerases, and ligases. A manganese deficiency causes improper organism function, but toxicity results if Mn is present in excessive amounts [1,2]. Concentrations of metal in erythrocytes may be a good indicator of tissue accumulation since red blood cells account for about 60–80% of the metal found in whole blood [3-5]. Manganese leaving the enterocyte and entering the circulation bound to transferrin, may bind to transferrin receptors on erythroid cells. The erythroid cell

*Corresponding Author: S. Jamilaldin Fatemi

Email: fatemijam@uk.ac.ir

<https://doi.org/10.24200/amecj.v4.i04.160>

potentially may incorporate manganese into the porphyrin ring in place of iron, therefore producing a manganese protoporphyrin instead of haem [6]. Mn is known to be transported by the transferrin receptor (TfR) and/or divalent metal transporter (DMT1) [7]. Both transporters have been identified in the RBC. Whole blood, serum and plasma manganese are the readily available biomarkers of manganese status in humans. The strength of the observed correlation between blood manganese concentrations and manganese exposure concentrations often depends on the magnitude and duration of exposure. In some studies, whole blood manganese concentrations correlate positively with exposure to manganese [8]. In other cases, blood manganese concentrations in exposed workers remain in the normal adult range (4–14 $\mu\text{g L}^{-1}$), and urine and hair manganese concentrations do not differ between exposed and non-exposed workers [9]. In severe cases of Mn poisoning, chelation therapy has been recommended in order to reduce the body burden of Mn. Chelation therapy that could be carried out as a single and/or combined therapy involves the use of chelating drugs that bind metal for the treatment of potentially fatal conditions [10,11]. In this investigation, we studied the effect of MnCl_2 exposure in low and high doses on blood serum and hematology parameters in male Wistar rats. Deferasirox (4-[3,5-bis (2- hydroxyphenyl)-1,2,4-triazol-1-yl]-benzoic acid, or ICL670) is a tridentate chelator and was first reported by Heinz et al [12]. Deferiprone (1,2-dimethyl-3-hydroxypyrid-4-one) is a bidentate chelator that was used in the detoxification of metals and desferrioxamine (*N*-{5-[acetyl(hydroxy) amino]pentyl}-*N*-[5-(4-[(5-aminopentyl)(hydroxy)amino]-4-oxobutanoyl)-amino]pentyl]-*N*-hydroxysuccinamide) is a hexadentate chelator. Manganese (Mn) used in human body. Manganese ions enter to human body from waters/ foods (rice, apple, wheat, beans, lettuce) and cause the different diseases. [13]. The high values of manganese exist in spinach and tea leaves in ranges of 10–100 mg kg^{-1} [14]. The manganese values in water has found less than 100 $\mu\text{g L}^{-1}$ at pH

7 and the oxidized forms archived in low pH [15,16]. Normal values of manganese in blood samples have found from 1 to 14.5 $\mu\text{g L}^{-1}$ [17]. The extra dosage of manganese has toxicity effect and caused to many diseases such as, memory impairment, dysfunction on liver, renal and CNS. So, manganese in various source such as water and blood samples must be measured by analytical procedures. As toxicity effect of manganese, it is caused to increase the neutrophil count cells and decrease the red blood cells. So, the various analytical techniques such as, flame atomic absorption spectrometry [18], cation exchange chromatography—sector field inductively coupled plasma mass spectrometry [19], the inductively coupled plasma mass spectrometry-MS [20] was used for determining of manganese in biological samples. Also, due to the trace concentration of manganese, and difficulty matrixes, the sample treatment used before sample analysis. Many sample treatments such as, the liquid-liquid extraction [21], the deep eutectic solvent extraction [22], the column graphene oxide-based solid phase extraction [23] were used for manganese extraction in blood samples.

In this research, manganese ions were extracted in blood of rats based on DFO, DFX and DFP chelators by IL-LEM procedure and the manganese concentration in rat blood samples was determined by the F-AAS. Also, the toxic effects of manganese on blood serum and hematology parameters such as: RBC, WBC, HGB, PLT and HCT were investigated.

2. Experimental

2.1. Rats preparation

The Ethics Committee at Medical Sciences, The University of Kerman, approved the research protocol. Male Wistar rats were purchased from Kerman Neuroscience Research Center, Kerman, Iran. At the time of use the rats were 7–8 weeks old, weighing $245 \pm 4\text{g}$ (mean \pm SEM.). All animals were housed in well-cleaned sterilized cages maintained in a room under controlled conditions of temperature ($23 \pm 2^\circ\text{C}$) and illumination (12-h light; 12-h darkness; darkness: 7 p.m. – 7 a.m.) and had free access to a standard diet and water.

2.2. Reagents

The desferrioxamine (DFO, CAS N.: 138-14-7), deferasirox (DFX, CAS N.: 201530-41-8) and deferiprone (DFP, CAS N.: 30652-11-0) as chelating agents (ligands) were purchased from Sigma Aldrich, Germany. 1-Hexyl-3-methylimidazolium hexafluorophosphate (IL, 97.0% HPLC grade; CAS N.: 304680-35-1) was prepared from Sigma Aldrich, Germany. Other materials were prepared from Merck Chemical Co. (Darmstadt, Germany). The standard solution for manganese were prepared by dissolving of 1.0 g of $Mn(NO_3)_2$ in deionized water (DW, 1 L). The working standard solutions for calibration of manganese were daily prepared by diluting of standard solutions (1000 mg L^{-1}) with DW (Millipore, USA). All the glass and tubes were cleaned by %10 nitric acid (v/v) for two days and then washed by DW. The standard reference materials (1640a; SRM) for manganese in water ($40.39 \pm 0.36\ \mu\text{g L}^{-1}$) was used.

2.3. Instrumental

Flame atomic absorption spectrometer with a double beam accessory (F-AAS, GBC 906, Aus.) based on air-acetylene (C_2H_2), the D_2 and HCL lampas was used. The limits of detection (LOD) and linear range was achieved 0.16 mg L^{-1} and $0.5\text{-}3.6\text{ mg L}^{-1}$, respectively by the FAAS. The HCL light of manganese was optimized by two screws (Hor. S and Ver. S) and the wavelength of 279.5 nm (slit of 0.2 nm ; 5 mA) was selected for

F-AAS. After sample treatment, 1 mL of water and blood samples were injected to burner of FAAS by the auto-sampler. The working range for F-AAS was obtained $0.2\text{-}3.8\text{ mg L}^{-1}$. The validation of results was obtained by the graphite furnace atomic absorption spectrophotometer (GF-AAS, GBC, Aus.) for manganese analysis in blood samples. The pH of the samples was measured by Omega pH meter (USA). The shaker (Grant, U.K) and centrifuge (speed $3000\text{-}5000\text{ rpm}$ x g, Germany) was used for extraction/separation of manganese from blood samples.

2.4. Chelation therapy design

In this study, manganese chloride [$MnCl_2$ (LD50: 1715 mg kg^{-1})] at two doses of 30 mg kg^{-1} body weight (low dose) and 60 mg kg^{-1} body weight (high dose) was given to the drinking groups for 3 months followed by an early administration of chelating agent. Study population consisted of 95 rats that were housed in groups of five per cage. We assigned them randomly to control (5 rats) and treated groups [high dose (45 rats) and low dose (45 rats)]. After 90 days, chelation therapy was carried out after Mn application. Treated animals were classified as follows (Table 1): before chelation therapy (5 rats), without chelation therapy [vehicle oral (5 rats) and intraperitoneally (5 rats)], single therapy (15 rats) and combined therapy (15 rats) for both low and high doses. Chelators were given orally (DFX and DFP) and intraperitoneally (DFO) as single and combined therapies. Doses of DFX,

Table 1. Classification of rat animals for further analysis

Treated groups (90):	Before chelation therapy	
	Without chelation therapy (Vehicle)	Vehicle oral Vehicle intraperitoneally
	Single therapy	DFX (30 mg kg^{-1} body weight) DFO (30 mg kg^{-1} body weight) L1 (60 mg kg^{-1} body weight)
	Combined therapy	DFX (15 mg kg^{-1} body weight)+DFO (15 mg kg^{-1} body weight) DFX (15 mg kg^{-1} body weight)+L1 (30 mg kg^{-1} body weight) DFO (15 mg kg^{-1} body weight)+L1 (30 mg kg^{-1} body weight)

DFP and DFO were 30, 60 and 30 mg kg⁻¹ body weight, respectively (Table 1). Chelators were given immediately after Mn application during 2 weeks. After chelation therapy, rats were sacrificed by exsanguinations from abdominal aorta and their blood was collected for analysis.

2.5. Sample collection and analysis procedure

The full blood count sample was collected into a citrate tube (Tek Lab, Catalogue No. K-100LS). Hematology parameters such as RBC (10⁶/l), WBC (10³ L⁻¹), HGB (g dL⁻¹), PLT (10³ L⁻¹) and HCT (%) were measured in whole blood by counting device (fluorescent flow cytometry technology (Sysmex KX-21N) in hematology lab.

By the IL-LEM procedure, the DFO, DFX and DFP chelators mixed with IL and used for speciation and extraction of Mn ions in rat blood samples (Fig.1). The chelators dispersed in 10 mL of standard manganese solution (25- 180 µg L⁻¹) and rat blood samples, after chelation and extraction Mn ions, the hydrophobic ionic liquid ([HMIM] [PF6]; 100 mg) was added to samples and diluted with acetone. In fact, the Mn ions was extracted by coordination

bond of nitrogen at optimized pH (98%), but at higher pH, manganese ions precipitated (Mn(OH)₂). The manganese chelated with the DFO, DFX and DFP chelators and separated from samples by hydrophobic ionic liquid ([HMIM] [PF6]) in end of conical tube after centrifuging for 5 min at 3500 rpm. After removing upper blood/serum phase, manganese ions were back-extracted from the DFO/IL, DFX/IL and DFP/IL into aqueous phase with 0.3 mL of HNO₃ solutions (0.2M). Finally, the resulting solution was determined by F-AAS after dilution with DW up to 0.5 mL. The linear range for manganese was 25- 180 µg L⁻¹ or 0.025-0.18 mg L⁻¹ by the IL-LEM procedure.

2.6. Statistical analysis

The statistical package for the sciences (SPSS, Bristol, England) version 18 was used to process the data. All comparisons among the groups were analyzed with a one-way analysis of variance (ANOVA) followed by LSD test for multiple comparisons. Data were reported as the mean±SEM. In all comparisons, p<0.05 was the criterion for statistical significance.

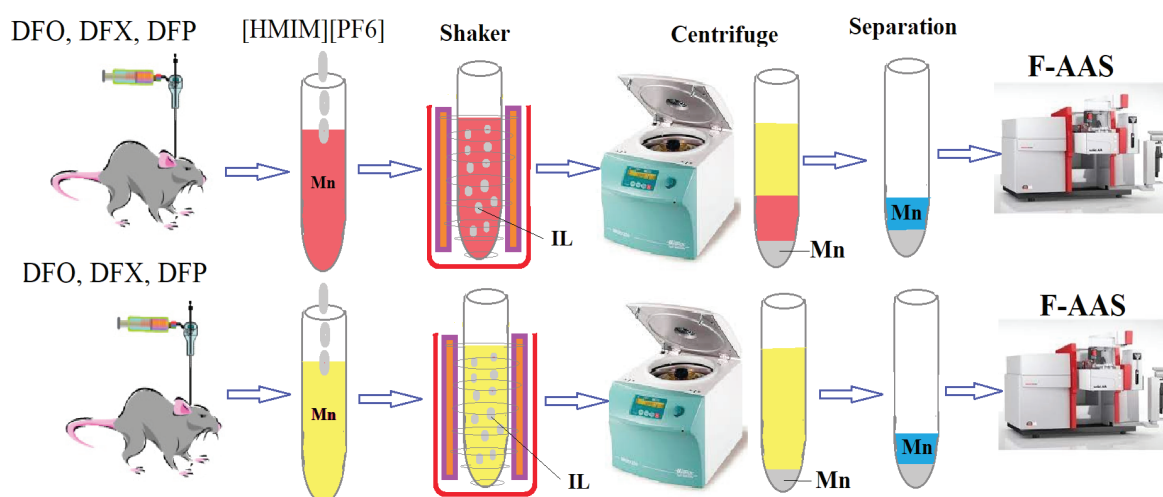


Fig.1. Determination of manganese in the rat blood/serum based on chelators by the IL-LEM procedure coupled to F-AAS

Table 2. Bodyweights over 90 days for rats in different groups (all data are expressed as the mean±SEM)

Group	Control	Low dose drinking of manganese	High dose drinking of manganese
Initial body weight (g)	242.21 ± 8.62	249.80 ± 2.91	244.61 ± 4.20
Final body Weight (g)	297.20 ± 7.46	299.60 ± 4.55	286.61 ± 7.95

3. Results and Discussion

3.1. Symptoms

Over 90 days, results indicated that difference weight between initial and final body weight, decreased in both the high and low doses groups compared to the control group (Table 2). Furthermore, toxicity symptoms such as: skin reaction, black spots on liver and bright lung appeared.

3.2. Hematology parameters

The hematology parameters are shown in Table 3 and 4. Compared to each respective control group, a significant enhance in HGB count was observed in both low and high doses groups. The RBC, WBC, PLT and HCT counts enhanced significantly in the high dose group (Table 3 and 4, Fig. 2). In order to investigate the effect of passing time in removing

Mn from the body spontaneously, one group was treated as without chelation therapy (vehicle). Since there were no significant differences between the vehicle and before chelation therapy groups, results of chelation therapy were compared to each respective vehicle group. After chelation therapy, the RBC count significantly reduced by DFO+DFX in low dose group and DFO in high dose group. The HGB count significantly reduced by DFX, DFP(L1) and DFO+DFX in low dose group and DFO, DFP (L1), DFX, DFO+DFP (L1), DFO+DFX and DFX+DFP(L1) in high dose group. The PLT count by DFO and DFX+DFP(L1), also HCT count by DFO and DFO+DFP (L1) significantly reduced in high dose group (Table 3 and 4, Fig. 3). (The level of significance in all tests was set as $p < 0.05$)

Table 3. Hematology parameters in low-dose groups (all data are expressed as the mean±SEM)

Group	Control	Before chelation therapy	Vehicle	Chelation therapy DFX	Chelation therapy DFP (L1)	Chelation therapy DFO	Chelation therapy DFO+DFP (L1)	Chelation therapy DFX+DFO	Chelation therapy DFX+DFP (L1)
RBC ($10^6 L^{-1}$)	7.24±0.25	7.28±0.11	7.91±0.39	7.58±0.33	7.28±0.42	7.75±0.11	7.88±0.14	6.98±0.57	7.63±0.16
WBC ($10^3 L^{-1}$)	7.42±0.43	8.60±1.94	9.79±1.94	9.94±0.59	11.10±1.14	9.80±0.84	9.80±1.64	12.25±1.22	8.04±0.83
HGB (g dL ⁻¹)	11.96±0.29	13.02±0.75	12.75±0.38	11.54±0.89	11.35±0.03	12.77±0.14	12.15±0.43	10.80±2.18	12.18±0.33
PLT ($10^3 L^{-1}$)	501.79±45.53	680.02±47.69	663.20±45.28	782.00±37.83	828.00±60.44	654.20±69.69	691.40±48.52	579.40±153.65	658.80±71.39
HCT (%)	39.02±1.21	37.39±0.20	38.62±1.16	37.70±1.55	37.62±1.72	41.00±0.26	38.96±0.67	35.68±2.73	39.42±0.59
Mn concentration (mg L ⁻¹)	1.28±0.10	1.95±0.15	1.79±0.22	1.32±0.14	1.08±0.12	1.01±0.15	1.02±0.20	1.34±0.17	1.19±0.07

ANOVA analysis shows p value in all of treatment groups in comparison to vehicle

Table 4. Hematology parameters in high-dose groups (all data are expressed as the mean±SEM).

Group	Control	Before chelation therapy	Vehicle	Chelation therapy DFX	Chelation therapy L1(DFP)	Chelation therapy DFO	Chelation therapy DFO+(DFP) L1	Chelation therapy DFX+DFO	Chelation therapy DFX+L1
RBC ($10^6 L^{-1}$)	7.24±0.25	8.04±0.12	8.30±0.83	8.08±0.15	7.92±0.70	7.30±0.21	7.87±0.30	7.74±0.18	8.41±0.18
WBC ($10^3 L^{-1}$)	7.42±0.43	11.22±1.44	10.74±1.13	10.76±1.40	15.28±2.40	11.56±1.38	9.42±1.02	11.32±1.08	8.74±1.41
HGB (g dL ⁻¹)	11.96±0.29	14.27±0.22	13.80±0.22	12.34±0.39	12.68±0.20	11.50±0.46	12.38±0.29	12.17±0.32	12.84±0.29
PLT ($10^3 L^{-1}$)	501.79±145.53	824.00±48.12	806.75±42.74	630.25±56.54	800.40±46.70	623.00±68.40	806.00±67.66	723.66±42.03	594.25±140.02
HCT (%)	39.02±1.21	40.30±0.58	40.95±0.88	42.85±0.70	40.86±0.59	38.08±1.10	38.95±0.67	39.70±0.63	42.60±0.96
Mn concentration (mg L ⁻¹)	1.28±0.10	2.03±0.26	1.32±0.14	1.32±0.14	1.42±0.05	1.14±0.16	1.23±0.14	1.28±0.21	1.18±0.09

ANOVA analysis shows p value in all of treatment groups in comparison to vehicl

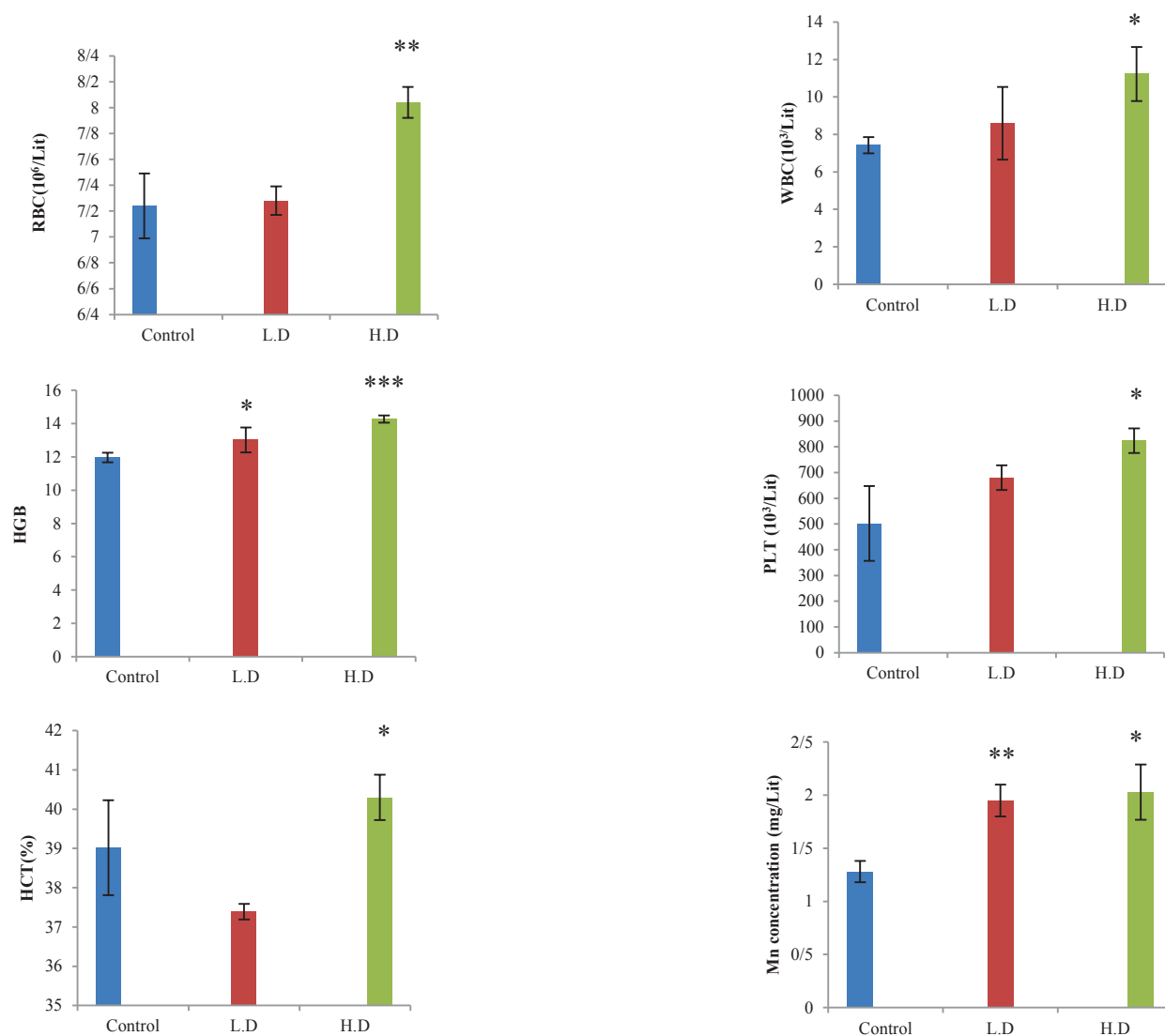


Fig. 2. Hematology parameters and Mn concentrations in control, high and low doses of Mn administration (Before chelation therapy), * $p < 0.05$, ** $p < 0.01$, *** $p < 0.001$ as compared to control.

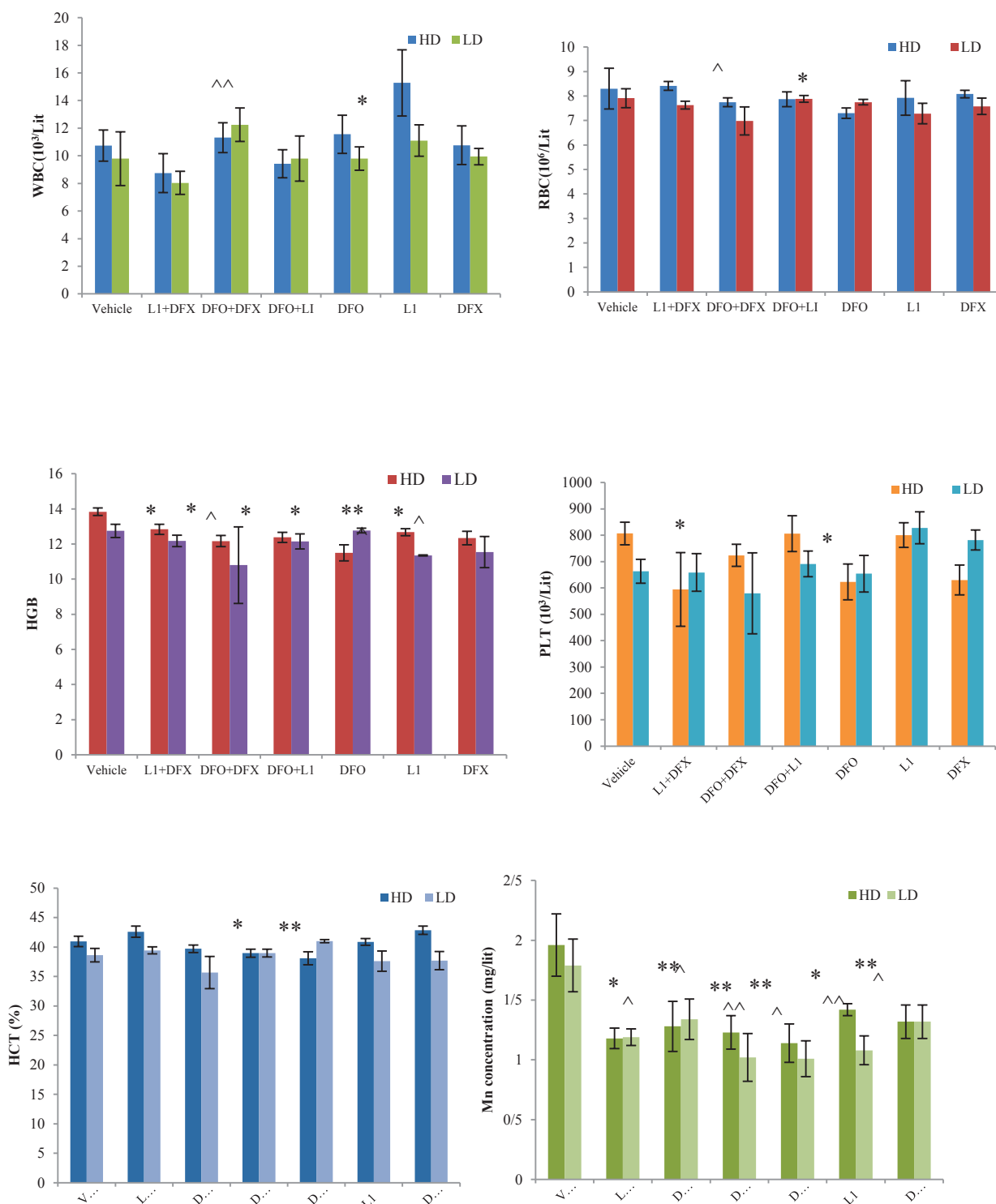


Fig. 3. Hematology parameters and concentrations of Mn in Vehicle and treated groups after chelation therapy, * $p < 0.05$, ** $p < 0.01$, *** $p < 0.001$ significantly different from HD vehicle and ^ $p < 0.05$, ^^ $p < 0.01$, ^^ $p < 0.001$ significantly different from LD vehicle, by one-way ANOVA followed by LSD's multiple comparison test

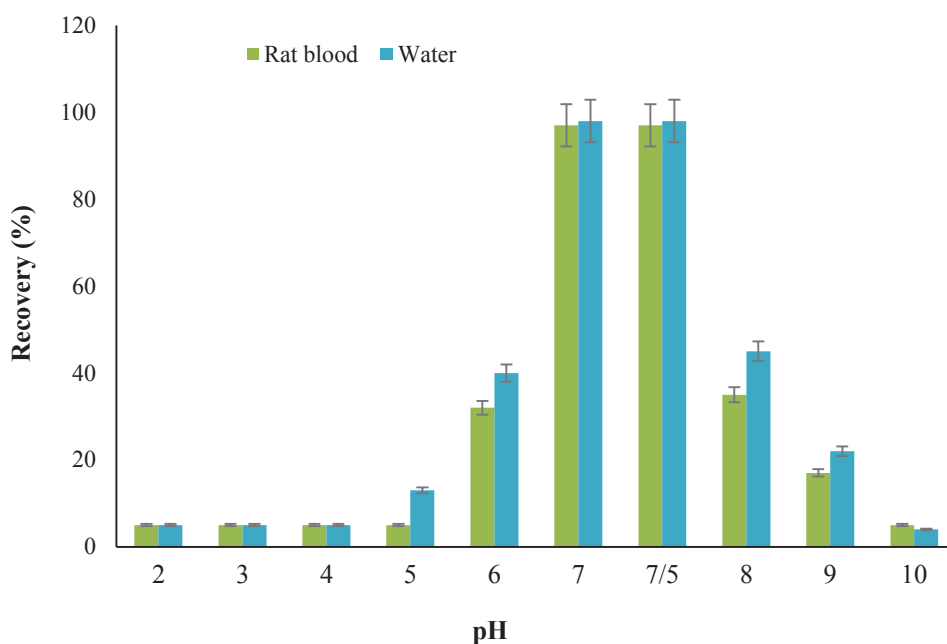


Fig.4. The effect of pH on manganese extraction by IL-LE method

3.3. Mn concentration

Administration of manganese chloride in both of low and high doses groups caused a significant increase in concentration of Mn (Table 3 and 4, Fig. 2). After chelation therapy, all chelators significantly decreased the level of Mn in both low and high doses groups. Although DFO was more effective chelator (Table 3 and 4, Fig. 3)

3.4. Optimization of extraction parameters

For efficient extraction for manganese in blood samples, the effect of parameters such as the amount of ligand, the pH, the Ionic liquids, the shaking and centrifuging time, the sample volume and the interferences ions were studied and optimized.

3.4.1. pH effect

The effect of pH on extraction of manganese in water and rat blood samples must be optimized. The pH effect on the manganese complexation by the DFO, DFX and DFP chelators. So, the various pH between 2 - 11 was evaluated for the Mn extraction in rat blood samples. The pH was

controlled by a buffer solution. The result showed, the high recovery based on chelators for manganese value between 25-180 $\mu\text{g L}^{-1}$ was obtained at pH of 7. The recoveries were decreased for Mn at pH ranges less than 7 and more than 8.0. So, the pH of 7.0-7.5 were selected for extraction of manganese in waters and rat blood samples by the IL-LEM procedure (Fig. 4).

3.4.2. Optimization of DFO, DFX and DFP chelators

The concentration of chelators is main parameters for manganese extraction which must be optimized by the IL-LE procedure. For optimizing, 0.1×10^{-6} – 0.9×10^{-6} mol L^{-1} of DFO was used in the rat blood sample. The results showed that, by increasing ligand concentration up to 0.6×10^{-6} mol L^{-1} , the recoveries are also increased (Fig. 5). So, the amount of chelating agent (DFO) between 0.6-0.9 $\mu\text{mol L}^{-1}$ had high recovery and 0.7 $\mu\text{mol L}^{-1}$ was found the best amount for Mn extraction. The DFX and DFP have almost used with the similar range between 0.6-0.9 $\mu\text{mol L}^{-1}$.

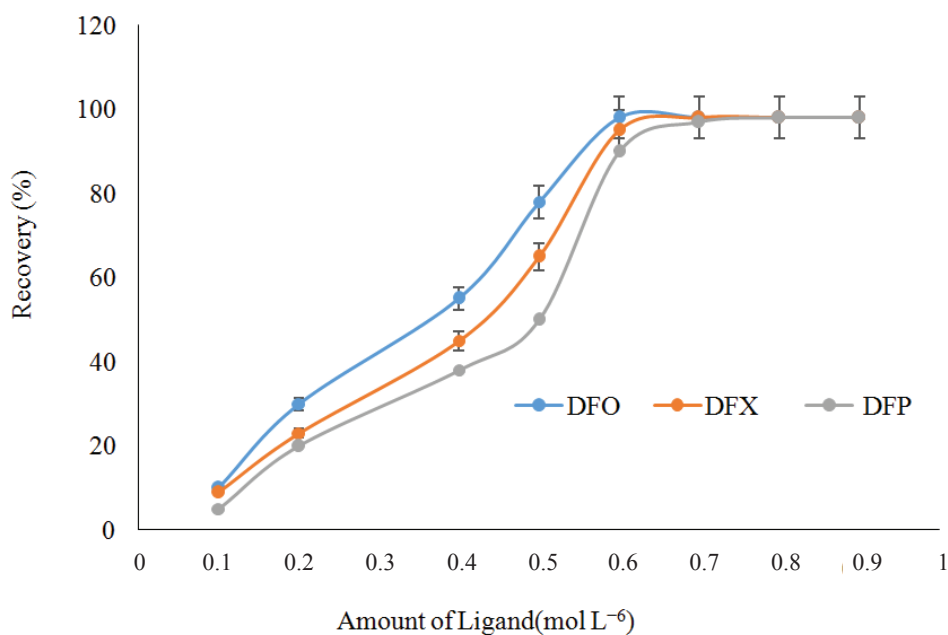


Fig. 5. The effect of ligand on manganese extraction by IL-LE method

3.4.3. Optimization of sample volume and eluent

The sample volume of rat blood samples and the standard solution was evaluated from 1.0 mL to 25 mL for Mn concentration between 25-180 $\mu\text{g L}^{-1}$. The results showed us the efficient extraction was obtained for 10 mL of rat blood samples at pH 7-7.5 (Fig. 6). In-addition, the effect of eluent on manganese extraction based on ligand/IL (DFO,

DFX and DFP/IL) were evaluated. At low pH, the covalent bond between the manganese and nitrogen group was break-down and released the Mn ions into acid phase. So, the acid solutions (HCl, HNO₃, H₂SO₄) were used for back-extraction process in blood and water samples. The results showed, the efficient extraction was obtained by HNO₃ (0.2 M, 0.3 mL) (Fig. 7).

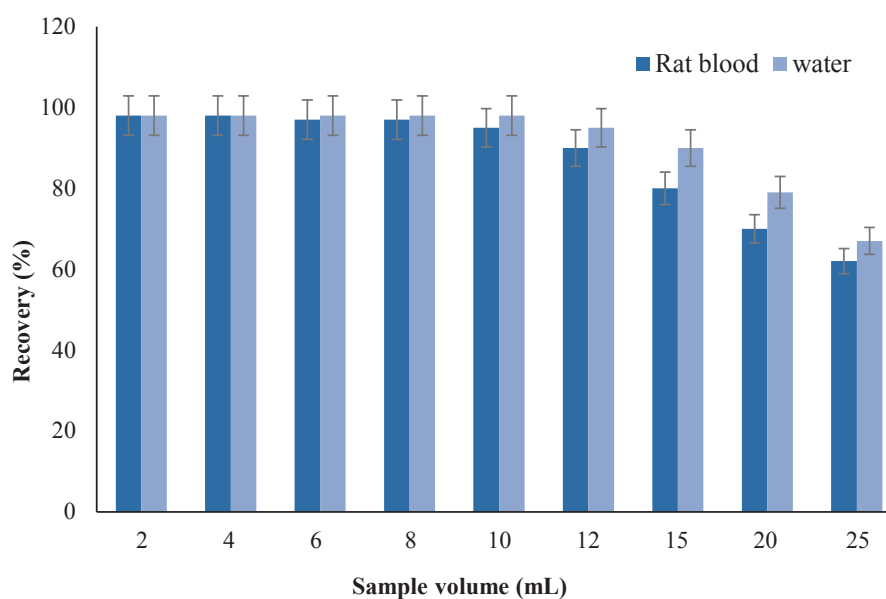


Fig. 6. The effect of sample volume on manganese extraction by IL-LE method

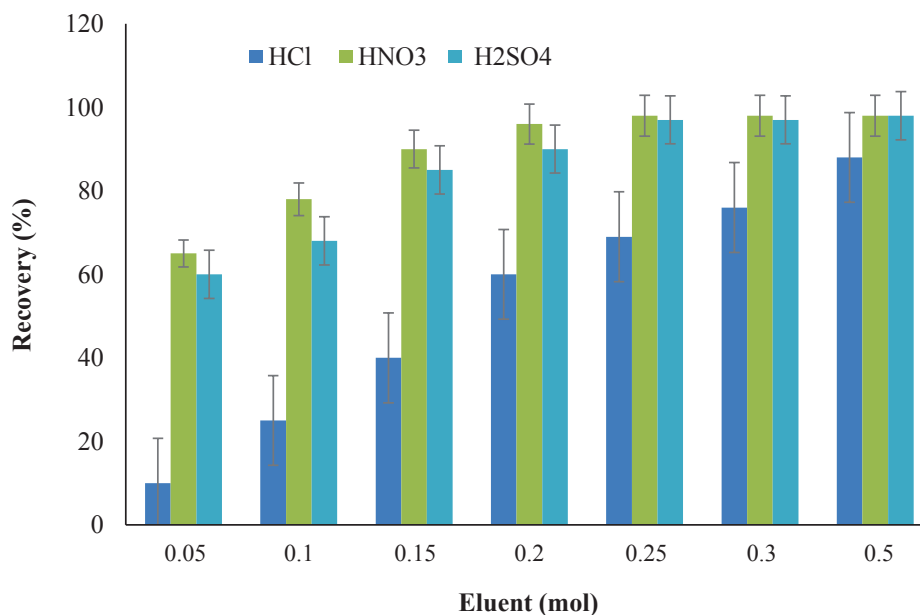


Fig. 7. The effect of eluents on manganese extraction by IL-LE method

3.5. Discussion of Manganese toxicity

By procedure, the manganese extracted based on ligand and IL in rat blood samples before determined by the F-AAS. Also, the toxicity of manganese in rat evaluated by chelation therapy with DFO, DFX and DFP before determined by the IL-LE procedure at pH=7-7.5. Due to biologically evaluation, manganese is considered to be an essential metal important to mitochondrial oxidative processes for all living mammals, but may also be toxic at high concentrations [24]. Manganese toxicity seems to be largely due to Mn induced cellular free radical damage [25]. This hypothesis is based on the potent redox properties of Mn. In our current study uptake of manganese after oral exposure led to elevating RBC, WBC, HGB, PLT and HCT. Furthermore, we observed a clear increase in level of Mn in blood serum as compared to control. According the previous study, Mn in the blood compartment may tend to accumulate in the blood cells [26]. RBC count had a significant positive relationship with whole blood manganese [6]. Hemoglobin is a protein containing iron in red blood cells. One red blood cell contains 280 million molecules of hemoglobin. Exposure to Mn during the toxicity period, results increase in both counts of RBC and HGB in whole

blood. Manganese leaving the enterocyte and entering the circulation bound to transferrin, may bind to transferrin receptors on erythroid cells. The erythroid cell potentially may incorporate manganese into the porphyrin ring in place of iron, therefore producing a manganese proto-porphyrin instead of hemoglobin [6]. Subsequently, the amount of deformed hemoglobin increases. Hematocrite is the percentage of red blood cells. Therefore, after toxicity with Mn, its behavior is similar red blood cells. The platelet is responsible for blood coagulation. Interestingly, Mn toxicity increase platelet and the immune system become more active by increasing white blood cell counts. A simple measurement of extracellular Mn such as in serum or plasma may not accurately reflect Mn concentrations in the blood compartment, including blood cells, so whole blood must be analyzed [26]. However, Serum levels of metal are questioned as valid markers of total-body of metal. In any event, our results indicate that Mn can accumulate in serum. In severe case of manganese poisoning, chelation therapy has been recommended in order to reduce the body burden of manganese. Deferasirox, deferipron and desferrioxamine are commonly used chelating agent for treatment of a variety of metal-induced

toxicities [27, 28], especially treatment of iron. In our previous studies, it has been shown these chelators increase toxin elimination and reducing the body burden of manganese [29, 30]. Also current our study supports the clinical effectiveness of these chelators. Results show that the above chelators are able to return Mn and hematology parameters to nearly normal level of control group. On the other hand, they can determine/separate/extraction of Mn ions in rat blood samples with high accuracy and precision by F-AAS. The results showed, the DFO as single and combined with DFX and L1 is more effective for extraction of manganese ions. Surprisingly after chelation therapy by combination of DFX and DFO count of WBC increased. There is no satisfactory explanation for this result. However, it is reasonable to postulate that the immune system against the drug increases the white blood cell count.

3.6. Validation of extraction procedure

By the ILLE procedure, the separation and determination of Mn ions in rat blood samples

were achieved at pH from 7.0 to 7.5. In the real samples such as, water, rat blood and rat serum, the result of manganese were validated by spiking to standard solutions of manganese (10, 20, 40, 60 $\mu\text{g L}^{-1}$) at optimized conditions (Table 5). The results showed us, the efficient extraction for manganese was carried out in real samples based on mixture of DFX, DFO, L1 and [HMIM][PF6] before shaking and centrifuging process. Finally after extraction and back-extraction of Mn ions, the remained solution was determined by F-AAS by dilution of DW up to 0.5 mL.

4. Conclusions

In summary, the speciation and determination of Mn ions in rat blood samples were achieved by the ILLE procedure at pH from 7.0 to 7.5. The three chelators, DFX, DFO and L1 used as chelation therapy in rats, then the [HMIM][PF6] added to blood of rats. After shaking, extraction, centrifuging and back-extraction, the Mn values were determined by F-AAS. The linear range and LOD was obtained 25- 180 $\mu\text{g L}^{-1}$ and 6.5 $\mu\text{g L}^{-1}$, respectively. Also,

Table 5. Validation of ILLEM for determination of manganese ions in water, whole blood, serum and plasma of rat based on ligand/IL by spiking of real samples ($\mu\text{g L}^{-1}$; n=8)

Samples	Added	*Found Mn	*Final concentration Mn Dilution factor 20	Recovery (%)
Whole blood of rat	-----	76.54 ± 1.11	530.80 ± 25.51	-----
	20	45.83 ± 2.05	916.60 ± 40.42	96.5
	40	68.12 ± 2.88	1362.40 ± 53.72	103.9
Serum of rat	-----	13.68 ± 0.62	273.60 ± 12.76	-----
	10	23.14 ± 1.12	462.80 ± 21.73	94.6
	20	33.52 ± 1.69	670.40 ± 29.82	99.2
Plasma rat	-----	7.68 ± 0.33	153.60 ± 6.54	-----
	5	12.55 ± 0.56	251.00 ± 11.75	97.4
	10	17.97 ± 0.78	359.40 ± 16.43	102.9
Water	-----	23.88 ± 1.12	-----	-----
	20	43.64 ± 1.98	-----	98.8
	40	62.41 ± 2.95	-----	96.3

* $x \pm ts / \sqrt{n}$ at 95% confidence (n=8)

1 mL of Whole blood, Serum and plasma diluted with DW up to 20(1:20)

the results of the current study clearly demonstrated that chronic Mn exposure not only resulted in a marked increase of Mn concentrations in blood serum, but also caused significant enhances count of RBC, WBC, HGB, PLT and HCT in whole blood. Chelation therapy was effective in returning hematology parameters and Mn ions to nearly normal level. As well as three chelators are more efficient as combined therapy than single therapy in removing manganese from tissues. Therefore, after basic preclinical research this could be recommended for human administration.

5. Acknowledgements

The authors wish to thanks from the head and director of Kerman Neuroscience Research Center, Mohammad Faghihi Zarandi as statistical data analyzer, and Shahid Bahonar University of Kerman Faculty Research for Funding and supporting of this research.

6. Declaration of interest

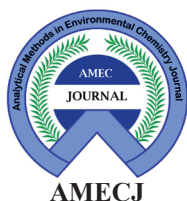
The authors report no conflicts of interest. The authors alone are responsible for the content and writing of this article.

7. References

- [1] L. Li, X. Yang, The essential element manganese, oxidative stress, and metabolic diseases: links and interactions, *Oxid. Med. Cell. Longev.*, 2018 (2018) 7580707. <https://doi.org/10.1155/2018/7580707>
- [2] T.V. Peres, M.R.C. Schettinger, P. Chen, F. Carvalho, D.S. Avila, A.B. Bowman, M. Aschner, Manganese-induced neurotoxicity: a review of its behavioral consequences and neuroprotective strategies, *BMC Pharmacol. Toxicol.*, 17 (2016) 57. <https://doi.org/10.1186/s40360-016-0099-0>.
- [3] N. Reynolds, A. Blumsohn, J.P. Baxter, G. Houston, C.R. Pennington, Manganese requirement and toxicity in patients on home parenteral nutrition, *Clin. Nutr.*, 17 (1998) 227-230. [https://doi.org/10.1016/s0261-5614\(98\)80064-2](https://doi.org/10.1016/s0261-5614(98)80064-2).
- [4] A.C. Pfalzer, A.B. Bowman, Relationships between essential manganese biology and manganese toxicity in neurological disease, *Curr. Environ. Health. Rep.*, 4 (2017) 223-228. <https://doi.org/10.1007/s40572-017-0136-1>.
- [5] S.L. O'Neal, W. Zheng, Manganese toxicity upon overexposure: a decade in review, *Curr. Environ. Health. Rep.*, 2 (2015) 315-328. <https://doi.org/10.1007/s40572-015-0056-x>.
- [6] E.A. Smith, P. Newland, K.G. Bestwick, N. Ahmed, Increased whole blood manganese concentrations observed in children with iron deficiency anaemia, *J. Trace Elem. Med. Biol.*, 27 (2013) 65-69. <https://doi.org/10.1016/j.jtemb.2012.07.002>.
- [7] Y. Shen, X. Li, D. Dong, B. Zhang, Y. Xue, P. Shang, Transferrin receptor 1 in cancer: a new sight for cancer therapy, *Am. j. Cancer. Res.*, 8 (2018) 916-931. <http://www.ncbi.nlm.nih.gov/pmc/articles/pmc6048407/>.
- [8] X. Ge, F. Wang, Y. Zhong, Y. Lv, C. Jiang, Y. Zhou, D. Li, B. Xia, C. Su, H. Cheng, Y. Ma, F. Xiong, Y. Shen, Y. Zou, X. Yang, Manganese in blood cells as an exposure biomarker in manganese-exposed worker's healthy cohort, *J. Trace Elem. Med. Biol.*, 45 (2018) 41-47. <https://doi.org/10.1016/j.jtemb.2017.09.016>.
- [9] M. Aschner, K.M. Erikson, D.C. Dorman, Manganese dosimetry: species differences and implications for neurotoxicity, *Crit. Rev. Toxicol.*, 35 (2005) 1-32. <https://doi.org/10.1080/10408440590905920>.
- [10] S.J. Fatemi, A. Sh. Saljooghi, F. Dahooee, M. Iranmanesh, M. Golbafan, Chelation of cadmium by combining deferasirox and deferiprone in rats, *Toxicol. Ind. Health*, 27 (2011) 371-377. <http://dx.doi.org/10.1177/0748233710388451>.
- [11] S.J. Fatemi, F. Khajooee nejad, T. Zandevakili, F. Dahooee balooch, Chelation of cobalt by combining deferasirox, deferiprone and desferrioxamine in rats, *Toxin. Rev.*, 33 (2014) 146-150. <https://doi.org/10.3109/15569543.2014.911749>.

- [12] U. Heinz, K. Hegetschweiler, P. Acklin, B. Faller, R. Lattmann, H.P. Schnebli, 4-[3,5-Bis(2-hydroxyphenyl)-1,2,4-triazol-1-yl]- benzoic Acid: A novel efficient and selective iron(III) complexing agent, *Angew. Chem. Int. Ed.*, 38 (1999) 2568-2570. [https://doi.org/10.1002/\(SICI\)1521-3773\(19990903\)38:17%3C2568::AID-ANIE2568%3E3.0.CO;2-C](https://doi.org/10.1002/(SICI)1521-3773(19990903)38:17%3C2568::AID-ANIE2568%3E3.0.CO;2-C).
- [13] T.L. Gerke, B.J. Little, J. Barry Maynard, Manganese deposition in drinking water distribution systems, *Sci. Total. Environ.*, 541 (2016) 184-193. <https://doi.org/10.1016/j.scitotenv.2015.09.054>.
- [14] M. Tuzen, A. Elik, B. Hazer, S. Şimşek, N. Altunay, Poly(styrene)-co-2-vinylpyridine copolymer as a novel solid-phase adsorbent for determination of manganese and zinc in foods and vegetables by FAAS, *Food. Chem.*, 333 (2020) 127504. <https://doi.org/10.1016/j.foodchem.2020.127504>.
- [15] M. Yoon, C. Ring, C.B.V. Landingham, M. Suh, G. Song, T. Antonijevic, P.R. Gentry, M.D. Taylor, A.M. Keene, M.E. Andersen, H.J. Clewell, Assessing children's exposure to manganese in drinking water using a PBPK model, *Toxicol. Appl. Pharmacol.*, 380 (2019) 114695. <http://dx.doi.org/10.1016/j.taap.2019.114695>.
- [16] WHO, Manganese in drinking water. Background document for development of WHO guidelines for drinking-water quality. World Health Organization, 2011. www.who.int/water_sanitation_health/dwq/chemicals/manganese.pdf.
- [17] C. Kirk, L. Gemmell, C.A. Lamb, N.P. Thompson, C.G. Mountford, B.J. Toole, Elevated whole-blood manganese levels in adult patients prescribed "manganese-free" home parenteral nutrition, *Nutr. Clin. pract.*, 35 (2020) 1138-1142. <https://doi.org/10.1002/ncp.10431>.
- [18] M. Arain, T. Kazi, H. Afridi, J. Ali, A. Spectroscopy, preconcentration of trace level manganese in blood samples of patients with different neurological disorders using a deep eutectic solvent extraction method prior to analysis by flame atomic absorption spectrometry, *At. Spectrosc.*, 38 (2017) 92-98. <http://dx.doi.org/10.46770/AS.2017.04.003>.
- [19] N. Solovyev, M. Vinceti, P. Grill, J. Mandrioli, B. Michalke, Redox speciation of iron, manganese, and copper in cerebrospinal fluid by strong cation exchange chromatography – sector field inductively coupled plasma mass spectrometry, *Anal. Chim. Acta*, 973 (2017) 25-33. <https://doi.org/10.1016/j.aca.2017.03.040>.
- [20] S. Meyer, M. Markova, G. Pohl, T.A. Marschall, O. Pivovarova, A.F.H. Pfeiffer, T. Schwerdtle, Development, validation and application of an ICP-MS/MS method to quantify minerals and (ultra-) trace elements in human serum, *J. trace. Elem. Med. Biol.*, 49 (2018) 157-163. <https://doi.org/10.1016/j.jtemb.2018.05.012>.
- [21] B. Tışlı, T.U. Gösterişli, B.T. Zaman, E.G. Bakırdere, S. Bakırdere, Determination of manganese in coffee and wastewater using deep eutectic solvent based extraction and flame atomic absorption spectrometry, *Anal. Lett.*, 54 (2021) 979-989. <https://doi.org/10.1080/00032719.2020.1789871>.
- [22] D. Rolle-McFarland, Y. Liu, F. Mostafaei, S. E. Zauber, The association of bone and blood manganese with motor function in Chinese workers, *Neurotoxicol.*, 88 (2022) 224-230. <https://doi.org/10.1016/j.neuro.2021.12.005>.
- [23] M.R. Pourjavid, M. Arabieh, S.R. Yousefi, A. Akbari Sehat, Interference free and fast determination of manganese(II), iron(III) and copper(II) ions in different real samples by flame atomic absorption spectroscopy after column graphene oxide-based solid phase extraction, *Microchem. J.*, 129 (2016) 259-267. <https://doi.org/10.1016/j.microc.2016.07.008>.
- [24] H. Röllin, A. Mathee, J. Levin, P. Theodorou, F. Wewers, Blood manganese concentrations among first-grade schoolchildren in two South African cities, *Environ. res.*, 97 (2005) 93-99. <https://doi.org/10.1016/j.envres.2004.05.003>.

- [25] D. Ganini, J.H. Santos, M.G. Bonini, R.P. Mason, Switch of mitochondrial superoxide dismutase into a prooxidant peroxidase in manganese-deficient cells and mice, *Cell. Chem. Biol.*, 25 (2018) 413-425. e416. <https://doi.org/10.1016/j.chembiol.2018.01.007>.
- [26] Y. Jiang, W. Zheng, L. Long, W. Zhao, X. Li, X. Mo, J. Lu, X. Fu, W. Li, S. Liu, Q. Long, J. Huang, E. Pira, Brain magnetic resonance imaging and manganese concentrations in red blood cells of smelting workers: search for biomarkers of manganese exposure, *Neurotoxicol.*, 28 (2007) 126-135. <https://dx.doi.org/10.1016/j.neuro.2006.08.005>.
- [27] M. Khatamifar, Z. Rashidi Ranjbar, S.J. Fatemi, Preparation of deferasirox in nano-scale by ultrasonic irradiation and optimization the amount and reaction time parameters, *Int. J. Nano. Dimens.*, 6 (2015) 363-369. <https://doi.org/10.7508/ijnd.2015.04.004>.
- [28] N. Partovi, M.R. Ebadzadeh, S.J. Fatemi, M. Khaksari, Antilithiatic effect of aqueous and ethanolic extracts of cactus prickly pear in chemically induced urolithiasis in rats, *Toxin. Rev.*, 37 (2018) 166-170. <https://doi.org/10.1080/15569543.2017.1325906>.
- [29] T. Zandevakili, S.J. Fatemi, V. Sheibani, Chelation of manganese by combining deferasirox, deferiprone and desferrioxamine in male rats as biological model, *Toxin. Rev.*, 34 (2015) 151-156. <https://doi.org/10.3109/15569543.2015.1074924>.
- [30] T. Zandevakili, S.J. Fatemi, M. Shabani, K. Esmaeilpour, V. Sheibani, Evaluating the effects of single and combined chelators therapies on spatial learning and memory impairments in chronic manganese poisoning, *Toxin. Rev.*, 35 (2016) 38-46. <https://doi.org/10.3109/15569543.2016.1141788>.



Synthesis and identification of meta-(4-bromobenzyloxy) benzaldehyde thiosemicarbazone (MBBOTSC) as novel ligand for cadmium extraction by ultrasound assisted-dispersive-ionic liquid-liquid micro extraction method

Abdolreza Hassanzadeh^a, Bagher Amirheidari^b, Ahmad Salarifar^c, Ali Asadipour^a and Yaghoob Pourshojaei^{a*}

^a Department of Medicinal Chemistry, Faculty of Pharmacy, Kerman University of Medical Sciences, Kerman, Iran.

^b Department of Pharmaceutical Biotechnology, Faculty of Pharmacy, Kerman University of Medical Sciences, Kerman, Iran

^c Environmental Engineering, Faculty of Natural Resources, Islamic Azad University, Bandar Abbas Branch, Iran

ARTICLE INFO:

Received 13 Aug 2021

Revised form 20 Oct 2021

Accepted 19 Nov 2021

Available online 30 Dec 2021

Keywords:

Cadmium,
 Meta-(4-bromobenzyloxy)
 benzaldehyde thiosemicarbazone,
 Ligand,
 Synthesis,
 Metal extraction,
 Ultrasound assisted-dispersive-ionic
 liquid-liquid microextraction

ABSTRACT

In this research, meta-(4-bromobenzyloxy) benzaldehyde thiosemicarbazone (MBBOTSC) as a novel ligand was synthesized from the reaction between meta-(4-bromobenzyloxy) benzaldehyde and thiosemicarbazide under basic condition in water and ethanol as solvents. Ligand has the ability to chelate ions and therefore, it was used to form a complex and extract ions. So, the cadmium ions in water and wastewater samples were separated based on MBBOTSC by ultrasound assisted-dispersive-ionic liquid-liquid microextraction method (USA-D-ILLME) before determination by AT-F-AAS. The MBBOTSC ligand was added to the mixture of the ionic liquid/acetone (IL/AC, [OMIM][PF₆]) and then injected by syringe to 50 mL of water samples at pH 6-7. The sample was put into the ultrasonic accessory for 5 minutes, after complexation (Ligand-Cd; RS...Cd...RS), the water sample was centrifuged for 3 min for phase separation. Due to complexation and back-extraction of Cd in liquid phase, the amount of Cd ions in the water samples was determined by AT-F-AAS after dilution eluent (0.5 M, HNO₃) with DW up to 1 mL. In optimized conditions, the Linear ranges and LOD for 50 mL of water samples were obtained 1-36 μg L⁻¹ and 0.3 μg L⁻¹, respectively (Mean RSD= 1.26%). The validation results were successfully achieved by spiking real samples and using electrothermal atomic absorption spectrometry (ET-AAS).

1. Introduction

Thiosemicarbazones (TSCs) are an important class of organic compounds containing N and S elements that have various uses and properties [1]. These compounds as Schiff base ligands have been widely used to form complexes and to separate metals [2]. Furthermore, due to the presence

of electron pairs on sulfur and nitrogen, these compounds are used over a large area (Fig. 1). TSCs form a prominent class of pharmaceuticals and biologically active compounds by virtue of their antimicrobial, antiviral, anti-bovine viral diarrhea, antiproliferative and antifungal activities [3-7]. Also, the formation of metal complexes plays a very important role in the treatment of cancer, especially since there are reports of the destructive role of reactive oxygen species in increasing the antiproliferative activity of chelators against

*Corresponding Author: YaghoobPourshojaei

Email: pourshojaei@yahoo.com

<https://doi.org/10.24200/amecj.v3.i04.161>

tumour cells [8]. Synthesis of TSC is performed in different ways: a) it is a two-step pathway in which hydrazine reacts with isothiocyanate and the product with aldehyde or ketone, which leads to TSCs [9], b) it is the opposite of pathway a, ie hydrazine first reacts with aldehydes or ketones and then the resulting compound reacts with isothiocyanate [10], c) it is a 4-step process, in which hydrazine first reacts with carbon disulfide and the resulting intermediate reacts with methyl iodide to form methylhydrazine thiocarbamate, eventually nucleophilic substitution with amines and a condensation reaction with an aldehyde or ketone produces TSC [11]. In continuation of our research on the synthesis of various compounds [12-15] and recent report introducing penicillamine as a metal chelator [16], herein, MBBOTSC as ligand containing sulfur and nitrogen has proposed as cadmium chelator.

The toxicity of cadmium (Cd) in water is very important because of the long half-life in the human body. The high toxicity of cadmium caused to damage human organs such as kidneys, liver, lungs and cancer [21,22]. Cadmium is easily transferred from water to plants/humans and has

also contamination in the environment [23]. The environmental protection agency (EPA) and Agency for Toxic Substances and Disease Registry reported that cadmium values in the waters are usually less than $5 \mu\text{g L}^{-1}$ [24]. For healthy people, the mean cadmium concentration in human serum samples is less than $0.2 \mu\text{g L}^{-1}$ [25]. So, the determination of cadmium in water samples is an important concern for controlling toxicity [26,27]. The sensitive techniques such as the electrothermal atomic absorption spectrometry (ET-AAS) [28], the atom trap assist to flame atomic absorption spectrometry and flame atomic absorption spectrometry (AT-F-AAS, F-AAS) [29], inductively coupled plasma-atomic emission spectrometry (ICP-AES) using thiosemicarbazide derivative on alumina [30], and inductively coupled plasma-mass spectrometry (ICP-MS) [31], was used for the determination of cadmium in water and wastewater samples. However, as a low concentration of cadmium and high interferences in wastewater samples, sample preparation before analysis is required. Solid-phase extraction (SPE) and liquid-liquid micro extraction (LLME) are preferred to other techniques for ultra-trace cadmium determination and separation in water samples [32,33].

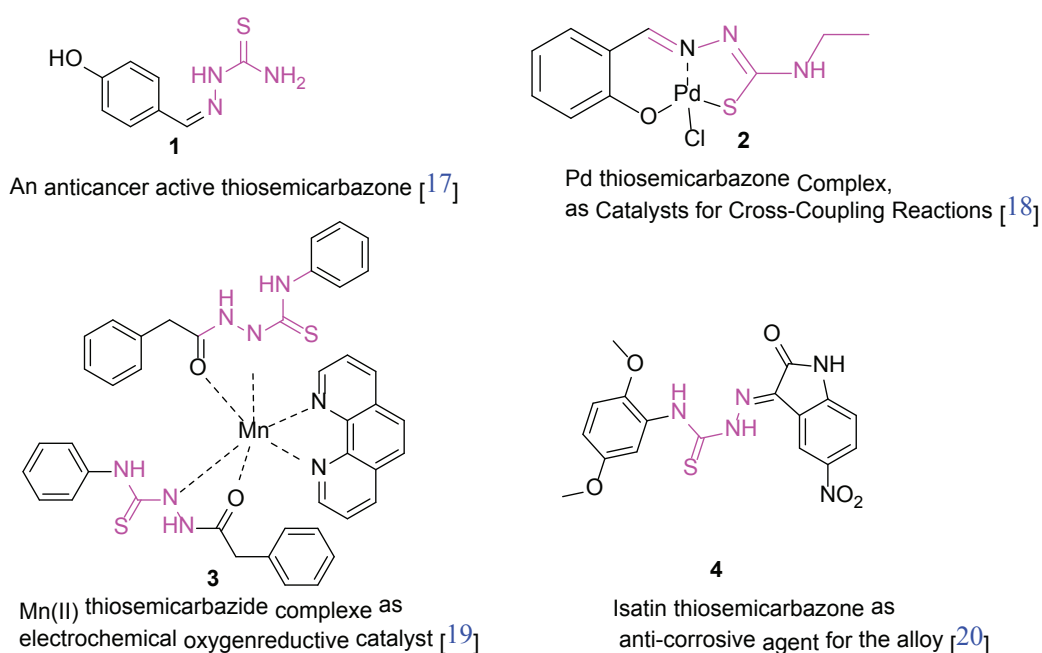


Fig. 1. Several TSC derivatives with different application

Herein a TSC as ligand containing sulfur and nitrogen was synthesized in two steps; a) synthesis of a primary aldehyde; meta-(4-bromobenzyloxy) benzaldehyde, b) synthesis of final ligand meta-(4-bromobenzyloxy) benzaldehyde thiosemicarbazone (Scheme 1). Then the structure of the final ligand was identified by spectroscopic methods such as NMR and IR as well as TLC and melting point.

In this study, the ligand structure was identified by spectroscopic methods such as ^1H NMR, ^{13}C NMR, and FTIR as well as melting point. Thin layer chromatography (TLC) was used to check the progress of the reaction (ethyl acetate and n-hexane were used as the mobile phase). Finally, the mixture of MBBOTSC ligand, IL and acetone was used for cadmium extraction based on the USA-D-ILLME procedure at pH 6-7 before determined by the AT-F-AAS. The results were validated by spiking of water samples and compared to the ET-AAS.

2. Experimental

2.1. Instrumental Analysis

The atom trap flame atomic absorption spectrometry (AT-F-AAS) was used for cadmium determination in water and wastewater samples. The signal absorption improved by the atom trap accessory was added to the burner AAS which was caused to increase the sensitivity of absorption for cobalt analysis. The limits of detection (LOD) for AT-FAAS and FAAS were achieved 0.05 and 0.2 mg L^{-1} , respectively. The information of cobalt was entered to software Avanta (wavelength of 228.8 nm, 3.0 mA and slit of 0.5 nm). The auto-sampler was used for all samples. The linear range for AT-FAAS was 0.05-1.8 mg L^{-1} for cobalt analysis. The validation of results was checked by electrothermal atomic absorption spectrophotometer (GBC, Aus) in water samples (0.2-6.0 $\mu\text{g L}^{-1}$). The pH of the water samples was tuned by the buffer solutions of Merck, Germany before measured by the digital pH meter (Metrohm, Swiss). The phosphate buffers have adjusted the pH for 6-7.

2.2. Reagents and Materials

All reagents/starting materials and solvents used in this study were purchased from commercial suppliers (Merck AG, Aldrich or Acros Organics). The melting point was measured on an electrothermal IA9100 melting point apparatus fixed at 1°C per minute and are uncorrected. The reagents of phosphate buffers (CAS N: 7558-79-4) were prepared from Sigma Aldrich, Germany. The ionic liquid of 1-methyl-3-octylimidazolium hexafluorophosphate ([OMIM] $[\text{PF}_6]$, CAS N: 304680-36-2) was prepared from Sigma Aldrich, Germany. The calibration standards containing 1, 5, 10, 20, 25, 35 $\mu\text{g mL}^{-1}$ Cd standard solutions were prepared by dissolving 1.0 g of cadmium nitrate ($\text{Cd}(\text{NO}_3)_2$) in 1 L of deionized water solution (DW in 2% HNO_3). The standard of Cd solutions was daily made by stock solutions (1g L^{-1} , 1000 mg L^{-1}) which was diluted by DW up to one litre (Millipore, USA). Other reagents such as HCl, HNO_3 and acetone were purchased from Merck, Germany.

2.3. Characterization

IR spectra were recorded using Nicolet FT-IR Magna 550 spectrographs (KBr disks). The NMR spectra were recorded on Bruker 300 spectrometers in $\text{DMSO-}d_6$ as solvent. ^1H NMR data are reported in the following order: Chemical shifts (δ) in part per million (ppm) downfield from TMS as internal standard; approximate coupling constant values (J) in Hertz (HZ); spin multiplicities (s, singlet; d, doublet; t, triplet). Thin-layer chromatography (TLC) was performed on pre-coated Silica Gel F254 plates in ethyl acetate: n-hexane as the mobile phase, for checking the reactions.

2.4. Synthesis of meta-(4-bromobenzyloxy) benzaldehyde

The meta-(4-bromobenzyloxy) benzaldehyde was prepared by reaction of 3-hydroxybenzaldehyde with 4-bromobenzylchloride in the presence of K_2CO_3 as catalyst. The physical and chemical properties of it, was compared with literature and its structure was confirmed [34]

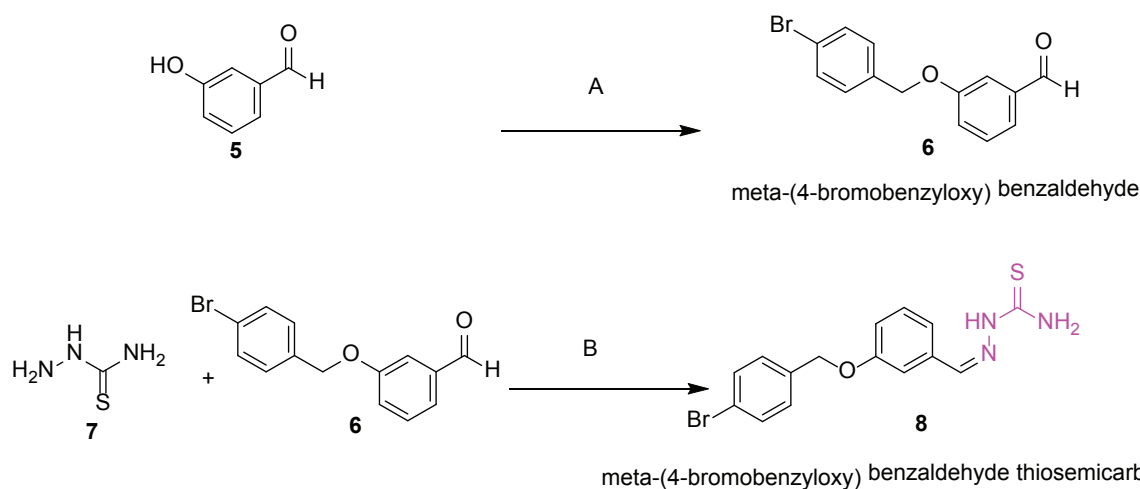
2.5. Synthesis of MBBOTSC

In a 50 ml round bottom flask equipped with a magnet, dissolved 0.1 g of NaOH in 5 cc of distilled water, at first 1 mmol (0.291 mg) of meta-(4-bromobenzyloxy) benzaldehyde and then gradually 1 mmol (0.091 g) of thiosemicarbazide was added to the resulting solution. And the mixture was gently stirred for one day. Then 5 cc of ethanol was added and refluxed for one hour. The reaction progress was controlled by TLC EtOAc/n-hexane (1:3) as eluent. The obtained sediments were filtered using filter paper and dried in a vacuum. Then the precipitate was recrystallized in boiling ethanol. At the end, crystalline product was filtrated to obtain crystalline pure product (Scheme 1). The structure, yield, melting point of synthesized compound is given in the Table 1. Also, the FT-IR, ^1H NMR and ^{13}C NMR spectra of the synthesized ligand are shown in Figures 3 to 5, respectively.

2.6. Procedure of metal extraction

By the USA-D-ILLME procedure, the cadmium

was complexed with the MBBOTSC ligand in water and wastewater samples. Also, the Co ions was determined by AT-F--AAS. The MBBOTSC ligand (0.1 g) added to mixture of [OMIM][PF₆] and acetone (0.2 g: 500 μL) and was injected into 50 mL of Cd included 1-36 $\mu\text{g L}^{-1}$. After shaking of samples (5.0 min), the cobalt ions were extracted with sulfur and nitrogen groups of MBBOTSC ligand [R-N: (S:)Cd(II) \leftarrow (:S)N:-R] at pH 6. After the complexation, the Cd-MBBOTSC was separated with IL [OMIM][PF₆] at the bottom of a PVC conical tube by centrifuging for 3 min and speed of 4000 rpm. The water samples were set aside by auto-sampler (50 mL) and the Cd ios in IL phase back-extracted by 0.5 mL of HNO₃ (0.5M). After diluted acide phase with DW up to 1.0 mL, the Cd values was determined by AT-FAAS. The procedure was shown in Figure 2. The enrichment factor (EF) based on the slope of calibration curve of Cd in the proposed procedure (USA-D-ILLME) and standard method was calculated ($m_1/m_2 = \text{tg}\alpha$, EF= 49.64).



Scheme 1. A) Synthesis of meta-(4-bromobenzyloxy) benzaldehyde 6 B) meta-(4-bromobenzyloxy) benzaldehyde thiosemicarbazone 8, Reagents and conditions: (a) K₂CO₃, DMF, 100 °C; (b) NaOH, H₂O, EtOH, reflux.

Table 1. Structure, yield and melting point of ligand

Entry	Structure	Yield (%)	m.p. (lit)
2		87	187-189°C

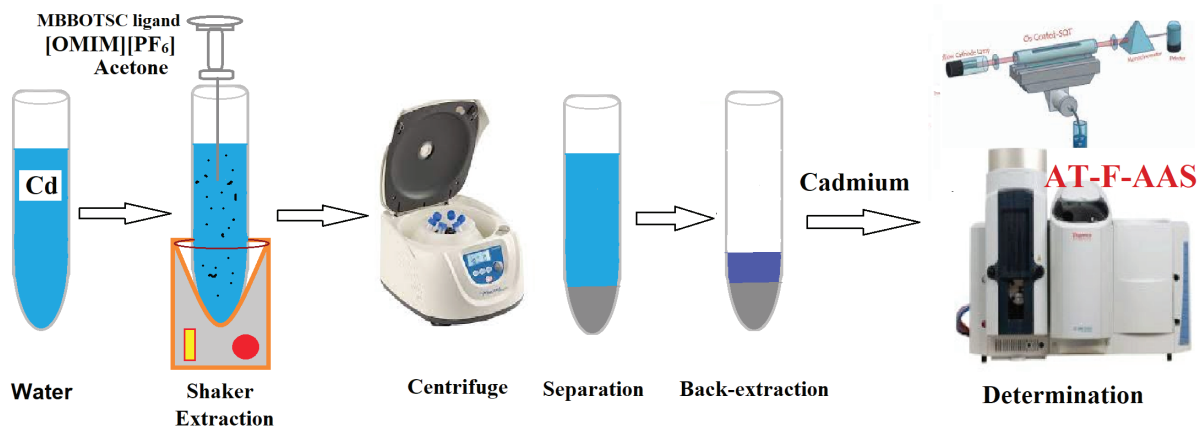


Fig.2. Determination of cadmium based on MBBOTSC ligand by the USA-D-ILLME procedure

3. Results and Discussion

The aim of the present study was to synthesize the meta-(4-bromobenzyloxy) benzaldehyde thiosemicarbazone derivative and to confirm its structure by spectroscopic methods such as FT-IR, ¹H-NMR, and ¹³C-NMR and use it to separate and extract the cadmium ions from the water and wastewater samples before determined by AT-F-AAS. The meta-(4-bromo benzyloxy) benzaldehyde reacted with thiosemicarbazide under basic condition to form the target ligand. Ligand synthesis is based on a nucleophilic attack of the electron pair of the free amine of thiosemicarbazide on the carbon of the carbonyl of aldehyde group, and after removing of a water molecule from intermediate, an imine bond is formed and the product is obtained.

3.1. FTIR Analysis

The FT-IR, ¹H-NMR, ¹³C-NMR spectra of the synthesized ligand analyzed to confirm its structure. In the FT-IR spectrum of the ligand, two stretching vibration frequencies in the regions of 3393 and 3342 cm⁻¹ belong to the NH₂ group. The peak that appearing at the stretching vibration frequency of 3025 cm⁻¹ is related to the aromatic CH stretching vibrations of this synthesized ligand. The peak that has appeared at 1530 cm⁻¹ is related to the stretching vibration frequency of the C = N. And the peak appearing at the frequency 1262 cm⁻¹ is correspond to the stretching vibration frequency of the C = S functional group. The peak at 834 cm⁻¹ is attributed to the C-Br stretching vibration (Fig.3).

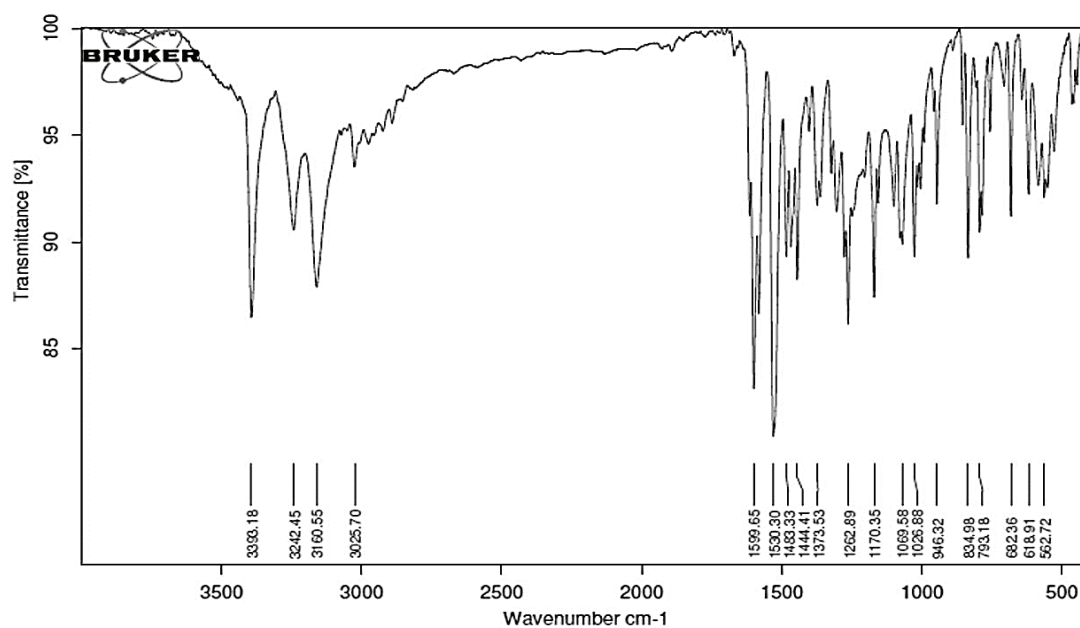


Fig. 3. FT-IR spectrum of MBBOTSC ligand

3.2. $^1\text{H-NMR}$ spectrum

In the $^1\text{H-NMR}$ spectrum of the ligand, a single peak appeared in the region of $11.48 \mu\text{g mL}^{-1}$, which corresponds to hydrogen of NH. Two single peaks in the regions of $8.27 \mu\text{g mL}^{-1}$ and $8.1 \mu\text{g mL}^{-1}$ belong to the two protons NH_2 , and the single peak appear at the $8.04 \mu\text{g mL}^{-1}$ indicate the CH alkene group. The three aromatic protons appeared as a doublet at the $7.5 \mu\text{g mL}^{-1}$ with coupling constant (J) 6 Hz. In the area of $7.45 \mu\text{g mL}^{-1}$, a doublet with coupling constant (J) 6 Hz appeared, which corresponds to two aromatic protons, as well as in the area of $7.35 \mu\text{g mL}^{-1}$, doublet with coupling constant (J) 6 Hz has appeared related to two aromatic protons. In the region $7.03 \mu\text{g mL}^{-1}$, a triplet peak has appeared with coupling constant (J) 6 Hz, which is corresponded to an aromatic proton. The single peak that appears in the region of $5.15 \mu\text{g mL}^{-1}$ belongs to the two

protons of the OCH_2 group. The $^{13}\text{C-NMR}$ spectrum of this compound also confirms the desired structure in that the ligand contains 11 types of carbon, which can be seen in the $^{13}\text{C-NMR}$ spectrum as 11 separate carbon peaks (Fig.4 and 5).

Representative spectral data

Meta-(4-bromobenzoyloxy) benzaldehyde thiosemicarbazone (X): Cream-shaped crystals, *m.p.*: $187\text{-}189^\circ\text{C}$; FT-IR (KBr) (ν_{max} , cm^{-1}): 3393 (N-H), 3342 (N-H), 3160 (N-H), 3025 (C-H_{Ar}), 1530 (C=N), 1262 (C=S), 1170 (C-O), and 834 (C-Br). $^1\text{H NMR}$ (DMSO- d_6 , 300 MHz) δ (ppm): 11.48 (1H, s, NH), 8.27 (1H, s, NH), 8.1 (1H, s, NH), 8.04 (1H, s, CH), 7.5 (3H, d, $J = 6\text{Hz}$, CH_{Ar}), 7.45 (2H, d, $J = 6\text{Hz}$, CH_{Ar}), 7.35 (2H, d, $J = 6\text{Hz}$, CH_{Ar}), 7.03 (1H, t, $J = 6\text{Hz}$, CH_{Ar}), and 5.15 (2H, s, OCH_2). $^{13}\text{C NMR}$ (DMSO- d_6 , 75 MHz) δ (ppm): 178, 158, 142, 136, 136, 131, 130, 121, 117, 112, and 69.

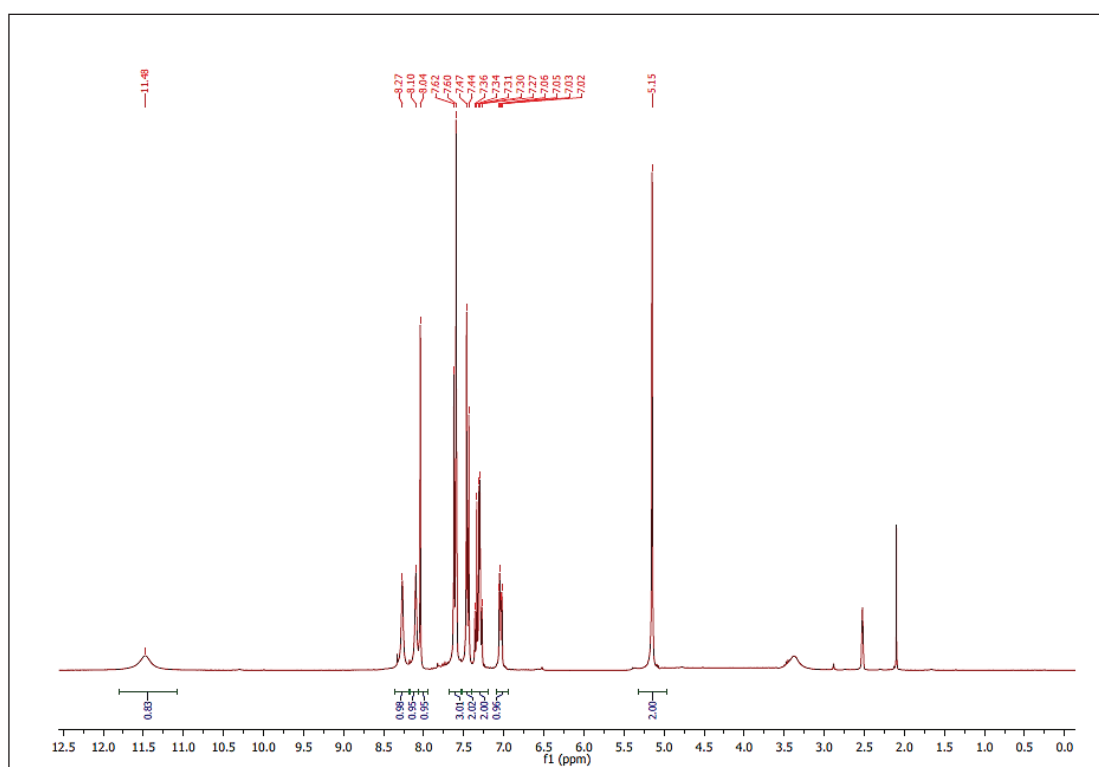


Fig. 4. $^1\text{H-NMR}$ spectrum of MBBOTSC ligand

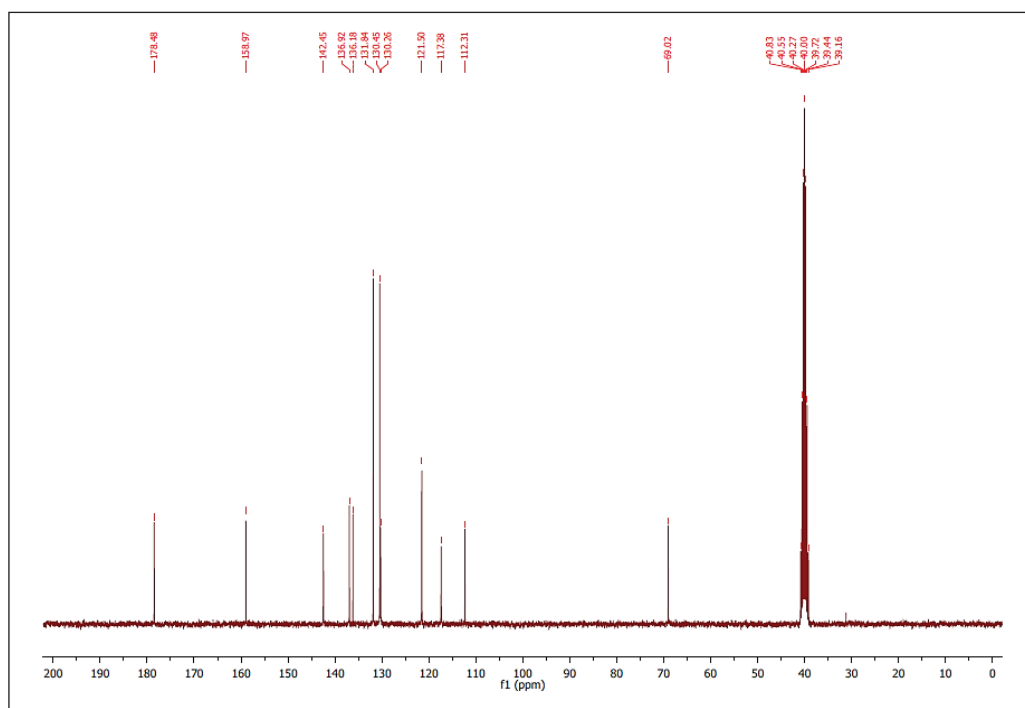


Fig. 5. ^{13}C -NMR spectrum of MBBOTSC ligand

3.3. Mechanism of cobalt extraction

The mechanism of extraction is based on the interaction of imine nitrogen ($=\text{N}$) and thio ($=\text{S}$) groups of the MBBOTSC with cadmium ions using dative/covalent bonding to form stable five ring. The mechanism of extraction between nitrogen and thiol of the MBBOTSC with Cd ions was shown in Figure 6. The mechanism demonstrates that MBBOTSC ligand can bind to Cd^{2+} by complex formations that are easily eliminated from the water samples. The sulfur and nitrogen groups in MBBOTSC ligands caused to easily extracted the Cd ions from aqueous solutions

3.4. Optimizing of parameters

3.4.1. The effect of pH

The pH of the sample is the main parameter for cadmium extraction from water and wastewater samples which was affected on complexation. So, the effect of pH on extraction efficiency of

cadmium with MBBOTSC ligand was studied in different pH between 2 to 11 (Fig.7). The complexation of sulfur and nitrogen groups with Cd^{2+} was depended on the pH of samples. Due to results, the efficient extraction for Cd ions was obtained more than 96% at pH of 6.0-7.0 ($\text{Cd} \rightarrow : \text{S}-\text{R}$ or $: \text{NH}_2-\text{R}$). At higher pH (more than 7.5), the extraction of cadmium was reduced and Cd ions was precipitated [$\text{Cd}(\text{OH})_2$]. The mechanism was depended on the coordination bond between Cd^{2+} and amine /sulfur groups of MBBOTSC ligand at optimized pH. In acidic pH, the NH_2 and SH groups of the MBBOTSC ligand are protonated (+) and complexation decreased. Also, in basic pH at more than 7.5, the NH_2 and SH groups were deprotonated (-) but the cadmium ions precipitated. So, the MBBOTSC is favorite ligand for extraction and determination of cadmium in water samples by the USA-D-ILLME procedure at pH 6.5.

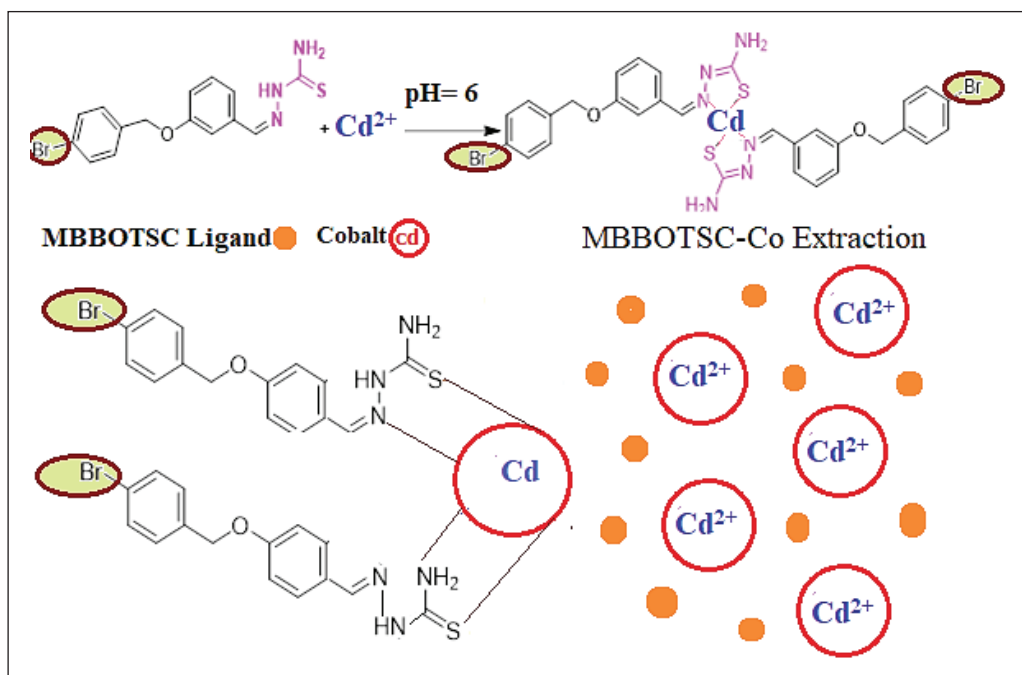


Fig.6. The mechanism of extraction between nitrogen and thiol of the MBBOTSC ligand with cobalt ions

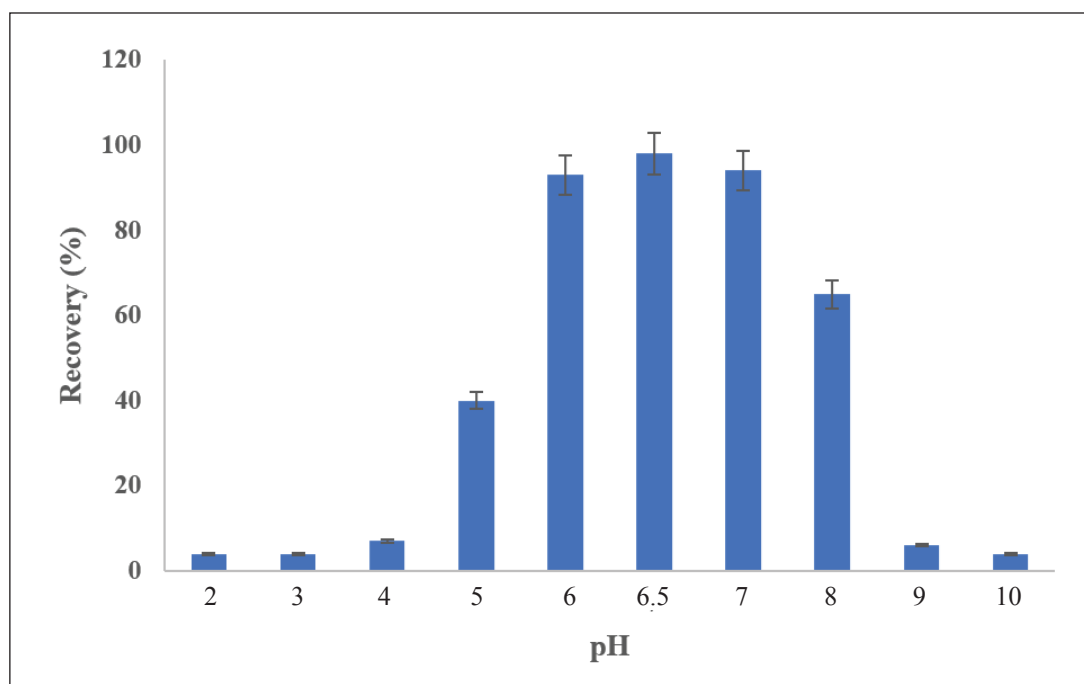


Fig. 7. The effect of pH on cadmium extraction based on MBBOTSC ligand by the USA-D-ILLME procedure

3.4.2. The effect of IL

The different hydrophobic ionic liquid such as, [OMIM] [PF₆], [BMIM][PF₆] and [EMIM][PF₆] was used for collecting and separation ligand/Cd from water samples (Fig. 8). So, the effect of ILs on the cadmium extraction was evaluated within the IL range (0.1-0.5 g) by standard cadmium solution (1-36 µg L⁻¹). Due to results, the high recoveries were achieved by 0.17 g of [OMIM] [PF₆] (98.9%). Therefore, 0.2 g of [OMIM] [PF₆] was used as optimum IL for Cd extraction by MBBOTSC ligand.

3.4.3. Optimization of MBBOTSC ligand

The effect of MBBOTSC for cadmium extraction must be evaluated. MBBOTSC is one of the important factor for cadmium extraction which should be optimized by the USA-D-ILLME procedure. First, 0.015×10^{-4} – 0.35×10^{-4} mol L⁻⁶ of MBBOTSC ligand was examined for cadmium extraction in the water and standard samples. Due to results, the

recovery of extraction increased for 0.065×10^{-4} – 0.35×10^{-4} mol L⁻⁶ of MBBOTSC ligand (Fig. 9). So, 0.07×10^{-4} mol L⁻¹ of MBBOTSC ligand in 50 mL of water sample was selected as optimum amount of ligand for cadmium extraction.

3.4.4. Effect of back-extraction eluents

The effect of back-extraction eluents for cadmium extraction in water samples were studied by MBBOTSC ligand. At acidic pH (pH<4), the covalent bond between the cadmium ions and sulfur/nitrogen groups (complexation) was broken and cadmium ions released into eluents. For this purpose, the different acid solutions (HCl, HNO₃, H₂CO₃, H₂SO₄) were prepared and used for back-extraction cadmium ions from ligand/IL in water and wastewater samples. In-addition, the eluent concentrations and volumes between 0.1-1.0 mol L⁻¹ and 0.1-2.0 mL) was studied. The results showed, the high extraction for cadmium was achieved by 0.5 mL of nitric acid (0.5 M) (Fig. 10).

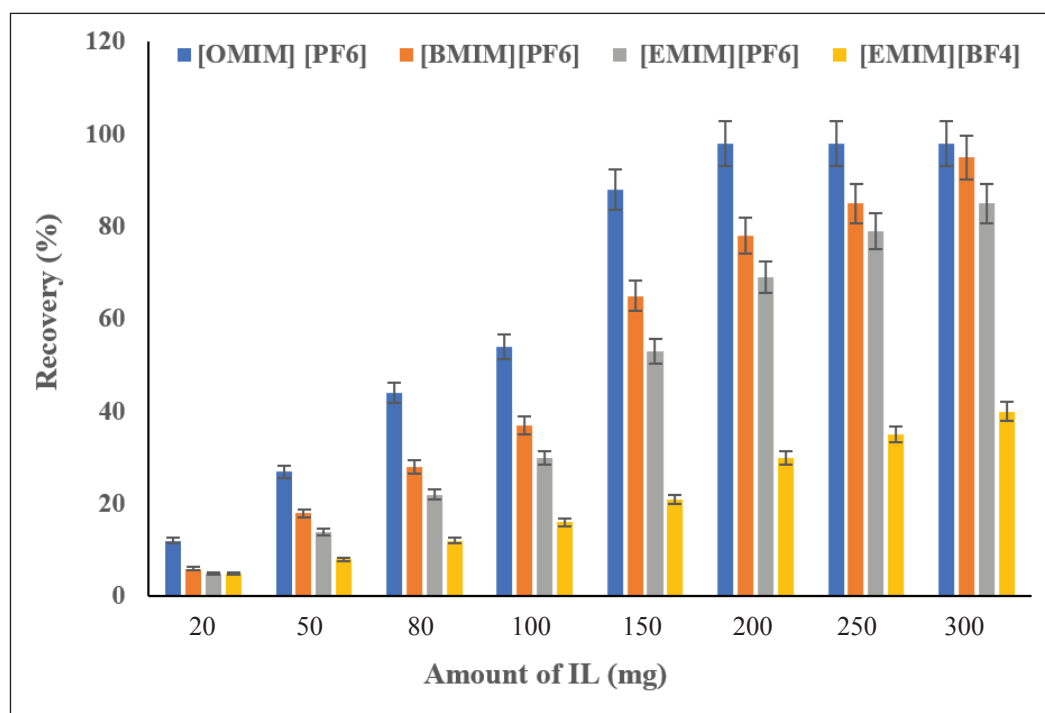


Fig. 8. The effect of amount of IL on cadmium extraction based on MBBOTSC ligand by the USA-D-ILLME procedure

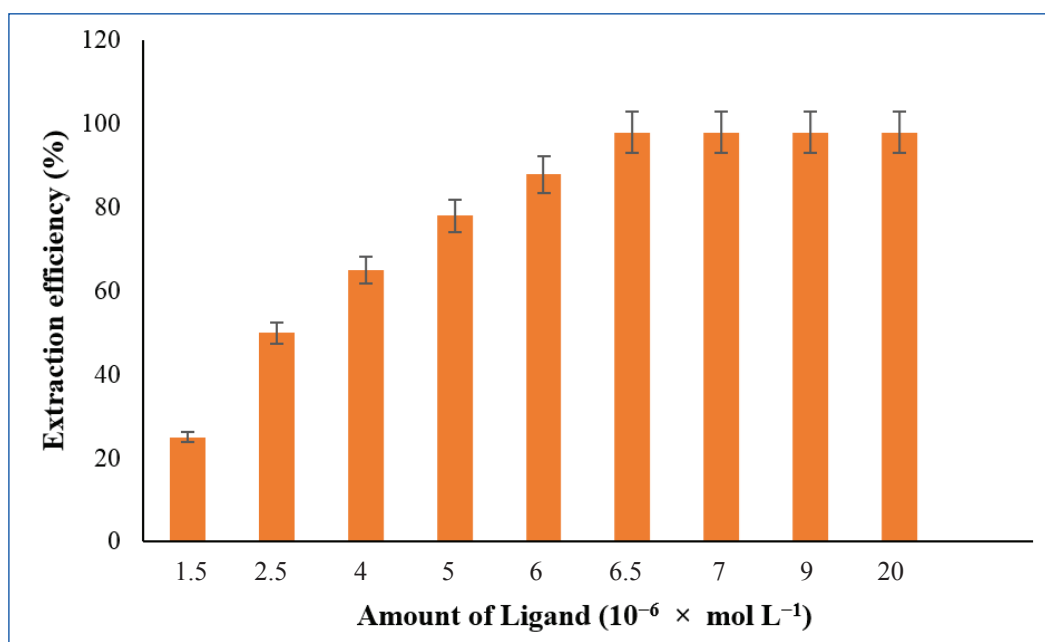


Fig. 9. The effect of ligand on cadmium extraction by the USA-D-ILLME procedure

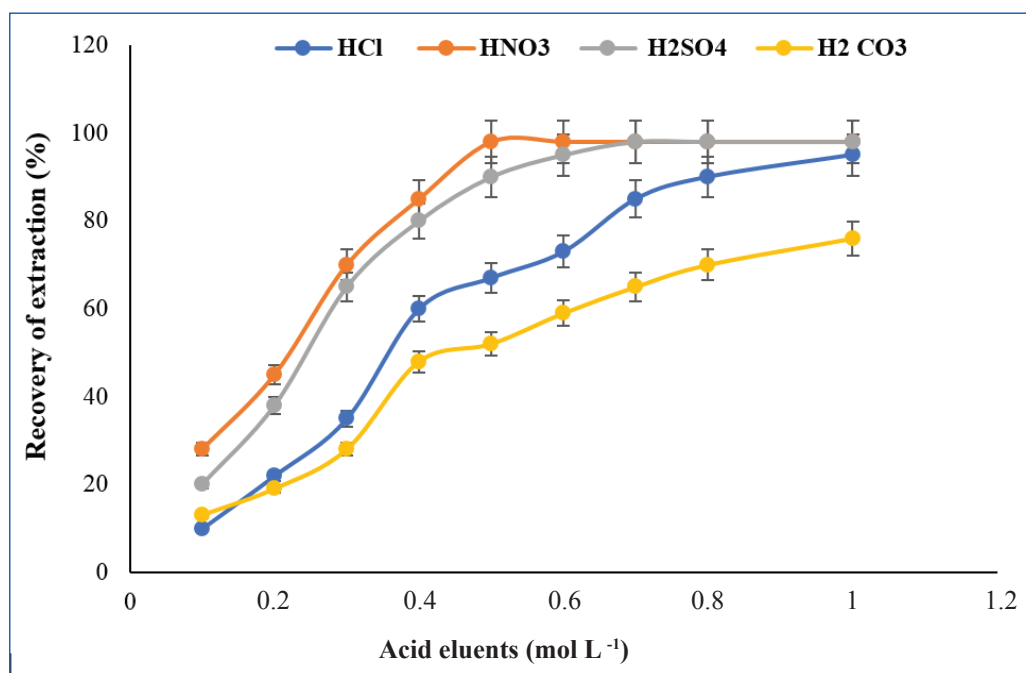


Fig. 10. The effect of eluents on cadmium extraction based on MBBOTSC ligand by the USA-D-ILLME procedure

3.4.5. Effect of sample volume

The effect of sample volume for cadmium extraction in water samples was evaluated between 5 - 100 mL with cadmium concentration ($1-36 \mu\text{g L}^{-1}$) by AT-F-AAS. As result, the high recovery occurred less than 60 mL of water samples at pH 6.5. So, 50 mL was selected as optimum sample volume for cadmium extraction based on the MBBOTSC ligand by the USA-D-ILLME procedure.

3.5. Validation of methodology

The cadmium ions (Cd^{2+}) was separated and determined in water and standard samples by the USA-D-ILLME procedure. The cadmium ions were successfully extracted based on MBBOTSC ligand in water samples with high recovery. Moreover, the accuracy of cadmium analysis must be validated by advanced analytical techniques and spiking samples. In this study, the results of USA-D-ILLME procedure was validated by spiking the standard cadmium solution in water samples (Table 2). Also, the data analysis of cadmium in this procedure can be validated by ET-AAS (Table 3). The results demonstrated

the accurate extraction and high recovery for cadmium ions in water and wastewater samples. The spiked samples showed satisfactory results for extraction and separation of cadmium based on the MBBOTSC ligand in water samples by the USA-D-ILLME procedure.

4. Conclusions

An analytical method for extraction and determination of cadmium in water samples was carried out by synthesis of meta-(4-bromobenzyloxy) benzaldehyde thiosemicarbazone (MBBOTSC) as a novel ligand at pH 6.5. The complexation between cadmium and ligand was achieved with the MBBOTSC ligand and cadmium extracted by the USA-D-ILLME procedure. By the proposed procedure, the simple and fast extraction, as well as the efficient separation for cadmium ions was obtained at optimized conditions. Results showed the LOD, the working range and RSD ranges were obtained at $0.3 \mu\text{g L}^{-1}$, $1-75 \mu\text{g L}^{-1}$ and 1.12%-2.54%, respectively. Due to results, the separation cadmium in water samples was simply achieved by the IL phase before determined by AT-F-AAS.

Table 2. The validation of results for cadmium extraction based on the MBBOTSC ligand in water samples by spiking standard solution ($\mu\text{g L}^{-1}$).

Samples	Added	USA-D-ILLME *	Recovery (%)
Drinking Water	----	0.45 ± 0.02	----
	0.5	0.94 ± 0.05	98.1
	1.0	1.47 ± 0.07	102
Well water	----	5.14 ± 0.19	----
	5.0	9.95 ± 0.44	96.2
	10	15.25 ± 0.62	101.1
Wastewater	----	9.85 ± 0.46	
	5	14.76 ± 0.67	98.2
	10	19.78 ± 0.84	99.3
Wastewater	----	12.58 ± 0.57	
	10	23.01 ± 1.14	104.3
	20	32.31 ± 1.52	98.6

* Mean of three determinations \pm confidence interval ($P=0.95$, $n=5$)

Wastewater prepared from petrochemical industry in Arak and well water from south of Tehran (Share-Ray)

Table 3. The validation of methodology for cadmium extraction and determination in water by spiking samples and comparing to the ET-AAS analyzer

Samples	Added ($\mu\text{g L}^{-1}$)	ET-AAS* ($\mu\text{g L}^{-1}$)	USA-D-ILLME * ($\mu\text{g L}^{-1}$)	Recovery (%) ET-AAS	Recovery (%) USA-D-ILLME
Drinking Water	-----	0.73 ± 0.03	0.69 ± 0.02	-----	-----
	0.5	1.21 ± 0.05	1.22 ± 0.06	96.0	106
Well water	-----	3.76 ± 0.16	3.82 ± 0.18	-----	-----
	3.0	6.72 ± 0.29	6.77 ± 0.32	98.6	98.3
Wastewater	-----	14.02 ± 0.71	13.87 ± 0.64	-----	-----
	15	28.56 ± 1.28	29.03 ± 1.42	96.9	101.1
Wastewater	-----	16.32 ± 0.78	16.15 ± 0.81	-----	-----
	20	36.25 ± 1.68	35.58 ± 1.74	99.7	97.2

* Mean of three determinations \pm confidence interval ($P=0.95$, $n=5$)

Wastewater prepared from petrochemical industry in Arak and well water from south of Tehran (Share-Ray)

5. Acknowledgments

We thank the Department of Medicinal Chemistry, Faculty of Pharmacy, Kerman University of Medical Sciences, Kerman, and Environmental Engineering, Faculty of Natural Resources, Islamic Azad University, Bandar Abbas Branch for support of this work.

6. References

- [1] L.N. Suvarapu, A.R. Somala, J.R. Koduru, S.O.k. Baek, V.R. Ammireddy, A critical review on analytical and biological applications of thio- and phenylthiosemicarbazones, *Asian J. Chem*, 24 (2012) 1889-1898. <https://asian-journalofchemistry.co.in/Home.aspx>
- [2] S.A. Hosseini-Yazdi, S. Hosseinpour, A.A. Khandar, W.S. Kassel, N.A. Piro, Copper (II) and nickel (II) complexes with two new bis(thiosemicarbazone) ligands: Synthesis, characterization, X-ray crystal structures and their electrochemistry behavior, *Inorganica Chim. Acta*, 427 (2015) 124-130. <https://doi.org/10.1016/j.ica.2014.12.011>.
- [3] İ. Kizilcikli, Y.D. Kurt, B. Akkurt, A.Y. Genel, S. Birteksöz, G. Ötük, B. Ülküseven, Antimicrobial activity of a series of thiosemicarbazones and their ZnII and PdII complexes, *Folia Microbiol.*, 52 (2007) 15-25. <https://doi.org/10.1007/BF02932132>.
- [4] C. Shipman, Jr., S.H. Smith, J.C. Drach, D.L. Klayman, Antiviral activity of 2-acetylpyridine thiosemicarbazones against herpes simplex virus, *Antimicrob. Agents. Chemother*, 19 (1981) 682-685. <https://dx.doi.org/10.1128%2Faac.19.4.682>.
- [5] M.C. Soraires Santacruz, M. Fabiani, E.F. Castro, L.V. Cavallaro, L.M. Finkielstein, Synthesis, antiviral evaluation and molecular docking studies of N4-aryl substituted/unsubstituted thiosemicarbazones derived from 1-indanones as potent anti-bovine viral diarrhea virus agents, *Bioorg. Med. Chem*, (2017) 4055-4063. <https://doi.org/10.1016/j.bmc.2017.05.056>.
- [6] J. Qi, X. Wang, T. Liu, M. Kandawa-Schulz, Y. Wang, X. Zheng, Synthesis, antiproliferative activity and mechanism of copper(II)-thiosemicarbazone complexes as potential anticancer and antimicrobial agents, *J. Coord. Chem.*, 73 (2020) 1208-1221. <https://doi.org/10.1080/00958972.2020.1768378>.
- [7] D. Rogolino, A. Gatti, M. Carcelli, G. Pelosi, F. Bisceglie, F.M. Restivo, F. Degola, A. Buschini, S. Montalbano, D. Feretti, C. Zani, Thiosemicarbazone scaffold for the design of antifungal and antiaflatoxigenic agents: evaluation of ligands and related copper complexes, *Sci. Rep*, 7 (2017) 11214. <https://doi.org/10.1038/>

- s41598-017-11716-w.
- [8] M. Whitnall, J. Howard, P. Ponka, D.R. Richardson, A class of iron chelators with a wide spectrum of potent antitumor activity that overcomes resistance to chemotherapeutics, *Proc. Nat. Acad. Sci.*, 103 (2006) 14901. <https://doi.org/10.1073/pnas.0604979103>.
- [9] R.H. Vekariya, K.D. Patel, D.P. Rajani, S.D. Rajani, H.D. Patel, A one pot, three component synthesis of coumarin hybrid thiosemicarbazone derivatives and their antimicrobial evolution, *J. Assoc. Arab Univ. Basic Appl. Sci.*, 23 (2017) 10-19. <https://doi.org/10.1016/j.jaubas.2016.04.002>.
- [10] S. Cunha, T.L.d. Silva, One-pot and catalyst-free synthesis of thiosemicarbazones via multicomponent coupling reactions, *Tetrahedron. Lett.*, 50 (2009) 2090-2093. <https://doi.org/10.1016/j.tetlet.2009.02.134>.
- [11] M. Tyagi, S. Chandra, Synthesis, characterization and biocidal properties of platinum metal complexes derived from 2,6-diacetylpyridine (bis thiosemicarbazone), *Open J. Inorg. Chem.*, 02 (2012). <http://dx.doi.org/10.4236/ojic.2012.23007>.
- [12] A. Asadipour, Y. Pourshojaei, K. Eskandari, A. Foroumadi, A short synthesis of 7-amino alkoxy homioisoflavonoides, *RSC Adv.*, 7 (2017) 44680-44687. <https://doi.org/10.1039/C7RA08990B>.
- [13] Y. Pourshojaei, F. Zolala, K. Eskandari, M. Talebi, L. Morsali, M. Amiri, A. Khodadadi, R. Shamsimeyandi, E. Faghih-Mirzaei, A. Asadipour, Nickel ferrite (NiFe₂O₄) nanoparticles as magnetically recyclable nanocatalyst for highly efficient synthesis of 4H-chromene derivatives, *J. nanosci. nanotechnol.*, 20 (2020) 3206-3216. <https://doi.org/10.1166/jnn.2020.17396>.
- [14] Y. Pourshojaei, A. Abiri, R. Eskandari, F. Dou-randish, K. Eskandari, A. Asadipour, Synthesis, biological evaluation, and computational studies of novel fused six-membered O-containing heterocycles as potential acetylcholinesterase inhibitors, *Comput. Biol. Chem.*, 80 (2019) 249-258. <https://doi.org/10.1016/j.compbiolchem.2019.04.004>.
- [15] Y. Pourshojaei, M. Nikzad, K. Eskandari, M. Darijani, A. Hassanzadeh, E. Faghih-Mirzaei, A.J.C.C.A. Asadipour, Ultrasound-assisted and efficient Knoevenagel condensation reaction catalyzed by silica sodium carbonate nanoparticles, *Croat. Chem. Acta*, 91 (2018) 19-28. <https://doi.org/10.5562/CCA3261>.
- [16] Y. Pourshojaei, A. Nasiri, Cobalt separation from water and food samples based on penicillamine ionic liquid and dispersive liquid-liquid microextraction before determination by AT-FAAS, *Anal. Method. Environ. Chem. J.*, 4 (2021) 21-32. <https://doi.org/10.24200/amecj.v4.i03.148>.
- [17] B.Z. Sibuh, S. Khanna, P. Taneja, P. Sarkar, N.K. Taneja, Molecular docking, synthesis and anticancer activity of thiosemicarbazone derivatives against MCF-7 human breast cancer cell line, *Life. Sci.*, 273 (2021) 119305. <https://doi.org/10.1016/j.lfs.2021.119305>.
- [18] I.D. Kostas, B.R. Steele, Thiosemicarbazone complexes of transition metals as catalysts for cross-coupling reactions, *catal.*, 10 (2020) 1107. <https://doi.org/10.3390/catal10101107>.
- [19] M.K. Bharty, A. Bharti, R. Chaurasia, U.K. Chaudhari, S.K. Kushawaha, P.K. Sonkar, V. Ganesan, R.J. Butcher, Synthesis and characterization of Mn(II) complexes of 4-phenyl(phenyl-acetyl)-3-thiosemicarbazide, 4-amino-5-phenyl-1,2,4-triazole-3-thiolate, and their application towards electrochemical oxygen reduction reaction, *Polyhedron*, 173 (2019) 114125. <https://doi.org/10.1016/j.poly.2019.114125>.
- [20] Q. Yuan, R. Cheng, S. Zou, C. Ding, H. Liu, Y. Wang, D. Yang, X. Xiao, Q. Jiang, R. Tang, J. Chen, Isatin thiosemicarbazone derivatives as inhibitors against corrosion of AA6060 aluminium alloy in acidic chloride medium: substituent effects, *J. Mater. Res. Technol.*, 9 (2020) 11935-11947. <https://doi.org/10.1016/j.jmrt.2020.08.012>.
- [21] S. Bhattacharya, The role of probiotics in the amelioration of cadmium toxicity, *Biol. Trace.*

- Elem. Res, 197 (2020) 440-444. <https://doi.org/10.1007/s12011-020-02025-x>.
- [22] M. Wang, Z. Chen, W. Song, D. Hong, L. Huang, Y. Li, A review on cadmium exposure in the population and intervention strategies against cadmium toxicity, *Bull. Environ. Contam. Toxicol*, 106 (2021) 65-74. <https://doi.org/10.1007/s00128-020-03088-1>.
- [23] Y. Huang, C. He, C. Shen, J. Guo, S. Mubeen, J. Yuan, Z. Yang, Toxicity of cadmium and its health risks from leafy vegetable consumption, *Food. Funct*, 8 (2017) 1373-1401. <https://doi.org/10.1039/C6FO01580H>.
- [24] ATSDR, Agency for Toxic Substances and Disease Registry, 2016. 4770 Buford Hwy NE, Atlanta, GA 30341 Contact CDC: 800-232-4636 / TTY: 888-232-6348. https://www.atsdr.cdc.gov/dro/central_branch.html
- [25] ACGIH, Documentation of the Threshold Limit Values (TLVs) and Biological Exposure Indices, American Conference of Governmental Industrial Hygienists, 2016 7th Ed. <https://www.acgih.org/science/tlv-bei-guidelines/>
- [26] M. Banihashemi, N. Dalali, N. Sehati, B. Farajmand, Decoration of Fe₃O₄@SiO₂@ZnO as a high performance nanosorbent on a stir bar microextraction device for preconcentration and determination of cadmium in real water samples, *Microchem. J*, 154 (2020) 104599. <https://doi.org/10.1016/j.microc.2020.104599>.
- [27] Y. Ji, M. Zhao, A. Li, L. Zhao, Hydrophobic deep eutectic solvent-based ultrasonic-assisted dispersive liquid-liquid microextraction for preconcentration and determination of trace cadmium and arsenic in wine samples, *Microchem. J*, 164 (2021) 105974. <https://doi.org/10.1016/j.microc.2021.105974>.
- [28] D. Martínez, G. Grindlay, L. Gras, J. Mora, Determination of cadmium and lead in wine samples by means of dispersive liquid-liquid microextraction coupled to electrothermal atomic absorption spectrometry, *J. Food. Compost. Anal*, 67 (2018) 178-183. <https://doi.org/10.1016/j.jfca.2018.01.013>.
- [29] A. Girgin, N. Atsever, T. Borahan, Z. Tekin, Ç. Büyükpınar, N. San, S. Bakırdere, Determination of cadmium in mineral water samples by slotted quartz tube-flame atomic absorption spectrometry after peristaltic pump assisted silica nanoparticle based pipette tip solid phase extraction, *Water. Air. Soil. Pollut*, 232 (2021) 422. <https://doi.org/10.1007/s11270-021-05386-8>.
- [30] F. Sabermahani a, R. askari b, S.J. Hosseini fard, M. Saeidi, Determination of cadmium in water and environmental samples by inductively coupled plasma atomic emission spectrometry after solid phase extraction using thiosemicarbazide derivative on alumina, *Scientia Iranica*, 21 (2014) 2012-2020. http://scientiairanica.sharif.edu/issue_153_304.html
- [31] Y. Takaku, K. Ishizuka, A. Nagaoka, M. Minakawa, T. Morita, K. Fujimoto, Determination of cadmium in sea water by ICP-MS with chelating resin preconcentration, *Bunseki. Kagaku*, 65 (2016) 399-402. <http://dx.doi.org/10.2116/bunsekikagaku.65.399>.
- [32] X. Wang, H. Liu, C. Lin, L. Pang, J. Yang, Q. Zeng, Optimization of ultrasound-assisted magnetic retrieval-linked ionic liquid dispersive liquid-liquid microextraction for the determination of cadmium and lead in water samples by graphite furnace atomic absorption spectrometry, *J. Ind. Eng. Chem*, 56 (2017) 321-326. <http://dx.doi.org/10.1016/j.jiec.2017.07.027>.
- [33] L. Esfanjani, N. Farhadyar, H.R. Shahbazi, F. Fathi, Development of a method for cadmium ion removal from the water using nano γ -alumina/ β -cyclodextrin, *Toxicol. Rep.*, 8 (2021) 1877-1882. <https://doi.org/10.1016/j.toxrep.2021.11.009>.
- [34] J. S. Lan, T. Zhang, Y. Liu, Y. Zhang, J.-w. Hou, S.-S. Xie, J. Yang, Y. Ding, Z. Z. Cai, Synthesis and evaluation of small molecules bearing a benzyloxy substituent as novel and potent monoamine oxidase inhibitors, *Med. Chem. Comm.*, 8 (2017) 471-478. <https://doi.org/10.1039/C6MD00586A>.